MEASUREMENT OF FLUX PINNING
IN PROTON IRRADIATED NIOBIUM
AND
THE FLUX LINE LATTICE DEFECT
INSTABILITY MODEL

A dissertation presented to

The Graduate Faculty of

The College of Arts and Sciences of Ohio University

In Partial Fulfillment

of the Requirements for the Degree

Doctor of Philosophy

by

Keunha Koh

June 1981

This dissertation has been approved
for the Department of Physics
and the College of Arts and Sciences by

Roger W Rollins

Professor of Physics

Wm F. Smith

Dean of the College of Arts and Sciences

ACKNOWLEDGEMENT

It is my pleasure to acknowledge those persons who have guided and assisted me throughout this work.

Professor Roger W. Rollins, my advisor, introduced me to superconductivity and suggested this problem. He also taught me the magnetic field profile measurement technique he had developed and guided me throughout the dissertation. I am specially grateful to him for allowing me to persue this subject in directions which corresponded with my own interests.

Professor Ronald L. Cappelletti gave me valuable understandings of various subjects through long discussions. I would like to thank him for his sincere friendship.

I would also like to express my thanks to Dr. J. Anjaneyulu, former co-graduate student for helping me to get aquainted with the labratory equipment and Mr. P. H. Beasley and Mr. D. J. Sturbois for their assistance in preparing the niobium samples.

I wish to thank all the faculty and staff of the physics department for their encouragement and friendship which made my stay at Ohio University a pleasent one.

TABLE OF CONTENTS

	page
LIST OF TABLES	vii
LIST OF FIGURES	viii
Chapter	
1. INTRODUCTION	1
2. FLUX LINE LATTICE	5
2.1 Introduction	5
2.2 The Critical State	8
2.3 Elastic Properties of the Flux Line Lattice	10
2.3.1 Elastic Constants of the Flux Line Lattice	10
2.3.2 Displacements of Flux Lines due to Local Forces	13
2.4 Flux Line Lattice Defects	22
3. REVIEW AND CRITIQUE OF CURRENT FLUX PINNING THEORIES	28
3.1 Pinning Mechanisms	28
3.2 Summation Rules and Threshold Criterion	30
3.3 Some Experimental Results and Their Interpretations	37
4. EXPERIMENTAL TECHNIQUES EMPLOYED	47
4.1 Sample Preperation	47
4.2 Resistivity Ratio	49
4.3 Proton Irradiation	50
4.4 Magnetic Field Profile	55
4.5 Intermediate Temperature Heat Treatment	70

Chapter page

5. EXPERIMENTAL RESULTS 71

5.1 Histories of Samples 71

5.2 Field Profiles 83

5.3 Field Dependences of Total Pinned Magnetic Field and Volume Pinning Force 91

5.4 Proton Fluence Dependence of Total Pinned Magnetic Field 106

5.5 Dependence of Total Pinned Magnetic Field on Subsequent Heat Treatment 118

5.6 The Time Dependence of Total Pinned Magnetic Field and Cycling Effect 118

5.7 Summary 131

6. FLUX LINE LATTICE DEFECT INSTABILITY MODEL 134

6.1 Introduction 134

6.2 FLLD Instability Model 136

6.2.1 Forces Acting on a FLLD 137

6.2.2 Origin of the Instability 138

6.3 Origin of FLLD 150

6.4 Critical Pinning Force 156

6.5 Interpretations of Experimental Results 161

6.5.1 Specific Pinning Force vs. Volume Pinning Force 161

6.5.2 Proton Fluence Dependence of Volume Pinning Force and Peak Effect 162

6.5.3 Cycling Effect and Time Dependence of Volume Pinning Force 163

7. SUMMARY 165

7.1 Experiment 165

Chapter page

7.2 FLLD Instability Model 166

REFERENCES 167

APPENDICES 171

LIST OF TABLES

Table		page
5.1	History of sample #16	73
5.2	History of sample #58	71
5.7	Histories of samples #17, #20, #21 and #22	73
5.4	Histories of samples #23, #26, #27 and #29	79
5.5	Histories of samples #12 and #13	81

LIST OF FIGURES

Figure		page
2.1	FLL elastic constants vs. reduced field for a high K material	16
2.2	FLL elastic constants for pure niobium	18
2.3	Maximum displacements of the flux lines for the maximum pinning force	20
2.5	Electron microscopies of flux line lattice	25
3.1	Illustrative diagram of pinning threshold of FLL instability model	35
3.2	Specific pinning force vs. elementary pinning force	40
3.3	Synchronization effect of FLL to the multiple of pinning center spacing	42
3.4	Cycling effect	44
4.1	Radiation damage station	53
4.2	Diagram used to obtain field profile equations	62
4.3	Block diagram of electronic circuitry used for field profile measurement	64
4.4	Magnetization curve of an annealed Nb sample obtained at 4.2 K	66
4.5	$\mu_{eq}(B)$ obtained from magnetization measurements	68
5.1	Wave forms at different dc fields	85
5.2	Field profiles at different dc fields	87
5.3	Field profiles with different ac field amplitudes	89
5.4	Total pinned magnetic field vs. dc field (sample #18)	94
5.5	Total pinned magnetic field vs. dc field (sample #16)	96

Figure		page
5.6	Total pinned magnetic field vs. dc field (samples #17, 20, #21 and #22)	98
5.7	Total pinned magnetic field vs. dc field (sample #23, #26, #27 and #29)	100
5.8	Volume pinning force vs. dc field (sample #17)	102
5.9	volume pinning force vs. dc field (sample #22)	104
5.10	Total pinned magnetic field vs. proton fluence (H_{dc} = 2.66 KOe)	110
5.11	Total pinned magnetic field vs. proton fluence (H_{dc} = 2.60 KOe)	112
5.12	Total pinned magnetic field vs. proton fluence (H_{dc} = 2.48 KOe)	114
5.13	Total pinned magnetic field vs. proton fluence (H_{dc} = 2.30 KOe)	116
5.14	Annealing temperature dependence of volume pinning force	121
5.15	Annealing temperature dependence of defect size distribution	123
5.16	Time dependent behavior of volume pinning force with ac field amplitude of 40 Oe at 1.88 KOe (sample #16)	127
5.17	Time dependent behavior of volume pinning force with ac field amplitude of 60 Oe at 1.88 KOe (sample #16)	129
6.1	Forces on a FLL defect	144
6.2	Relation between a pinning force and position of a FLLD	146
6.3	Illustrative diagram of the instability	148
6.4	Forces and stable configurations between parallel edge dislocation lines	153
6.5	Illustrative diagram describing peak effect	159

Chapter I

INTRODUCTION

In the mixed state of the type II superconductor, the magnetic field forms a two dimensional triangular lattice with a supercurrent vortex producing one quantum of magnetic flux, ϕ_o, at each lattice point. When a transport current J is applied, a Lorentz-like force $\vec{J} \times \vec{\phi}_o$ acts on each vortex. If the superconductor is a homogeneous material (free of crystalline defects or impurities), the flux line lattice (FLL) would move viscously parallel to the force. The moving FLL induces an electric field which acts like a resistive voltage and causes power dissipation. On the other hand, if the superconductor has inhomogeneities which restrict the FLL movement, then the power dissipation can be prevented until the Lorentz like force exceeds the restrictive force F_V (global or volume pinning force). Therefore, a large volume pinning force is essential to ensure the high critical currents and magnetic fields necessary for many practical applications of superconductivity. An understanding of the pinning mechanism would be very helpful in the research effort to establish large volume pinning forces in superconducting materials.

The interaction force f_P (elementary pinning force)

between a single crystaline defect (pinning center) and the FLL has been calculated for several specific types of defects. However, the summation of these elementary pinning forces in the proper way to find the volume pinning force has proved to be a very difficult problem and is still unsolved for the general case. A direct summation of the elementary pinning forces over pinning centers contained in a unit volume gives a much larger volume pinning force than found experimentally. Yamafuji and Irie (1967) and Labusch (1969a) pointed out that the summation should be carried out statistically taking account of the elasticity of the FLL. This model is known as the statistical summation model or quadratic summation model. In this dissertation, this model will be referred to as the FLL instability model rather than the statistical summation model and it will be contrasted with the flux line lattice defect (FLLD) instability model which is presented in chapter 6. A perfectly rigid FLL interacting with randomly distributed pinning centers will give a zero volume pinning force since the number of pinning centers whose pinning force is positive at a certain instant should be same as those whose pinning force is negative. Consequently, it is also suggested that an instability in the FLL movement is the necessary condition for the volume pinning force and an elementary pinning force which is not big enough to produce the instability should not contribute toward the volume

pinning force (threshold criterion). There has been considerable experimental effort to find this threshold but all the experimental evidence shows that the real threshold is at least several orders of magnitude lower, if it exists at all, than predicted by the current theory. Even if we ignore the threshold, the current theories often fail to explain the experimental phenomena adequately. Kramer (1977) suggested an empirical curve to represent the relation between the elementary pinning force and the volume pinning force, however, a theoretical justification was not presented.

In order to understand the flux pinning phenomena, one should know the relationship between the elementary pinning force, f_p, and the volume pinning force, F_v, and the effect of a change in f_p on the behavior of F_v. In flux pinning experiments, it is highly desirable to deal with only one kind and size of pinning center if possible. We chose niobium in its purist and defect free form obtainable as the sample material. The cylindrical samples were irradiated with 1 to 3.2 Mev protons at room temperature to produce dislocation loops (Anjaneyulu 1977). The magnetic field gradients in these samples were measured using the technique developed by Rollins et al. (1974) and the volume pinning forces were determined from these gradients. Many of the results obtained are similar to results previously reported by other authors but we also found some baffling

phenomena unreported in the literature. To explain the experimental results, we developed a new summation model based on an instability in the movement of flux line lattice defects. This model is, therefore, named the flux line lattice defect (FLLD) instability model and we believe it explains most experimental phenomena at least qualitatively at present.

To provide a background for the magnetic flux pinning theory, the properties of the FLL and its relation to the volume pinning force and the driving force are presented in chapter 2. The present pinning theories and their difficulties in explaining the experimental data are briefly reviewed in chapter 3. The experimental techniques employed in the course of this dissertion are explained in chapter 4 and their results are presented in chapter 5. The FLLD instability model and the interpretations of the experimental results by this model are presented in chapter 6. The summary is given in chapter 7.

Chapter II

FLUX LINE LATTICE

2.1 Introduction.

The general theory of superconductivity including the Ginzburg-Landau theory which is applicable to type II superconductors is presented by Tinkham (1975) and Parks (1969) and excellent reviews of magnetic flux pinning theory and experiment are given by Campbell and Evett (1972) and Ullmaier (1975).

Abrikosov (1957) first solved the Ginzburg-Landau equations for a superconductor with a Ginzburg-Landau parameter κ greater than $1/\sqrt{2}$ and predicted the existence of what is called the mixed state. For $\kappa > 1/\sqrt{2}$, the energy of the interface between the superconducting phase and the normal phase becomes negative and in the mixed state the specimen should have as large an interface area as possible with the minimum normal phase volume. The mixed state consists of supercurrent vortices surrounding a normal core with each vortex containing one quantum of magnetic flux. These quantized flux lines form a two dimensional triangular lattice (Fig. 2.4).

In an applied magnetic field lower than H_{c1}, the total free energy is minimum when no vortices are present in

the bulk of the superconductor and the magnetic field is entirely excluded (Meissner effect). As the applied magnetic field, H, is increased above H_{c1}, the total free energy is lowered by introducing the vortices into the bulk. These vortices enter through the surface of the sample and (in the absence of flux pinning) form the triangular lattice described above with uniform vortex density throughout the bulk. The density of quantized flux lines (vortices) continues to increase until H reaches H_{c2}. The average magnetic induction field, B, in the bulk of the superconductor is equal to $n\phi_0$, where n is the density of vortices. At H_{c2}, $B = B_{c2} = H_{c2}$ and the normal cores are overlapping. The bulk of the sample is in the normal state when $H > H_{c2}$, however, a very thin sheath (thickness 600 Å for Nb) remains superconducting until $H > H_{c3} \sim 1.7\ H_{c2}$.

In a type II superconductor in the mixed state, the local magnetic field, h, in the London limit ($\kappa \to \infty$) is (Tinkham 1975)

$$\lambda^2 \nabla^2 h - h = -\phi_0 \sum_j \delta(r - r_j) \tag{2.1}$$

where $\phi_0 = hc/2e \simeq 2 \times 10^{-7}$ gauss-cm^2 is the flux quantum and λ is the magnetic penetration depth and r_j is the position of the j-th lattice point. The solution is $K_0(r)$, the zero-order Hankel function of imaginary argument.

$$h(r) = \frac{\phi_o}{2\pi\lambda^2} \sum_j K_0\left(\frac{r-r_j}{\lambda}\right) . \tag{2.2}$$

The interaction energy between two vortices is

$$U_{ij} = \frac{\phi_o^2}{8\pi^2\lambda^2} K_0\left(\frac{r_{ij}}{\lambda}\right) . \tag{2.3}$$

This is a monotonically decreasing function of r and the difference between the FLL and an ordinary atomic crystal lattice is that the interaction force between two vortices is always repulsive and the FLL is held together by the external magnetic field pressure. The elastic constants of the FLL can be derived from the interaction energy of Eq. 2.3. For materials with $\kappa \simeq 1$ such as pure Nb, the vortex core energy is not negligible and the above equations are not valid. When $\kappa \simeq 1$, the full Ginzburg-Landau theory must be used to describe the structure of the vortex lattice in the mixed state (Parks 1969). However, the qualitative behavior of the FLL should be similar to that of the high κ case.

2.2 The Critical State.

In the static equilibrium state which is known as the critical state, the driving force on the FLL is balanced by the volume pinning force. The driving force on the FLL is produced by a gradient in the density of the quantized flux lines or a transport current. The critical state is created as the magnetic field is driven into the superconductor by increasing the applied magnetic field and maintained until the flux lines are driven out as the applied field is reduced. So, in most cases, the FLL is assumed to be always in the critical state.

Friedel et al. (1963) first derived the critical state equation employing a thermodynamic approach. They considered a system of a fixed number N of straight flux lines of unit length in an area A. The magnetic field pressure p at a temperature T can be written as

$$p = -\left.\frac{dF}{dA}\right|_{T,N} = -f - A\left.\frac{df}{dA}\right|_{T,N}$$

$$= -f + B\left.\frac{df}{dB}\right|_{T,N}, \tag{2.4}$$

since $d(N\phi_o)=d(BA)=BdA+AdB=0$, where $F=fA$ is the Helmholtz free energy per unit length and $B=N\phi_o$ is the average magnetic field. The driving force F_d (force per unit

volume) due to a gradient in the flux line density is given by

$$F_d = -\frac{dp}{dx} = -\frac{dB}{dx}\frac{dp}{dB} = -B\frac{dB}{dx}\frac{d^2f}{dB^2}. \tag{2.5}$$

The Gibbs free energy, $q=f-(BH/4\pi)$, is minimum in isothermal equilibrium and in the presence of an applied field H. Thus, in equilibrium, the reversible B-H relation, $B_{eq}(H,T)$ is determined by

$$\frac{dq}{dB} = \frac{df}{dB} - \frac{H}{4\pi} = 0,$$

or

$$H = 4\pi\frac{df}{dB}. \tag{2.6}$$

Therefore, the driving force F_d is

$$F_d = -\frac{H}{4\pi}\frac{dB}{dx}\left(\frac{dH}{dB}\right)_{eq} = -\frac{B}{4\pi\mu_{eq}}\frac{dB}{dx} = -\frac{B\,J}{10\mu_{eq}}, \tag{2.7}$$

where

$$J_c\ (\text{amps/cm}^2) = \frac{10}{4\pi}\frac{dB}{dx}\ (\text{gauss/cm})$$

and $\mu_{eq}(H)=dB_{eq}/dH$. The critical state is established when the driving force is just matched by the volume pinning force. The volume pinning force, F_v, can be calculated by

$$F_v = - F_d = \frac{B}{4\pi\mu_{eq}} \frac{dB}{dx} = \frac{B\ J_c}{10\ \mu_{eq}} \quad . \tag{2.8}$$

The volume pinning force can be measured indirectly by measuring the magnetic field profile inside the superconductor (Sec. 4.4).

2.3 Elastic Properties of the Flux Line Lattice.

2.3.1 Elastic Constants of the Flux Line Lattice.

The elastic properties of the FLL can be described by the elastic constants $c_{\mu\nu}$. The relation between the stress s_μ and the strain e_ν is (Kittel 1971)

$$s_\mu = \sum_\nu c_{\mu\nu}\ e_\nu \tag{2.9}$$

by the Hook's law. If the z axis is taken parallel to the vortex lines, the displacements of the vortex lines parallel

to the z axis leave the lattice unchanged and the forces are independent of e_{zz}. The remaining stress-strain relation can be written as

$$\begin{pmatrix} s_{xx} \\ s_{yy} \\ s_{yz} \\ s_{xz} \\ s_{xy} \end{pmatrix} = \begin{pmatrix} c_{11} & c_{12} & & & 0 \\ c_{12} & c_{11} & & & \\ & & c_{44} & & \\ & & & c_{44} & \\ 0 & & & & c_{66} \end{pmatrix} \begin{pmatrix} e_{xx} \\ e_{yy} \\ e_{yz} \\ e_{xz} \\ e_{xy} \end{pmatrix} \tag{2.10}$$

where

$$e_{xy} = \frac{du_x}{dy} + \frac{du_y}{dx}$$

and $\vec{u}$ is a distortion of flux lines. The relation between the elastic constants of the flux line lattice is

$$c_{66} = \frac{1}{2} (c_{11} - c_{12}) . \tag{2.11}$$

The shear modulus c_{66} is very small compared to the bulk modulus c_{11}, and c_{11} and c_{12} are usually considered equal.

These four elastic constants can be obtained from the reversible B-H relation, $B_{eq}(H)$, as follows (Labusch 1967 and 1969b):

$$c_{11} = c_{12} = \frac{B}{4\pi\mu_{eq}} ; \tag{2.12}$$

$$c_{44} = \frac{B_{eq}H}{4\pi} ; \tag{2.13}$$

$$c_{66} = \frac{1}{8\pi}\int_0^B B'^2 \frac{d^2H(B')}{dB'^2}\, dB' ,$$

when $B \ll B_{c2}$;

$$c_{66} = \frac{0.48}{4\pi} \frac{H_c^2 \kappa^2 (2\kappa^2 - 1)}{[1 + \beta_A (2\kappa^2 - 1)]^2} \left(1 - \frac{B}{B_{c2}}\right)^2 ,$$

when $B \simeq B_{c2}$; (2.14)

where $\beta_A = 1.16$ for a triangular lattice. For a high κ material and when the H field is near H_{c2}, the elastic constants can be approximated by

$$c_{11} = c_{12} = c_{44} = \frac{1}{4\pi} H_{c2}^2 b^2 ; \tag{2.15}$$

$$c_{66} = \frac{0.13}{4\pi\kappa^2} H_{c2}^2 (1-b)^2 ,$$

when $B \simeq B_{c2}$; (2.16)

where $b = B/B_{c2}$.

All the FLL elastic constants increase sharply as the magnetic field increases but c_{66} decreases to zero again as the field approaches H_{c2} while the others keep increasing up to H_{c2}. The magnitude of c_{66} is, even when the field is close to H_{c1}, several orders smaller than the other elastic constants (Fig. 2.1).

2.3.2 Displacements of Flux Lines due to Local Forces.

The displacements of the FLL due to a point pinning force can be found by using the elastic theory of an isotropic continuum. If density of pinning centers is low, the displacement u_0 of the flux lattice under the influence of a point force, f_p, acting perpendicularly to the flux line direction is (Labusch 1969b)

$$u_0 = \frac{f_p}{4\pi c_\ell r_0} \tag{2.17}$$

where

$$c_\ell = (3\, c_{44} c_{66}/2\pi)^{1/2}$$

and

$$r_o = (2\phi_o/\sqrt{3}\, B)^{1/2}$$

If the pinning center density is not so dilute, the neighboring pinning centers tend to limit the displacement. On the other hand, if the spacing between the pinning centers becomes very small, the pinning centers may act cooperatively and the displacement becomes larger than given in the Eq. 2.17. However, the displacement of the flux lines due to the pinning force is generally very small except at fields very close to H_{c1} or H_{c2} (Fig. 2.3).

Kramer (1973) introduced a line pinning model. The pinning centers separated by L_z on a flux line may act cooperatively as a line pinning center rather than acting individually as point pinning centers and the displacement, u_o, is given by

$$u_o = f_p \sqrt{\frac{B}{\phi_o}} \; \frac{1}{2\sqrt{c_{44}c_{66}}} \; \coth\left(\frac{L_z}{2l^+}\right) \tag{2.18}$$

where

$$l^+ = (c_{44}\phi_o/c_{66}B)^{1/2}$$

For a concentrated array of the pinning centers, the above equation becomes (Kramer 1973, Ullmaier 1975)

$$u_0 = \frac{f_p}{L_z} \frac{1}{2\, c_{66}} . \tag{2.19}$$

Because of the strong coupling of vortex lines to each other, their displacements due to the pinning force are also very small in the line pinning case except in the field regions very close to H_{c1} and H_{c2} where the shear modulus c_{66} is very small.

Figure 2.1 The FLL elastic constants for a NbTa alloy with $T_c = 7.1^\circ K$, $\kappa = 3.4$ at $T = 4.2^\circ K$ (Ullmaier 1975).

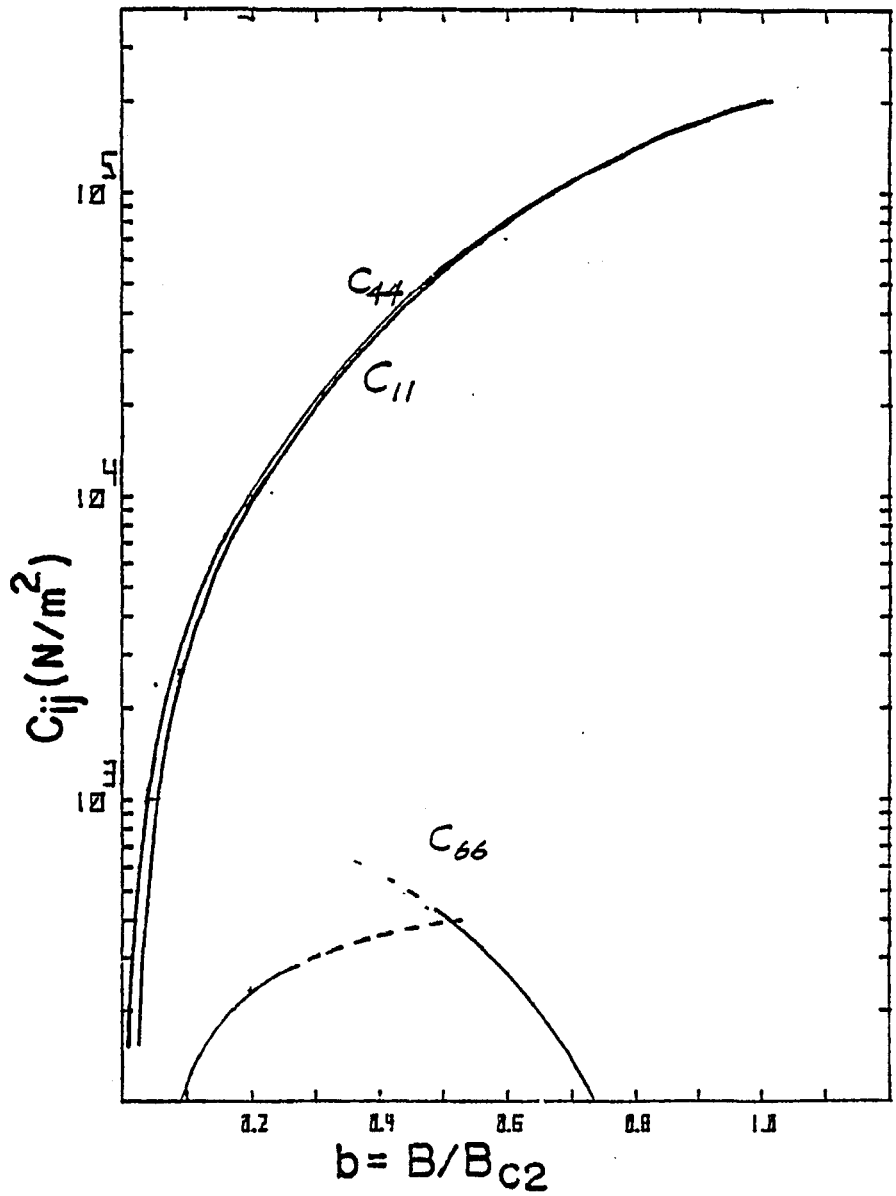
C_{44}
C_{11}
C_{66}
$C_{ij}(N/m^2)$
10^5
10^4
10^3
0.2
0.4
0.6
0.8
1.0
$b = B/B_{c2}$

Figure 2.2 The FLL elastic constants for pure niobium with H_{cz}= 2.71 KOe at T = 4.2°K (Anjaneyulu 1977).

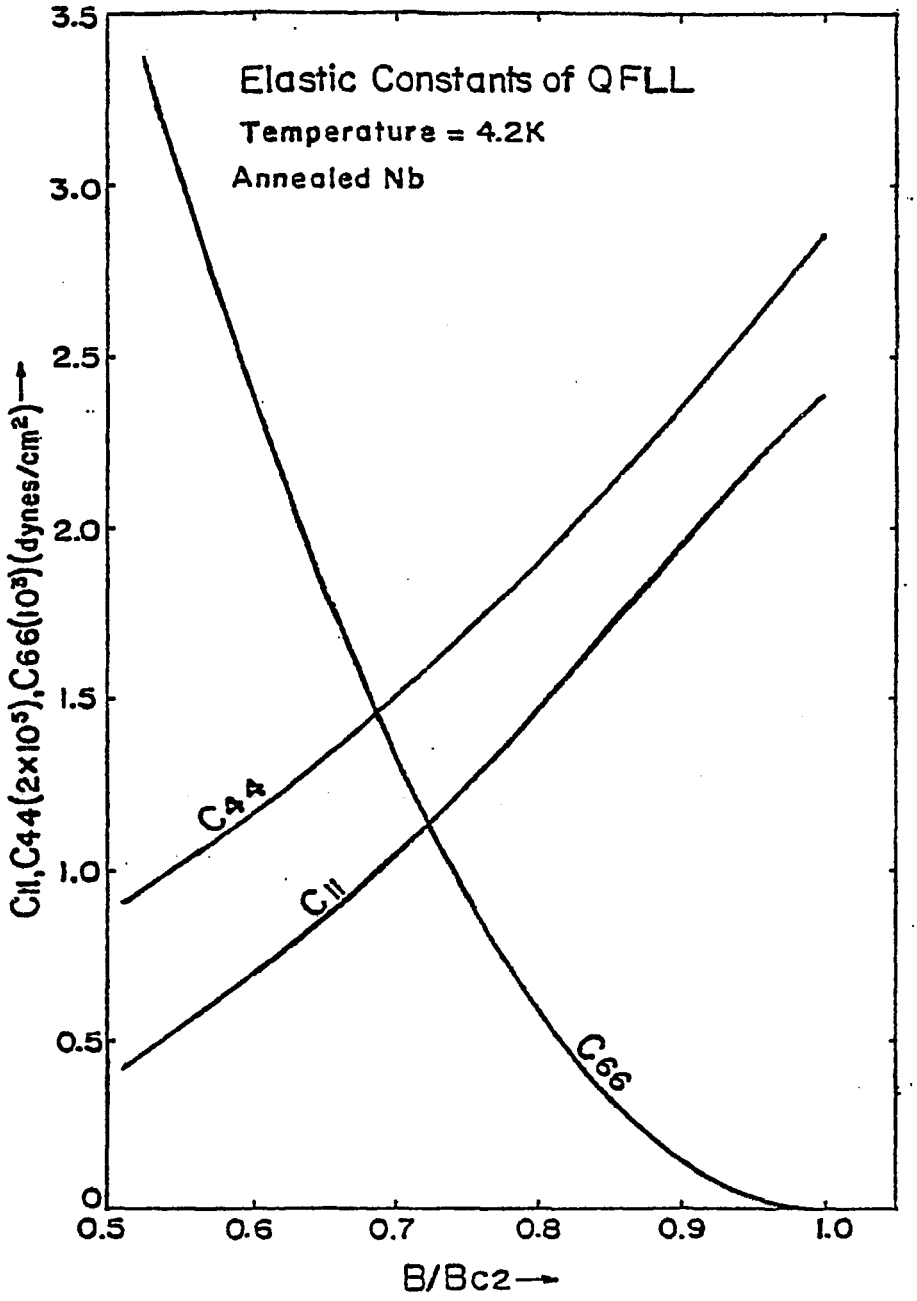
Elastic Constants of QFLL
Temperature = 4.2K
Annealed Nb
C44
C11
C66
C11,C44(2×10⁵),C66(10³)(dynes/cm²)→
B/Bc2→
3.5
3.0
2.5
2.0
1.5
1.0
0.5
0
0.5
0.6
0.7
0.8
0.9
1.0

Figure 2.3 The maximum displacement of the flux lines, s(0), relative to the FLL constant, d, vs. the reduced field $b=B/B_{c2}$ for a maximum pinning force exerted by a normal inclusion of volume ξ^3 where ξ is the coherence length and κ is the Ginzburg-Landau parameter (Schmucker and Brandt 1977).

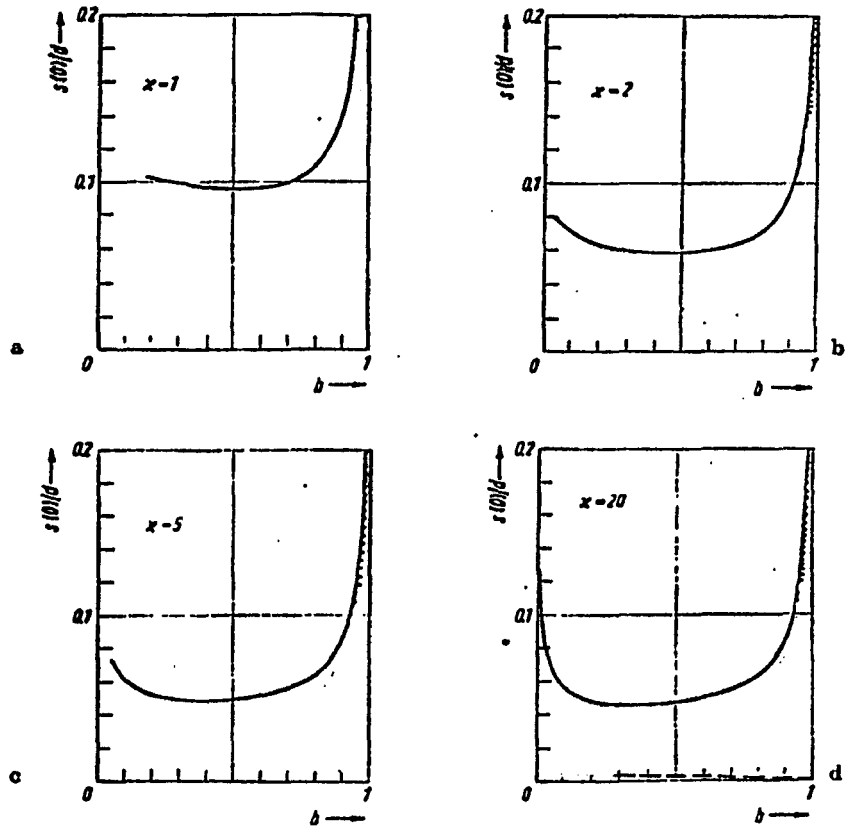
a
b
c
d
x=1
x=2
x=5
x=20
0.2
0.1
0
1
b

2.4 Flux Line Lattice Defects.

Labusch (1966) first predicted the existence of dislocations in the FLL and, shortly afterward, Essman and Trauble (1967) developed a technique which enabled them to observe the FLL directly at low vortex density. They found dislocations with various other defects such as vacancies, interstitials, stacking faults, and grain boundaries in the FLL (Fig. 2.4). Even though the existence of various defects in the FLL is a generally accepted fact, how these defects are created and how they affect the superconducting properties are not well understood at the present time.

The line defects like vacancies and interstitials are observed in a very narrow range of low vortex densities. In their measurements on Pb-6.3% In, Trauble and Essman found line defects for the field between 30 gauss and 60 gauss. When the field is below 30 gauss, the vortex lattice becomes fluid like and ceases to form a lattice and, when the field is above 60 gauss, the density of line defects decreases rapidly to one line defect to every 10,000 vortex lines. However, this is still orders of magnitude too high for those defects to be in thermal equilibrium. It was suggested that the pinning centers may determine the concentration of line defects (Hill et al. 1969) or that these line defects are produced during the formation of the FLL (Ullmaier 1975). Nevertheless, the influence of the line defects on the

macroscopic behavior of the FLL is thought to be very small except when the field is very close to H_{c1} (Brandt 1969).

Dislocations, in contrast to the line defects, are high in density and could play a substantial role in flux pinning. It is generally believed that the vortex density gradient is accomplished by the introduction of edge dislocation lines (Essman and Trauble 1969). There are also some strong indications that the dislocations can affect the volume pinning force in some cases. Campbell and Evetts (1972) found that the critical current in some superconductors varied by a factor of three or more depending on the way in which FLL dislocations were introduced into the FLL. Chang et al. (1969) first pointed out the similarity between the stress-strain curve in mechanical tests and the flux flow voltage-current characteristics. They suggested that the critical transport current should be described entirely in terms of the pinning of the FLL dislocations. Campbell and Evetts argued against this idea on the grounds that the dislocations created by the vortex density gradient have their glide plane parallel to the transport current and experience no force along the glide planes. Therefore, the presence of these dislocations should not affect the outcome. However, the dislocations with their glide plane perpendicular to the transport current may affect the outcome even if they are lower in density than those responsible for the vortex density gradient (chapter 6).

Grain boundaries were also found in the FLL but there are not enough experimental results to outline their effect on pinning. At the present time, there is no clear understanding of the effect of the FLL defects on the pinning in general regardless of their type.

Figure 2.4 The electron micrographs of the flux line lattice in lead-indium (Trauble and Essmann 1968).
$B = 70$ gauss, $\kappa = 2$, $T = 1.2^{\circ}K$.
(a) Dislocations in the FLL.
(b) Edge dislocation.
(c) Extended dislocation (stacking fault).
(d) Grain boundary.

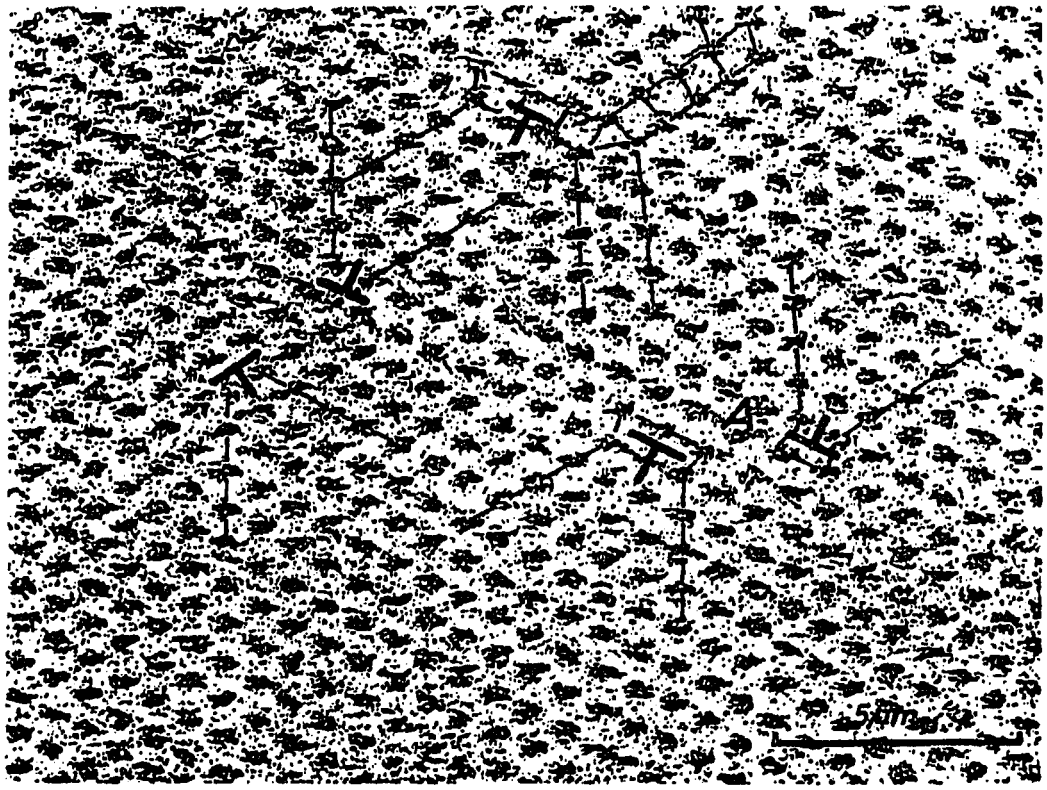

(a)

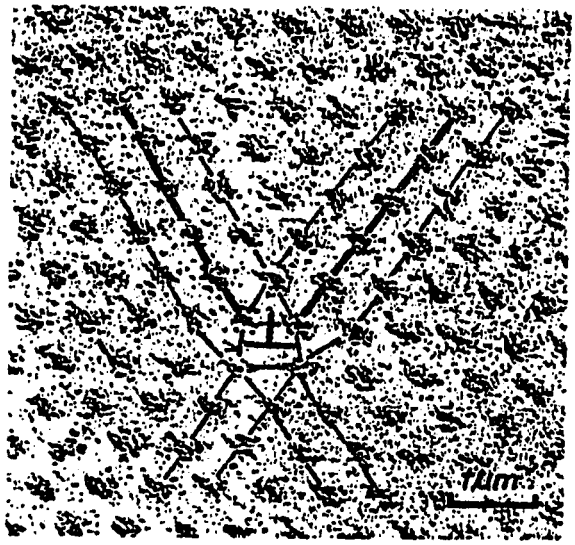

(b)

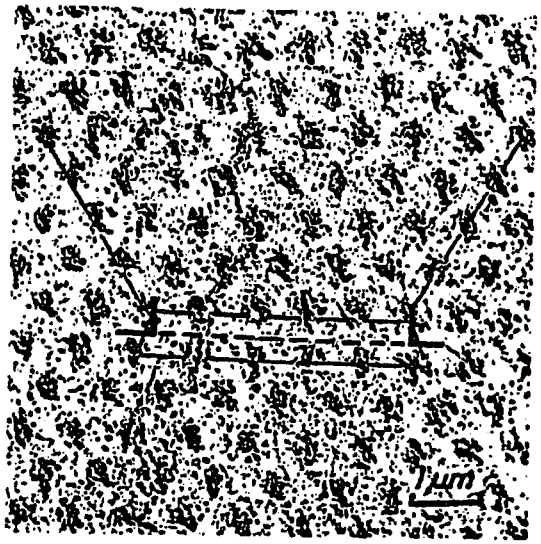

(c)

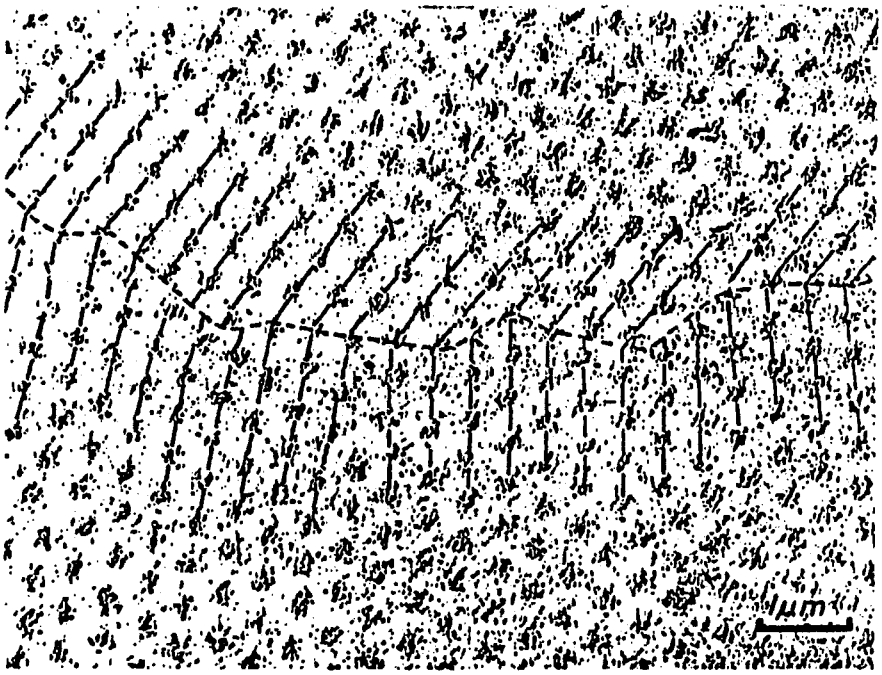

(d)

Chapter III

REVIEW AND CRITIQUE OF CURRENT FLUX PINNING THEORIES

A complete magnetic flux pinning theory requires an understanding of the elementary pinning force f_p, the maximum interaction force between a pinning center (crystalline defect) and the FLL, and of the proper summation of these local forces into the volume pinning force F_V.

3.1 Pinning Mechanisms.

Local changes of superconducting properties such as electron density of states, electron-phonon interaction and electron mean-free-path, etc. due to inhomogeneities in a type II superconductor in the mixed state result in the position dependence of the free energy of the flux line lattice. There are several different pinning mechanisms and, for a given defect structure, estimates of the relative importance of these machanisms can be made. For such estimates, it is practical to divide the field between H_{c1} and H_{c2} into two regions. In the low field region, the vortex lines are treated individually and the free energy of

a vortex line is split into contributions from the vortex core and from the surrounding magnetic field and current. In the high field region, the FLL is described by the Ginzburg-Landau theory with approximation methods utilized when the normalized Ginzburg-Landau order parameter, ψ, is small.

a) Core Interaction: At the center of a quantized flux line, the order parameter is zero and this adds a positive contribution to the free energy of the flux line (condensation energy). If the material has some region in which the order parameter is already zero or reduced from its value in the matrix, the flux lines tend to pass through this region to keep the free energy increase at a minimum.

b) Magnetic interaction: The free energy of a vortex line is the sum of the magnetic field energy and the kinetic energy of the vortex current in addition to the condensation energy. The presence of inhomogeneities causes local changes in the magnetic field and current densities to occur, affecting the field and current distributions of the vortex lines. Thus, the shape of the field and current distribution of a flux line changes as it moves through an inhomogeneous superconductor and so does the free energy.

c) Elastic interaction: The specific volume and the elastic compliance of a metal in the normal state is slightly smaller than in the superconducting state and this difference gives rise to a stress around a quantized flux

line. If a stress field already exists in the superconductor, the stress field due to the FLL couples with it and results in a position dependent total free energy.

3.2 Summation Rules and Threshold Criterion.

The volume pinning force F_V is the combined force of a large number of individual interaction forces between the pinning centers and the FLL. If $\rho(F)\,dF$ is the number of the interactions per unit volume with forces between F and F+dF, the volume pinning force F_V can be written as

$$F_v = \int_{-f_p}^{f_p} F \; \rho(F)\; dF \; . \tag{3.1}$$

The elementary pinning force f_p is the maximum force a pinning center of a given type can exert on a flux line. A straight forward evaluation is possible for two limiting cases:

a) If the FLL as well as the crystal lattice is completely rigid and there is a sufficiently large number of statistically distributed pinning centers, F_V would be zero.

b) If the FLL is completely soft so that every

pinning center contributes its maximum force f_p, or if the elementary pinning forces are so strong that the vortex lines move and arrange themselves such that each pinning center contributes its maximum force, the volume pinning force is a simple sum of the elementary pinning forces f_p.

$$F_v = - N_v f_p \qquad \text{direct summation rule,} \tag{3.2}$$

where N_v is the density of the pinning centers.

In the general case, however, the summation is a quite difficult problem. Let's consider the one dimensional case for its simplicity. In a one dimensional model, a pinning center can be characterized by a potential well $U(x)$ and the corresponding pinning force F (Lowell 1972)

$$F = - \frac{dU(x)}{dx} . \tag{3.3}$$

F will displace vortex lines by $u(x)$ which causes an elastic counter force $-C'u$ due to the interaction of the flux lines with each other.

$$C'u(x_0) = \left. \frac{dU(x)}{dx} \right|_{x_0+u(x_0)} ,$$

or

$$C'u(x_0) = \left.\frac{dU(x)}{dx}\right|_{x_0} + \left.\frac{d\ U(x)}{dx}\right|_{x_0} u(x_0) .$$

Thus,

$$u(x_0) = \frac{\left.\frac{dU(x)}{dx}\right|_{x_0}}{C' - \left.\frac{d^2U(x)}{dx^2}\right|_{x_0}} . \tag{3.4}$$

Since the well potential $U(x)$ can be assumed to be an even function, the distortion of flux lines $u(x)$ should be an odd function if $d^2U/dx^2 < C'$ for all x and the net force is zero. Thus, the condition $d^2U/dx^2 = C'$ represents a threshold criterion below which the pinning center results in zero net pinning force on the FLL.

On the other hand, when $d^2U/dx^2 > C'$, then there exists a point beyond which the vortex lines move abruptly until the pinning force F becomes equal to $-C'u$ again because F increases more rapidly with respect to x than the elastic counter force $-C'u$ in this case (Fig. 3.1). On the front side of the potential well, the unstable motion starts before F reaches f_p and stops after passing the maximum which makes the effective maximum force f_e smaller than f_p. However, this instability does not occur until F reaches f_p on the rear side of the potential well. Due to this

asymmetry, the volume pinning force F is not zero in this case. The exact form of $\rho(F)$ will depend on the details of the potential well of the pinning center but may be assumed to be constant for $-f_e < F < f_p$ and zero otherwise. If the FLL is displaced by a distance dx_o, each flux line will contact $N_v L_y\, dx_o$ new pinning centers per unit length where N_v is the pinning center density and L_y is their effective length in the direction perpendicular to the flux lines and the driving force (Ullmaier 1975). Since there are B/ϕ_o flux lines per unit area,

$$\rho(F)\ dF = \frac{B}{\phi_o} N_v L_y\, dx_0 .$$

The displacement dx_o is equivalent to a force change $dF = C' du \doteq C' dx_o$. Therefore,

$$\rho(F) = \frac{B}{\phi_o} \frac{N_v L_y}{C'} . \tag{3.5}$$

From Eq. 3.1,

$$F_v = \frac{B}{\phi_o} \frac{N_v L_y}{C'} \int_{-f_e}^{f_p} F\, dF$$

$$= \frac{B}{\Phi_o} \frac{N_v L_y}{C'} (f_p^2 - f_e^2) . \tag{3.6}$$

When $d^2U/dx^2 >> C'$, f_e is small compared to f_p and the volume pinning force is approximately quadratically proportional to the elementary pinning force.

$$F_v = \frac{B}{\Phi_o} \frac{N_v L_y}{C'} f_p^2 . \tag{3.7}$$

FLL instability model (Labusch's quadratic summation model)

F decreases as the rigidity of the FLL increases and it does not depend on whether the interaction is attractive or repulsive (Labusch 1969a).

Figure 3.1 The free energy U and the interaction force $F=-dU(x)/dx$ of a flux line with an elastic constant C' (dotted line) passing through a pinning center.

(a) When $d^2U(x)/dx^2$ is always smaller than C', the flux lines are stable for the whole pinning range.

(b) When the maximum value of $d^2U(x)/dx^2$ exceeds C', the instability occurs on both sides of the potential well but the pinning force never reaches the maximum value f_p on one side of the pinning center.

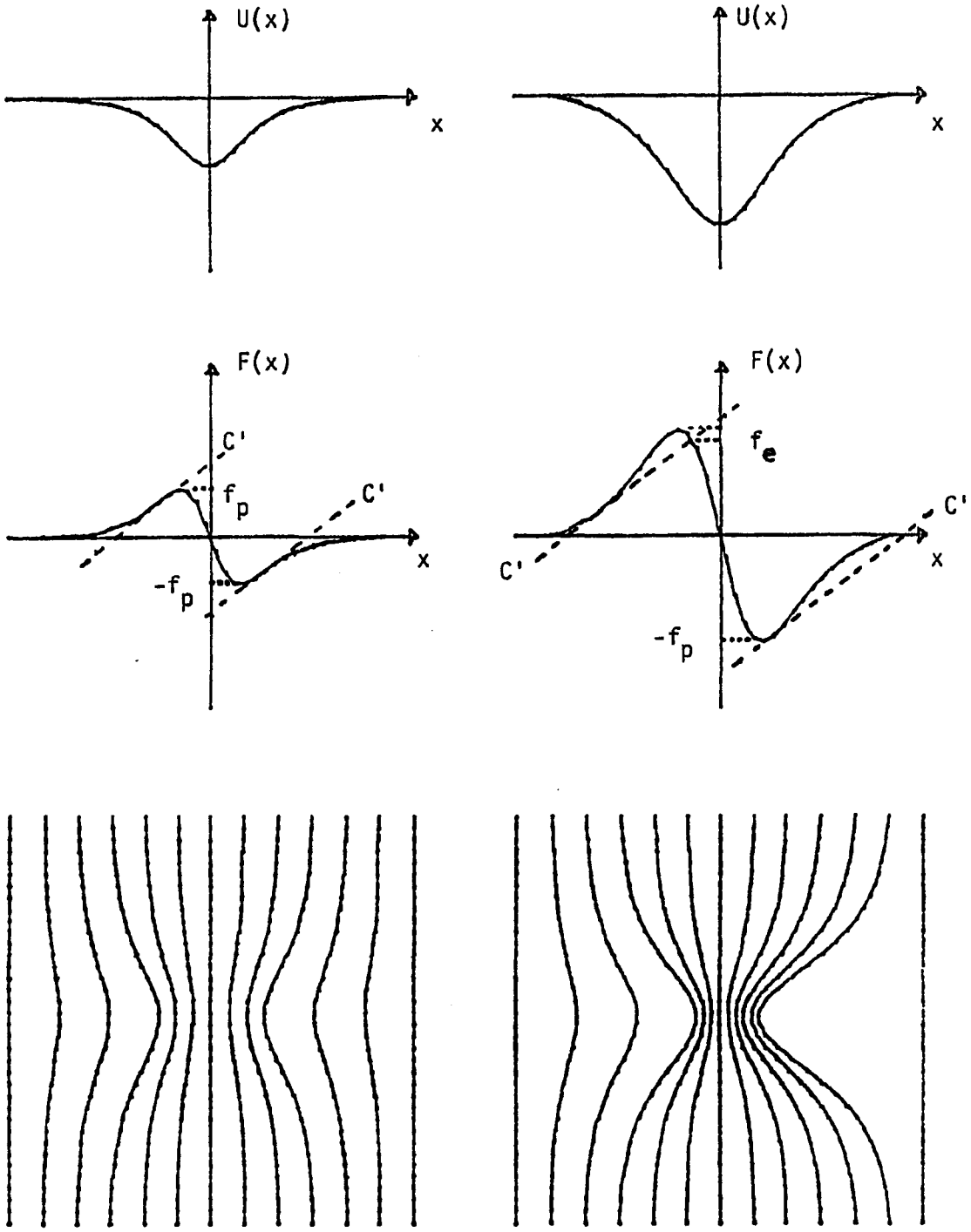

(a) (b)

3.3 Some Experimental Results and Their Interpretations.

There have been a considerable number of experiments and efforts to correlate the measured volume pinning forces with the present flux pinning theories. However, it seems clear, at present, that neither the direct summation model nor the FLL instability model can explain the experimental results satisfactorily.

If we define a specific volume pinning force Q as the volume pinning force per pinning center (Kramer 1978)

$$Q = \frac{F_V}{N_V}, \tag{3.8}$$

the relation between Q and f_p is $Q = f_p$ for the direct summation model and $Q \propto f_p^2$ for the FLL instability model. However, the curve on which the experimental data points fall lies between the two summation model lines (Fig. 3.2). In the high elementary pinning force region, the experimental data run parallel to the direct summation line but the Q value is about one order of magnitude smaller than the elementary pinning force f_p. As f_p decreases, the slope of a curve through the data becomes steeper until the curve runs nearly parallel to the FLL instability model prediction. The more perplexing fact is that pinning centers whose elementary pinning force is lower by up to

four orders of magnitude than the pinning threshold predicted by the FLL instability model still give rise to a strong volume pinning force. Fietz and Webb (1969) suggested that a number of pinning centers may act together as a super pinning center. However, to explain the low threshold, the super pinning center should include up to 10^5 pinning centers which is too large a cluster to be considered as a point pinning center. Also, the fact that the specific volume pinning force is nearly independent of the pinning center density make this suggestion hard to accept.

Experimental measurements of the volume pinning force as a function of the magnetic field in proton or neutron irradiated superconductors show a small sharp peak just below H_{c2} at low irradiation fluences. The height of the peak increases and shifts to lower fields while becoming much broader as the fluence increases (Sec. 5.3). If a synchronization of the flux line distance and the pinning center spacing occurs, all the pinning centers can act cooperatively and produce a bulk pinning force much larger than in the general case where the lattice must be distorted in order to produce a non-zero volume pinning force. Such effects have been observed experimentally (Fig. 3.3) but do not represent the situation described above. It is suspected that FLL softening because $c_{66} \rightarrow 0$ at fields close to H_{c2} might cause the peak effect. But if this is the

case, the FLL instability model would predict that the peak effect should occur at a field closer to H_{c2} than observed.

Some samples which display the peak effect also display a volume pinning force which is dependent on the magnetic field history (Kupfer and Gey 1977). At a field below the peak, the volume pinning forces of these samples are higher when they are brought up to a given applied field from below H_{c1} (cycled state) than when they are brought down to the same applied field from above H_{c2} (non-cycled state). See Fig. 3.4. It has been proposed that the FLL defects might be the cause of this cycling effect. The elastic constants of the FLL are affected by the FLL defects, and the type or density of the FLL defects might depend on the magnetic field history (Kupfer and Gey 1977).

Figure 3.2 The specific pinning force Q vs. the elementary pinning force for defects in Nb at b=.55 at T=4.2°K (Kramer 1978).

□ Dislocation loops.

○ Voids produced by neutron irradiation at high temperature.

● Voids produced by Ni^+ bombardment at high temperature.

△ Large Nb N precipitates in Nb.

⊠ Dislocation loops produced by proton irradiation at room temperature (Anjaneyulu and Rollins 1979).

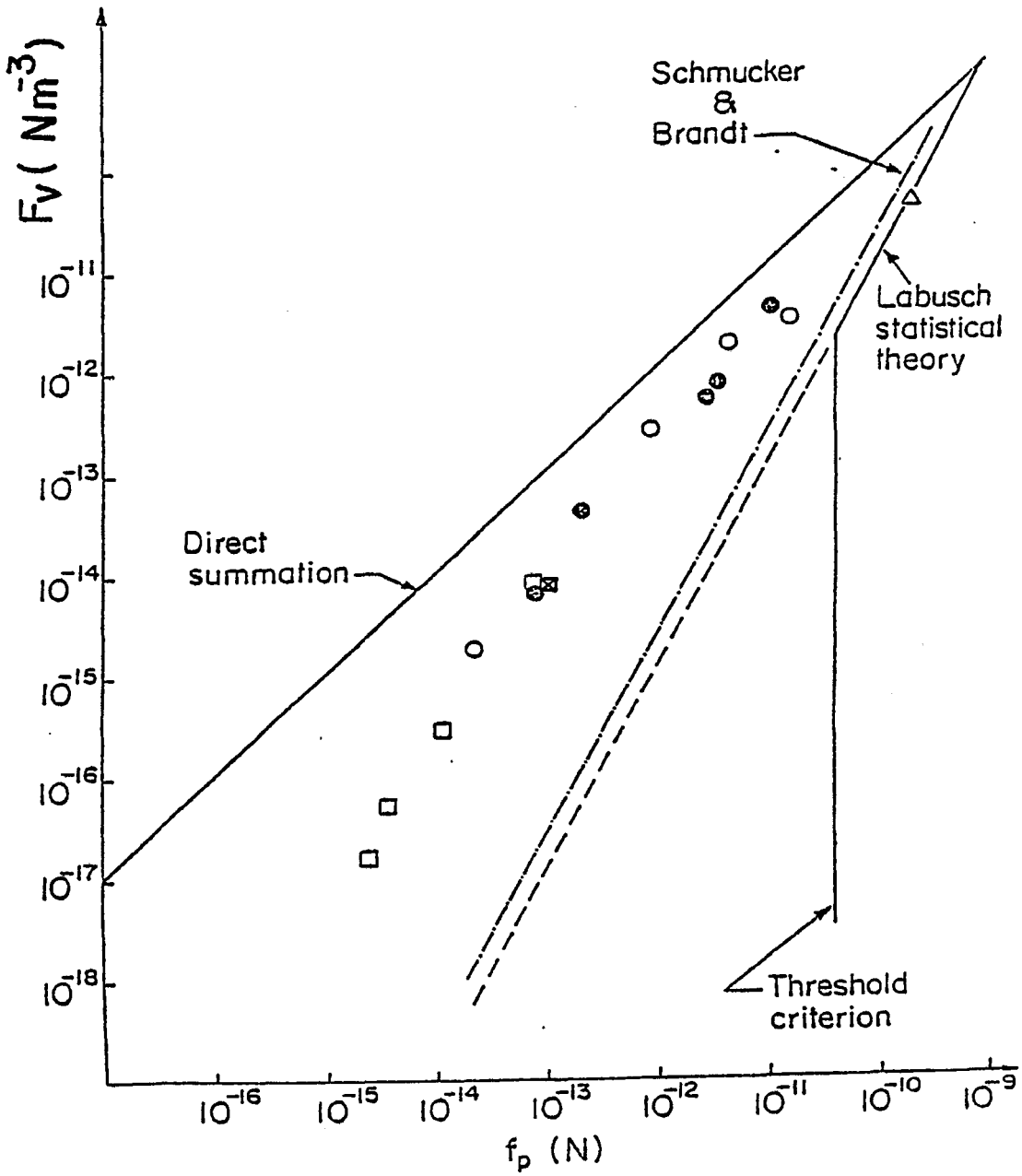
F_V (Nm^{-3})
10^{-11}
10^{-12}
10^{-13}
10^{-14}
10^{-15}
10^{-16}
10^{-17}
10^{-18}
Schmucker & Brandt
Labusch statistical theory
Direct summation
Threshold criterion
10^{-16}
10^{-15}
10^{-14}
10^{-13}
10^{-12}
10^{-11}
10^{-10}
10^{-9}
f_p (N)

Figure 3.3 The volume pinning force as a function of flux density B in NbTi containing an ordered array of alpha-precipitates. The pinning center spacing matches multiples of the flux line distance (Hillmann and Hauck 1972).

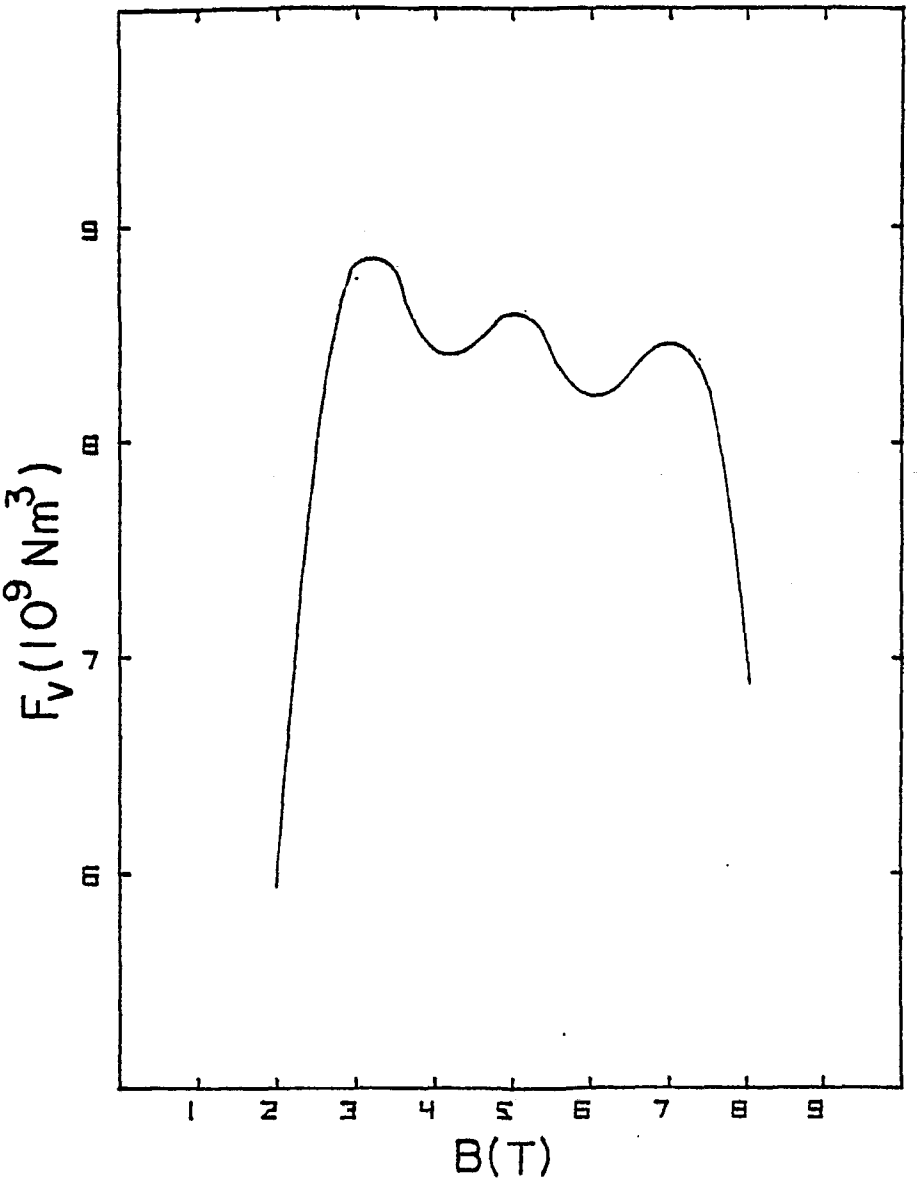
$F_v(10^9 Nm^3)$
6
7
8
9
1
2
3
4
5
6
7
8
9
B(T)

Figure 3.4 (a) Three different ways to reach the same temperature and applied field: (i) the "non-cycled" state (nc) reached by reducing the applied field from above $H_{c2}(T)$ at constant temperature; (ii) the "cycled" state (c) reached by increasing the applied field from zero at constant temperature; (iii) the "heated" state (h) reached by cooling the sample from above the critical temperature at constant applied field.

(b) Measurements of reduced volume pinning force F_v/F_v^{max} vs. reduced magnetic field $b=B/B_{c2}$ for several samples (Kupfer and Gey 1977).

——— non-cycled state (nc)

– – – – cycled state (c)

—·— heated state (h)

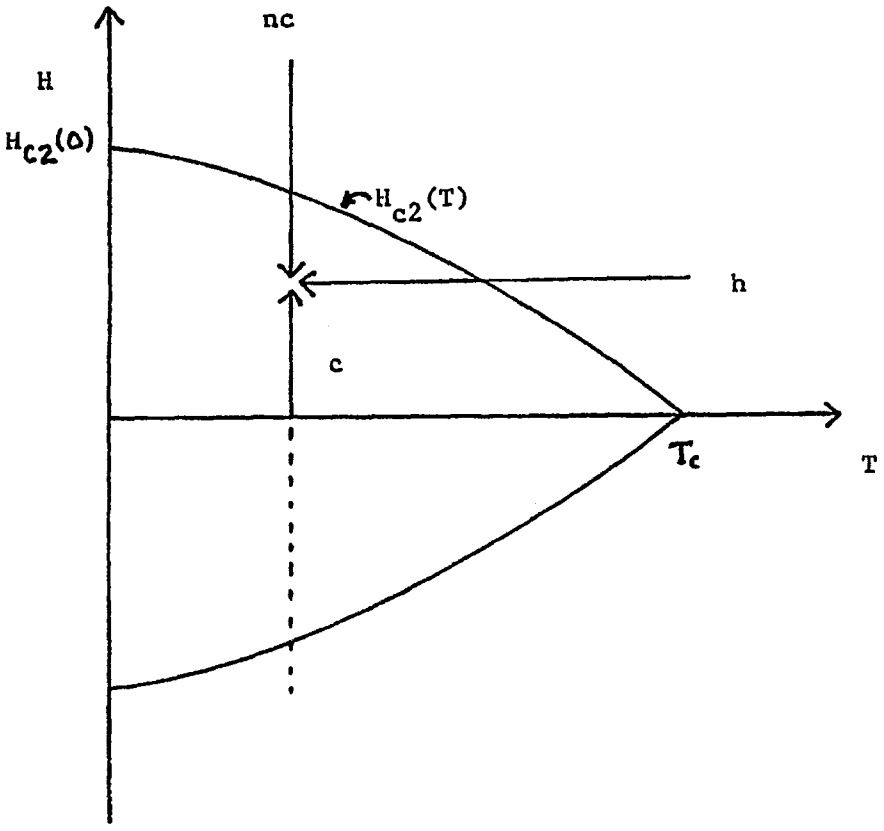

(a)

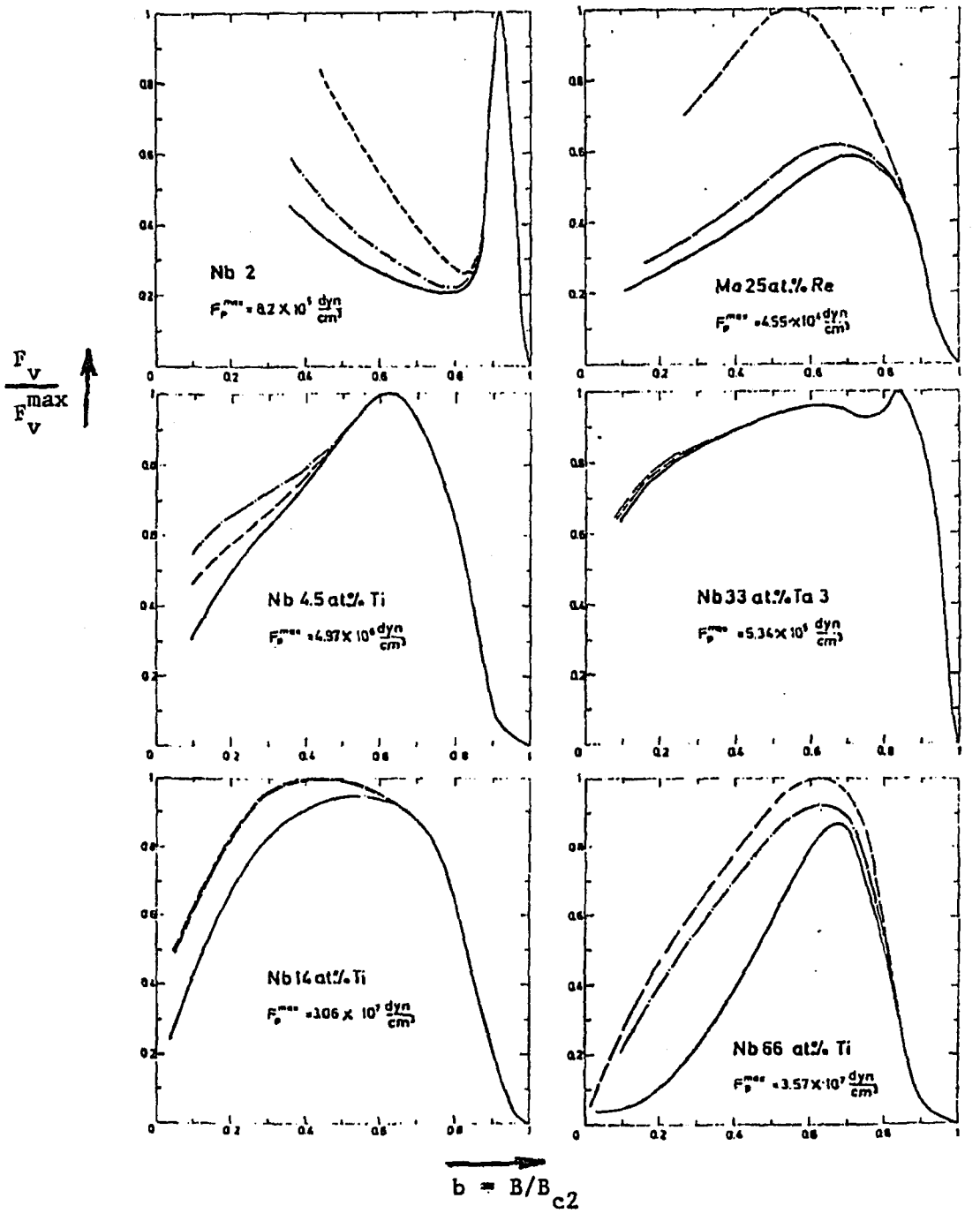
Nb 2
$F_p^{max} = 8.2 \times 10^5 \frac{dyn}{cm^3}$
Mo 25 at.% Re
$F_p^{max} = 4.55 \times 10^6 \frac{dyn}{cm^3}$
Nb 4.5 at.% Ti
$F_p^{max} = 4.97 \times 10^6 \frac{dyn}{cm^3}$
Nb 33 at.% Ta 3
$F_p^{max} = 5.34 \times 10^5 \frac{dyn}{cm^3}$
Nb 14 at.% Ti
$F_p^{max} = 3.06 \times 10^7 \frac{dyn}{cm^3}$
Nb 66 at.% Ti
$F_p^{max} = 3.57 \times 10^7 \frac{dyn}{cm^3}$
$\frac{F_v}{F_v^{max}}$
$b = B/B_{c2}$

(b)

Chapter IV

EXPERIMENTAL TECHNIQUES EMPLOYED

The sample preparation procedure and the experimental methods used in the proton bombardment and the field profile measurements are virtually identical with those described by Anjaneyulu (1977).

4.1 Sample Preparation.

The samples were prepared from zone-refined (MARZ grade) niobium rods (6.3 mm diameter) purchased from Materials Research Corporation. The niobium rods were chemically etched in a solution consisting 3 parts HNO_3 (70 % concentration) and 2 parts HF (48 % concentration) for about two minutes to remove their possibly contaminated surfaces and then swaged into rods with a diameter of 4.8 mm. Samples 4 cm long were cut from the swaged rods with a carborundum saw, and a 1.5 mm diameter blind hole was drilled along the center of each sample for water circulation during the proton bombardment. A 0.75 mm hole was drilled at the open end of each sample for hanging in an induction furnace during annealing. The drilled samples

were cleaned in acetone and the both outer and inner surfaces were chemically etched in the acid solution described above for about two minutes to remove the strained and contaminated surface. They were washed immediately afterward in distilled water and methyl alcohol. The chemical etching produced rough, pitted surfaces due to the strain produced by the swaging. These samples were again polished mechanically using 320, 400, and 600 grade emery paper and finally with L15 grade crocus cloth until smooth, shiny surfaces were obtained.

After being thoroughly washed, the samples were hung one at a time in the work coil of a vacuum induction furnace by the hanging hole. The vacuum chamber was pumped at least 6 hours until the pressure reached $2x10^{-7}$ torr before the annealing started. The samples were initially annealed at a temperature between 1800°C and 1920°C (as measured by an optical pyrometer) to remove the material strain which might cause preferential evaporation. The temperature was then raised to within 30°~80°C of the melting point and the sample was annealed for at least 12 hours. The temperature was raised in one step to minimize the absorption of gas by the sample at intermediate temperatures. The pressure in the vacuum chamber at the end of annealing was $2 \sim 3.7 \times 10^{-7}$ torr. After annealing, the samples were left to cool in the chamber for at least 6 hours at a vacuum less than $1x10^{-7}$ torr. The resitivity ratios of some of the annealed

samples were measured. The resistivity ratio measurement reintroduced some strain and therefore these samples were reannealed. The samples lost about 15 % of their weight during the process of etching, polishing and annealing. Immediately after the final annealing, each sample was epoxied to a 1 cm long copper base at its open end and they were afterward handled only by the copper base. The annealed samples were always kept in a desiccator.

4.2 Resistivity Ratio.

The electrical resistivity of most metals at room temperature is dominated by collisions of the conduction electrons with lattice phonons and is not affected by impurity atoms or crystalline defects (Kittel 1971). However, the resistivity at liquid helium temperature (residual resistivity) is mostly caused by the scattering of the electrons by impurity atoms and crystalline defects. The ratio of the resistivity of a specimen at room temperature to the resistivity at liquid helium temperature reveals the imperfections of the metal.

The resistivity measurements of the annealed niobium samples were made using a standard four leads technique. Copper clamps at each end of the sample served as the

current leads and two point contacts serving as voltage leads were made by two copper nails pressed by springs. A current of 1~7 ampere was supplied by a constant current generator and measured through a 0.1 ohm Leeds and Northrup standard resistor in series with the sample and the voltage across the voltage leads were measured with a Keithley 148 Nano-voltmeter. The voltage and current measurements were made for both polarities of the current to minimize thermal emf effects. The room temperature resistances were measured at the ambient room temperature and 4.2° K resistance measurements were done by immersing the samples in liquid helium and applying a magnetic field of 7 KOe to place the samples in the normal state. The resistivity ratios of the samples at the room temperature to that at the liquid helium temperature were found to be 1400~1900 which indicate very clean samples (DeSorbo 1963).

4.3 Proton Irradiation.

The annealed samples were irradiated with 1 Mev and 3.2 Mev protons supplied by the 11 Mev Tandem van de Graaf accelerator at Ohio University.

The radiation damage station used to irradiate the samples with protons at room temperature is shown in Fig.

4.1. The radiation chamber (4), which was machined from an aluminium block, was connected to the 2" beam line (6) of the accerelator. An aperture 12.3 mm in diameter (5) and a 1 mm by 3 mm rectanqular slit (2) were used to collimate the beam onto the sample. The aperture and slit were constructed from 1.5 mm thick aluminium sheet. The sample (1) was soft soldered to a 10 mil thick, 6.3 mm diameter stainless steel tube (8) by its copper base and a capillary (9) was inserted down to the tip of the sample through the tube. Distilled and deionized water chilled with ice was pumped to the sample through the capillary to keep the sample at room temperature during the proton bombardment. The slit was also cooled by the water circulation.

With the sample pulled out of the way, the proton beam was collimated and tuned to obtain the required beam current on the beam stop (3). The sample was then lowered in the path of the proton beam so that the beam hit the sample surface perpendicularly. The stainless steel tube with the sample was driven by two motors. One motor rotated the sample at the rate of one revolution per second and the other motor moved the sample along the axis 2.5 cm per 24 minutes using a threaded rod arrangement. The radiation chamber was electrically grounded and the electrical impedance between the sample and the ground was about 20 megohm. With the 3.2 Mev proton beam, the current measured on the sample was larger by about 16 % than that

measured on the beam stop with the sample pulled out. It is thought that the secondary electrons ejected from the sample were responsible for the difference, and 84 % of the measured total fluences were considered the real fluences. The apparent beam currents were kept between 3.1 microampere and 3.6 microampere on the samples which represent 2.6 microampere to 3.0 microampere of the real proton current.

Figure 4.1 The radiation damage station.

(1) sample, (2) slit, (3) beam stop

(4) radiation chamber, (5) aperture,

(6) proton beam line,

(7) dynamic vacuum seal,

(8) stainless steel tube, (9) capillary,

(10) linear bearing,

(11) motor (sample rotation),

(12) motor (vertical motion of the sample).

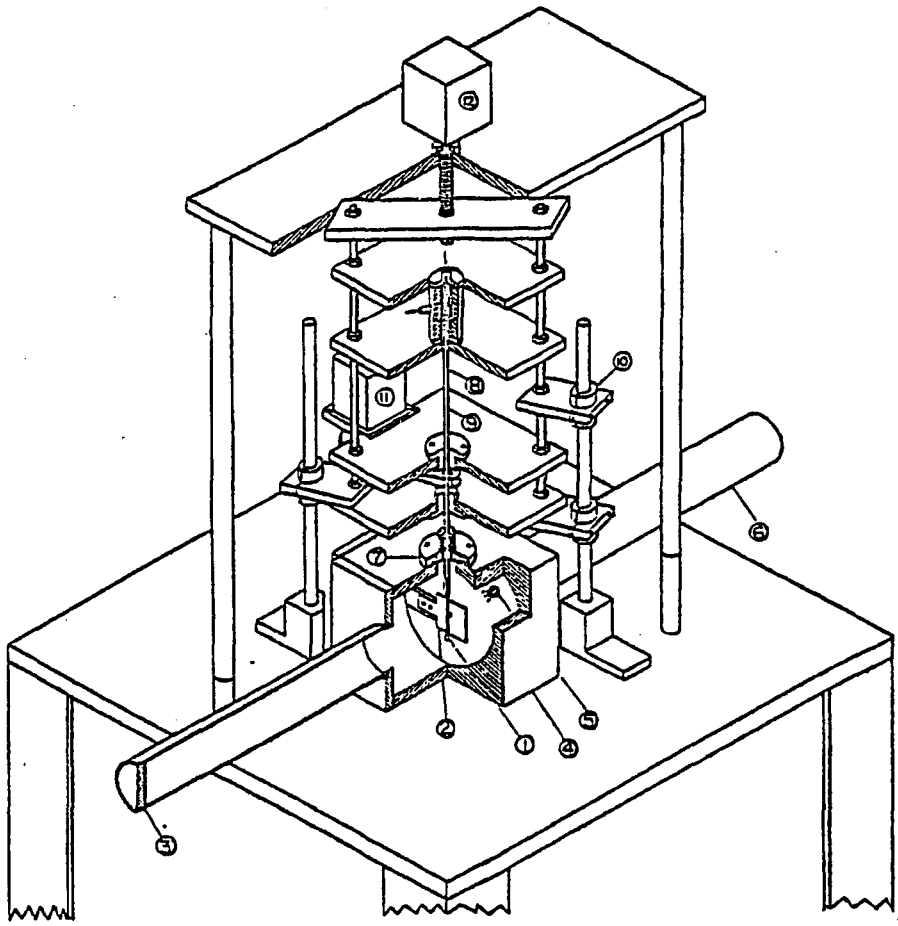

4.4 Magnetic Field Profile.

The volume pinning force may be calculated from the critical current J_c or from the gradient in the flux line density (Chap. 2). The critical current density can be measured by passing a current through a sample in a transverse magnetic field. The current is increased until a certain specified voltage (usually 1 microvolt) is detected across the sample. This method assumes that the current is distributed uniformly and is useful for samples in the form of wire or thin foil.

Rollins et al. (1974) developed an ac method capable of obtaining the magnetic field profile in a bulk specimen. This method makes it possible to study non-homogeneous pinning near the sample surface.

Since a pinning force produces a gradient in the density of flux lines, an oscillatory external magnetic field can penetrate only a certain depth into a type II superconductor which has a pinning force. The critical gradient in B(x) is given by eq. 2.8

$$\frac{dB}{dx} = \pm \frac{4\pi\mu_{eq}}{B} F_V(B,x) \quad , \tag{4.1}$$

where we have indicated that F_V may depend on B and position x. The plus or minus sign in Eq. 4.1 is determined by

whether the flux lines at that point tend to move out of or into the sample. The critical state model assumes that $F_V(B,T,X)$ exists for a given sample and, therefore, Eq. 4.1, together with an appropriate boundary condition determines $B(x)$ throughout the sample. The boundary condition used puts B at the surface equal to $B_{eq}(H,T)$ where H is the applied field.

Rollins et. al. (1974) considered the situation where a small ac field $h_o q(t)$ of amplitude h_o is superimposed on a large dc field H_{dc} applied parallel to a cylindrical sample. Then, at the sample surface, B will oscillate about $B_{av}=B_{eq}(H_{dc})$ with amplitude $b_o=\mu_{eq}h_o$. Furthermore, if $b_o \ll B_{av}$ then Eq. 4.1 simplifies considerably

$$\frac{dB}{dx} = \pm \frac{4\pi\mu_{eq}}{B_{av}} F_V(B_{av}, x) \quad .$$

Fig. 4.2 shows the field profiles which result near the surface of a sample where it is assumed F_V is larger near the surface than in the bulk. The rate of change of flux, $d\phi(t)/dt$, in the sample due to the change in B at the surface $(dB(t)/dt)_S$ is

$$\frac{d\phi(t)}{dt} = \left(\frac{dB(t)}{dt}\right)_s \int_{R-x(t)}^{R} 2\pi r \, dr \tag{4.2}$$

where x(t) is the depth to which the ac field has penetrated at time t. Since $(dB/dt)_s = \mu_{eq} h_o (dq/dt)$, Eq. 4.2 can be rewritten as

$$\frac{d\phi(t)}{dt} = [R^2 - \langle R-x(t)\rangle^2] \, \pi \, \mu_{eq}(H_{dc}) \; h_o \; \frac{dq(t)}{dt} , \tag{4.3}$$

where $\mu_{eq} = dB_{eq}/dH$, and $B_{eq}(H)$ is the reversible B-H relation for the pure material. If the frequency is very low so that the normal skin depth is much larger than the characteristic size of the sample, the change in flux through the sample while in the normal state during the same time interval is given by

$$\frac{d\phi_n(t)}{dt} = \pi R^2 h_0 \frac{dq(t)}{dt} . \tag{4.4}$$

Thus,

$$\frac{x(t)}{R} = 1 - \left[1 - \frac{d\phi(t)/dt}{\mu_{eq}(H_{dc}) \; [d\phi_n(t)/dt]}\right]^{1/2} . \tag{4.5}$$

The internal field B(x) at x(t) during the increasing field

half of the ac cycle is given by

$$B[x(t)] - (B_{av} - b_o) = \frac{1}{2} \mu_{eq}(H_{dc})\ h_o\ [g(t) + 1] \tag{4.6}$$

and during the decreasing field half of the ac cycle is given by

$$B[x(t)] - (B_{av} + b_o) = \frac{1}{2} \mu_{eq}(H_{dc})\ h_o\ [g(t) - 1] \tag{4.7}$$

where $B_{av}=B_{eq}(H_{dc})$ and $b_o=\mu_{eq}h_o$. A plot of $0.5\ \mu_{eq}(H_{dc})\ h_o[g(t)+1]$ vs. $x(t)/R$ with time t as a parameter gives the field profile during the increasing field half cycle and a plot of $0.5\ \mu_{eq}(H_{dc})\ h_o[g(t)-1]$ vs. $x(t)/R$ gives the field profile for the decreasing half cycle. The field profiles cover the depth from the surface of the sample to the maximum penetration depth, $x_{max}(b_o)$.

A block diagram of the electronic circuitry used is shown in Fig. 4.3. A Westinghouse end-compensated superconducting magnet provided the dc field and it was put in the persistent mode whenever the measurements were made. A 1.83 cm in diameter and 9.4 cm long solenoid provided the ac field with amplitude from 1 Oe to 160 Oe. The solenoid was made by winding 3492 turns of 0.0125" diameter copper wire around a copper tube and then potting with epoxy.

This small solenoid produced a peak magnetic field of 0.465 Oe per 1 milliampere of rms current. A 2.3 Hz sinusoidal signal from a Wavetek signal generator was integrated to minimize distortion and connected to a power amplifier before being fed into the small solenoid which served as a priary coil. A 0.5 ohm resistor was connected in series with the primary coil and 0.76 millivolts across the resistor corresponded with an ac field amplitude of 1 Oe. The secondary coil of about 2.5 mm in length was made by winding and potting with epoxy about 1000 turns of #48 copper wire on a teflon tube which fit snuggly around the samples. The sample was inserted in the secondry coil and clamped by its copper base so that the sample and the secondary coil were positioned at the center of the primary coil.

The signal from the secondary coil containing the sample was induced by flux changes not only in the sample but also in the free space between the sample and the secondary coil. The free space part of the signal could be cancelled by superimposing a signal from the compensation system and further corrected by substracting from all other wave forms the compensated wave form measured with the sample in the Meissner state ($H_{dc}=0$). The compensated system consisted of an identical set of primary and secondary coils coaxially arranged. The pair were connected in series and housed antiparallel with respect to

each other in a half inch thick aluminium casing to minimize the external interference. The primary coils of the system and compensation system were also connected in series. The signals from the secondary coils of the system and the compensation system were sent into a PAR # 113 wide band differential pre-amplifier. Its output was connected into an oscilloscope, a PAR Model # HR-8 Phase sensitive lock-in amplifier (for the precision compensation), and also into a Northern NS-550 series digital memory oscilloscope in its averaging mode (Fig. 4.3). The compensated wave forms from the pre-amplifier were accumulated a few hundred times in the memory oscilloscope to improve the signal to noise ratio. The improved wave form was fed for immediate analysis into a programmable Hewlett-Packard 9821-A computer coupled with a plotter. Approximately 200 equally spaced data points were used to store a complete wave form.

The ac magnetic field and the compensation signal were adjusted when the sample was in the non-cycled Meissner state in zero dc field and was not changed throughout the measurement. With $H_{dc}=0$, the compensated signal and the uncompensated signal (representing the signal from the free space between the sample and pick up coil) were acculated 400 times and 100 times respectively and stored. The sample was taken to the normal state by raising the dc field to approximately 7.5 KOe which is well above H_{C3}. The compensated normal signal was accumlated 100 times and

stored to be used as $d\phi_n/dt$ of Eq. 4.4. This normal wave form was compared with the free space part wave form, and the phase was shifted until the zero crossing points coincide with each other to minimize the normal skin effect. The sample was then taken into the superconducting mixed state from above H_{c2} and/or from below H_{c1} and the 100 to 400 times accululated wave forms were stored to be used as $d\phi/dt$ of Eq. 4.5. From the normal wave form and the superconducting wave form, x/R and B(x) were calculated and plotted. The q(t) was obtained by numerically integrating $d\phi_n/dt$ and all data were stored on magnetic tapes for later use. $\mu_{eq}(B)$ was obtained from the dc magnetization measurements made by C. Chen (Fig. 4.4) and calculated by Anjaneyulu (Fig. 4.5). The magnetization system has been described by Fearday in his Ph. D. thesis (1971).

Figure 4.2 (a) F_V vs. distance from the sample surface.

(b) The corresponding magnetic field profile at various times during the ac cycle (Rollins et. al. 1974)

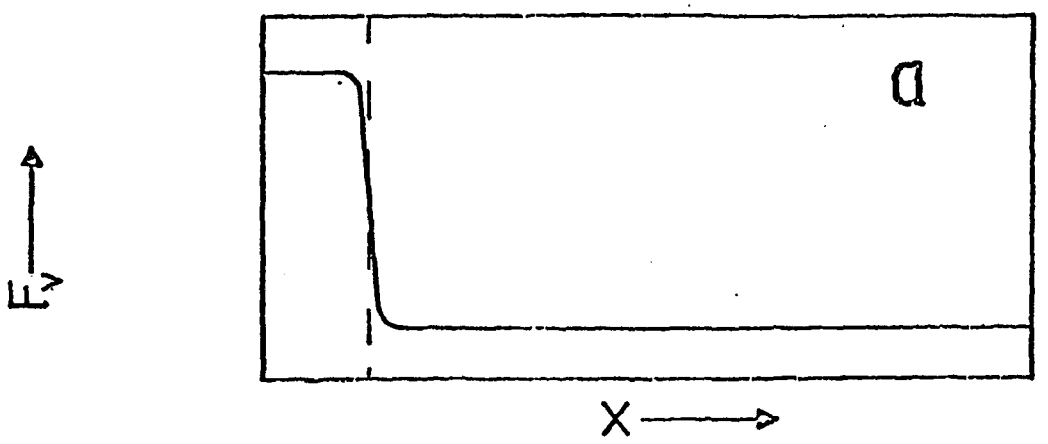
a
E
X

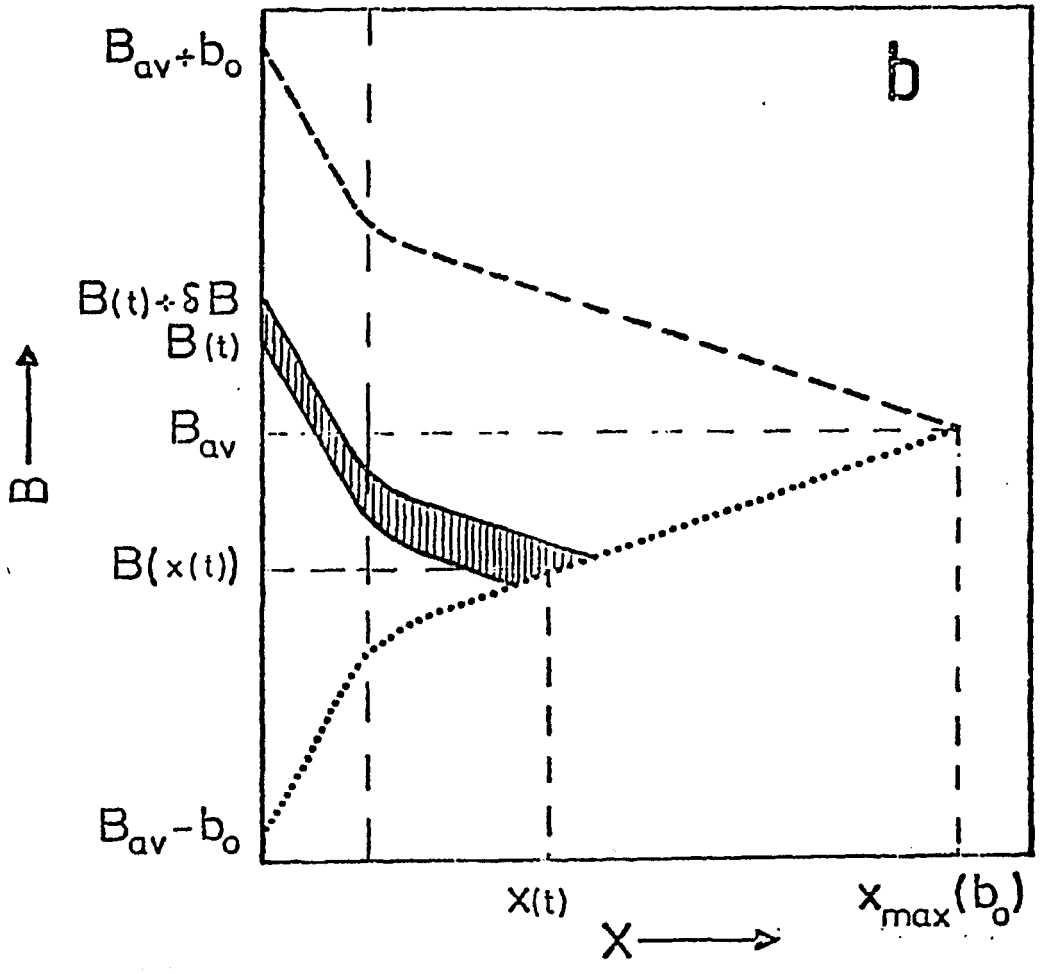
b
$B_{av}+b_o$
$B(t)+\delta B$
$B(t)$
B_{av}
$B(x(t))$
$B_{av}-b_o$
B
$x(t)$
$x_{max}(b_o)$
X

Figure 4.3 Block diagram of the electronic circuitry used for the field profile measurement.

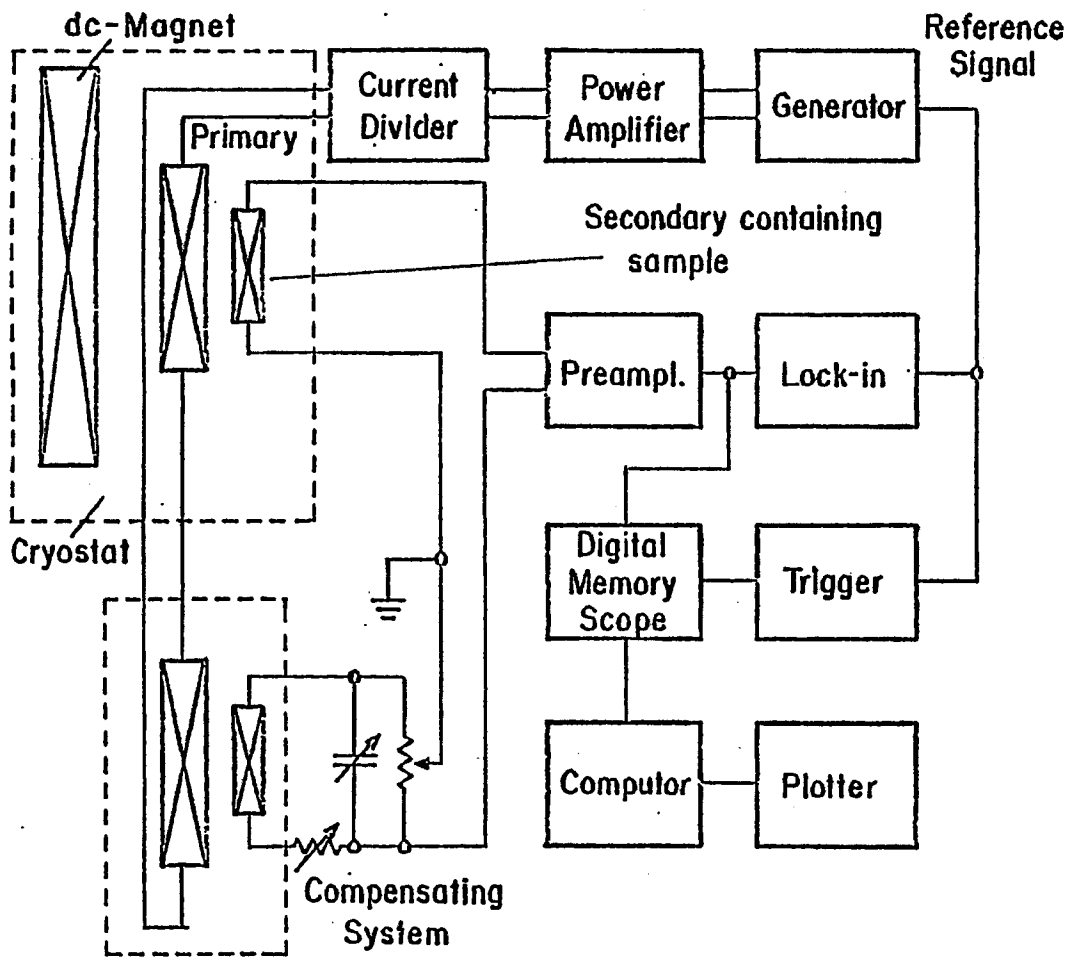
dc-Magnet
Current Divider
Power Amplifier
Generator
Reference Signal
Primary
Secondary containing sample
Preampl.
Lock-in
Cryostat
Digital Memory Scope
Trigger
Computor
Plotter
Compensating System

Figure 4.4 Magnetization curve of an annealed Nb sample obtained at 4.2°K (Anjaneyulu 1977).

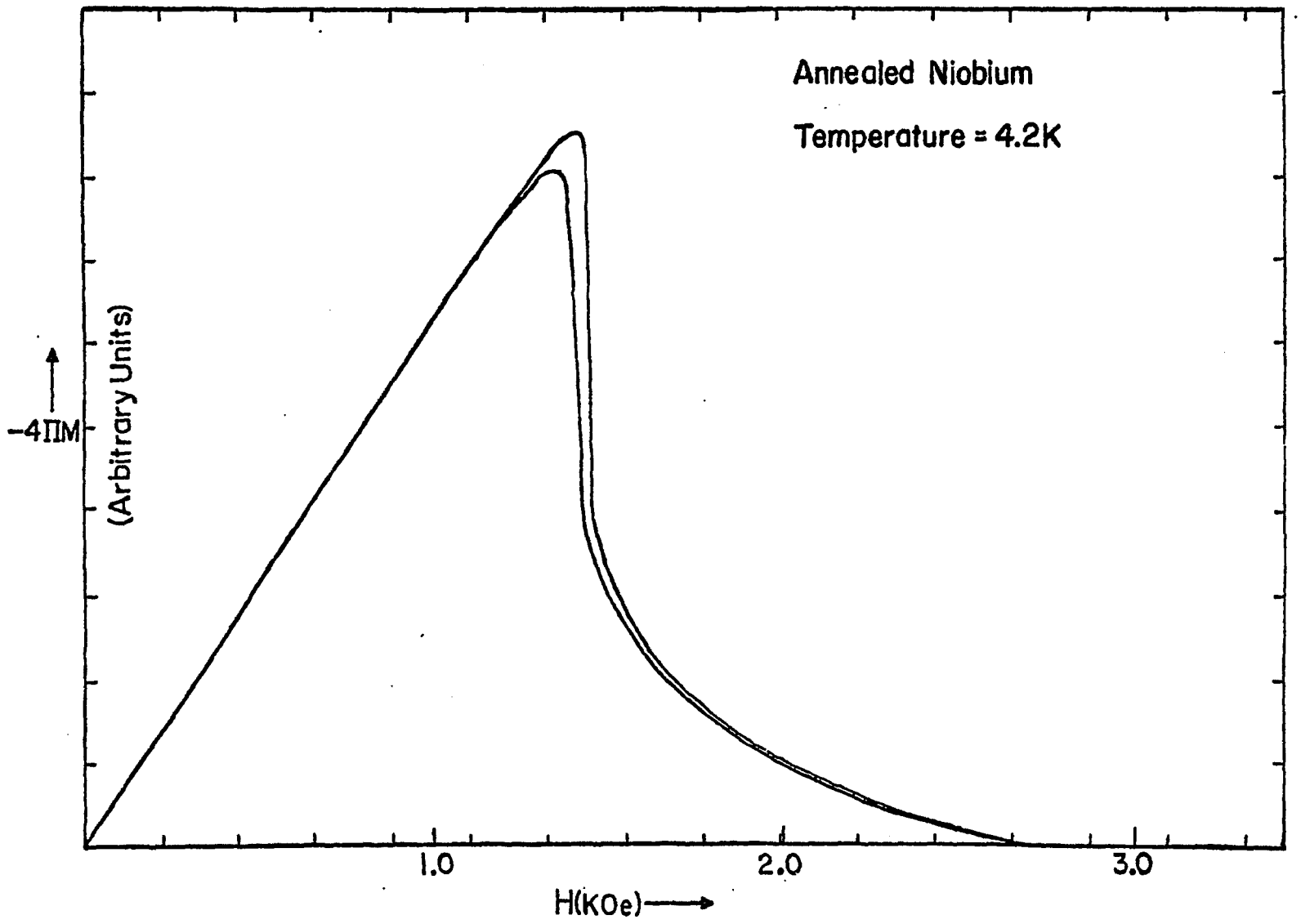
Annealed Niobium
Temperature = 4.2K
−4ΠM
(Arbitrary Units)
1.0
2.0
3.0
H(KOe)

Figure 4.5 $\mu_{eff}(B)$ obtained from magnetization measurements for three different temperatures plotted as a function of reduced field H/H_{c2} (Anjaneyulu 1977).

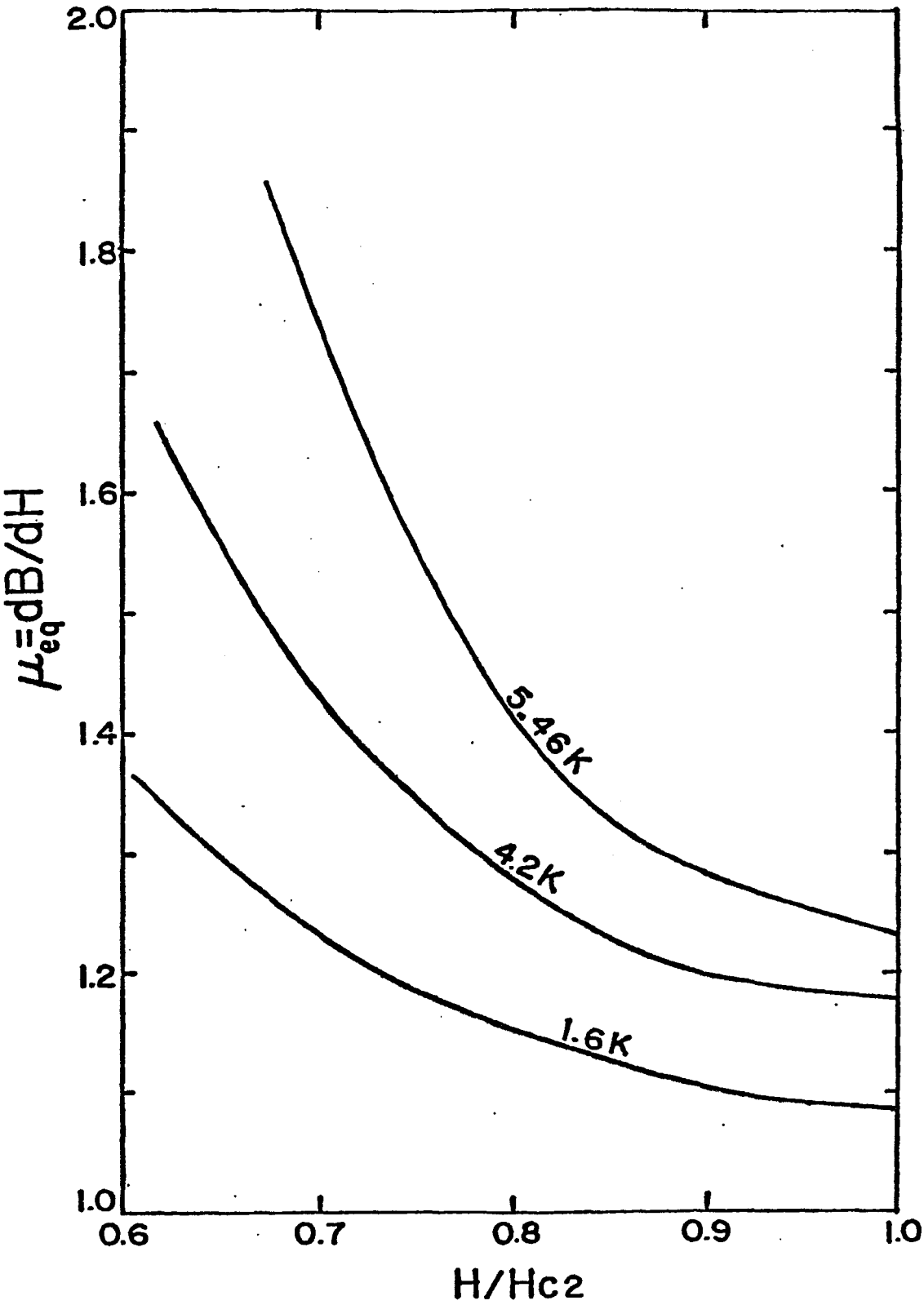
2.0
1.8
1.6
1.4
1.2
1.0
μ_{eq}=dB/dH
0.6
0.7
0.8
0.9
1.0
H/Hc2
5.46K
4.2K
1.6K

4.5 Intermediate Temperature Heat Treatment.

One of the samples (#20) was annealed at several successively higher temperatures of 135°C, 364°C, 455°C and 579°C for approximately one hour each in vacuum of abount 10^{-6} torr. The field profiles were measured after each annealing.

The copper base of the sample was etched away chemically in a solution of sulfuric acid and nitric acid. The sample was suspended at both ends by a stainless steel wire and placed in a glass tube. The tube was pumped with a liquid-nitrogen-trapped oil diffusion-pump vacuum system for more than 12 hours. With the pressure at about 10^{-6} torr the glass tube containg the sample was inserted in a preheated oven. The temperature was measured with a thermocouple inserted in the center hole of the sample and it took about 20 minutes for the sample to reach the annealing temperature and to cool down to room temperature again once removed fron the oven.

Chapter V

EXPERIMENTAL RESULTS

5.1 Histories of Samples.

The samples #16 to #22 came from two different niobium rods. A portion was cut from each rod before swaging and these pieces were annealed following the sample preperation procedure (Sec. 4.1). The resistivity ratios of these annealed pieces were measured to be 1180 and 1330. The niobium rods were swaged and made into samples. A sample annealed at $2045^{\circ} \pm 10^{\circ}$C had a trace of melting on its surface. Since the melting point of Nb is $2480^{\circ} \pm 10^{\circ}$ C, the actual annealing temperature should be considered about $380^{\circ} \pm 10^{\circ}$ C above the optical pyrometer reading. The difference came from the absorption of the glass wall of the vacuum chamber of the induction furnace and a correction due to the emmissivity of Nb. The sample #16 (table 5.1) and #18 (table 5.2) were irradiated in three successive steps and the other samples (table 5.3) were irradiated once with 3.2 Mev protons. The resistivity ratios of the samples (except sample #20) were measured after the anneal part 2 and reannealed afterward. In case of sample #20, the resistivity ratio was measured after the heat treatment experiment (Sec. 5.5).

The samples #23, #26, #27, #29 and #12, #13 were irradiated with 1.0 Mev protons. These samples, except #12 and #13 (table 5.4), were believed to have resistivity ratios similar to those of the previous samples. The samples #12 and #13 (table 5.5) came from the first niobium rod which was not etched before swaging but just cleaned in acetone. In this case, surface contamination might not have been removed or perhaps this rod was contaminated as purchased. In any case, the resistivity ratios of the samples from this rod never reached more than about one hundred. These two samples were included for comparison with the other samples.

The field profiles of some samples were measured before the proton bombardment and showed no detectable flux pinning force. The initial volume pinning force may vary from sample to sample but it is very small and it is assumed that the pinning force after the proton bombardment comes entirely from the defects produced by the incident protons.

Table 5.1 History of the sample #16.

The empty space represents the steps skipped and the temperatures are the optical pyromerter readings with an uncertainty of $\pm 10^{\circ}C$ (add 380° $\pm 10^{\circ}C$ to find the actual annealing temperature).

sample no.		16		
anneal part 1	temp. (°C)			
	time (hours)			
anneal part 2	temp. (°C)	2030		
	time (hours)	25		
	vacuum (10^{-7} torr)	3.7		
resistivity ratio				
anneal part 3	temp. (°C)			
	time (hours)			
	vacuum (10^{-7} torr)			
proton dosage	energy (Mev)	3.2	3.2	3.2
	no. of sweeps	6	3	3
	duration (min.)	157	77	78
	meter (10^{-3} coul)	31.2	16.8	20.2
	actual (10^{-3} coul)	26.2	14.1	17.0
	per cm^2 (10^{16} p)	4.07	2.23	2.65
	accum. (10^{16} p/cm^2)	4.07	6.30	8.95

Table 5.2 History of the sample #18.

The temperatures are the optical pyrometer readings with an uncertainty of $\pm 10^{\circ}$C (add 380° $\pm 10^{\circ}$C to find the actual annealing temperature).

sample no.		18		
anneal part 1	temp. ($^{\circ}$C)	1800		
	time (hours)	1.5		
anneal part 2	temp. ($^{\circ}$C)	2025		
	time (hours)	12.2		
	vacuum (10^{-7} torr)	2.2		
resistivity ratio		1890		
anneal part 3	temp. ($^{\circ}$C)	2025		
	time (hours)	7.42		
	vacuum (10^{-7} torr)	3.0		
proton dosage	energy (Mev)	3.2	3.2	3.2
	no. of sweeps	3	3	3
	duration (min.)	77	76	79
	meter (10^{-3} coul)	15.2	16.3	17.0
	actual (10^{-3} coul)	12.8	13.7	14.3
	per cm^2 (10^{16} p)	2.01	2.19	2.19
	accum. (10^{16} p/cm^2)	2.01	4.20	6.39

Table 5.3 Histories of the samples #17, #20, #21 and #22.

* The resistivity ratio of sample #20 was measured after the annealing experiments (Sec. 5.6).

\- The annealing temperature was not measured but should be similar to the others.

The empty space represents the steps skipped and the temperatures are the optical pyrometer readings with an uncertainty of $\pm 10^{\circ}C$ (add 380° $\pm 10^{\circ}C$ to find the actual annealing temperature).

sample no.		17	20	21	22
anneal part 1	temp. (°C)	1840	1900	1921	-
	time (hours)	1.2	2.3	4.0	5.3
anneal part 2	temp. (°C)	2030	2035	2035	-
	time (hours)	24	12	17.5	14
	vacuum (10^{-7} torr)	2.6	2.2	2.6	2.1
resistivity ratio		1440	1400*		
anneal part 3	temp. (°C)	2025			
	time (hours)	18.5			
	vacuum (10^{-7} torr)	2.6			
proton dosage	energy (Mev)	3.2	3.2	3.2	3.2
	no. of sweeps	6	12	2	3
	duration (min.)	166	319	56	78
	meter (10^{-3} coul)	35.8	68.0	20.7	17.3
	actual (10^{-3} coul)	30.1	59.2	17.4	14.5
	per cm^2 (10^{16} p)	4.53	8.92	2.58	2.32

Table 5.4 Histories of samples #23, #26, #27 and #29.

- The temperature was not measured but should be similar to the others.

The empty space represents the steps skipped and the temperatures are the optical pyrometer readings with an uncertainty of ±10 °C (add 380 ±10 °C to find the actual annealing temperature).

sample no.		23	26	27	29
anneal part 1	temp. ($^{\circ}$C)	1830	1860	-	1830
	time (hours)	2.7	6.0	3.2	3.3
anneal part 2	temp. ($^{\circ}$C)	2020	-	2025	2020
	time (hours)	20.5	12	11	22
	vacuum (10^{-7} torr)	3.0	2.0	2.2	1.7
resistivity ratio					
anneal part 3	temp. ($^{\circ}$C)				
	time (hours)				
	vacuum (10^{-7} torr)				
proton dosage	energy (Mev)	1.0	1.0	1.0	1.0
	no. of sweeps	2	4	2	3
	duration (min.)	60	118	57	95
	meter (10^{-3} coul)	18.2	18.2	16.2	17.3
	actual (10^{-3} coul)	15.3	15.3	13.6	14.5
	per cm^2 (10^{17} p)	2.06	2.11	1.94	1.86

Table 5.5 Histories of samples #12 and #13.

The temperatures are the optical pyrometer readings with an uncertainty of ±10 °C (add 380 ±10 °C to find the actual annealing temperature).

sample no.		12	13
anneal part 1	temp. (°C)	1880	1920
	time (hours)	3.0	3.5
anneal part 2	temp. (°C)	2020	2020
	time (hours)	22	20
	vacuum (10^{-7} torr)	1.4	1.2
resistivity ratio		91	102
anneal part 3	temp. (°C)	2020	2040
	time (hours)	10	14.5
	vacuum (10^{-7} torr)	2.2	2.0
proton dosage	energy (Mev)	1.0	1.0
	no. of sweeps	2	3
	duration (min.)	59	70
	meter (10^{-3} coul)	17.4	16.3
	actual (10^{-3} coul)	14.6	13.7
	per cm^2 (10^{16} p)	2.00	2.50

5.2 Field Profiles.

The wave forms obtained at dc fields above H_{c3} are purely sinusoidal. However, as soon as the dc field was lowered below H_{c2}, the wave forms of the proton irradiated samples showed a drastic reduction in amplitude and a change in shape (Fig. 5.1). Since the damage produced by the protons was confined to the region close to the surface (within the depth of 50 microns in the case of 3.2 Mev protons), the magnetic field experienced no pinning force beyond this surface region. The wave forms were very small when the ac field was not large enough to penetrate beyond this surface pinning region but as soon as the ac field exceeded this barrier, the wave form suddenly became large. The zero crossing points of the wave forms did not exactly coincide. The large amplitude wave forms which represent the deep penetration of the ac magnetic field into the sample tend to have phase lags. This was believed to be the effect of the flux flow and the data points close to the zero crossing points were excluded.

The field profiles obtained from these wave forms shows the actual position dependence of the magnetic field inside the samples (Fig. 5.2). Several different ac field amplitudes were used for a complete field profile to improve the quality of the graphs and they agreed well in most cases (Fig. 5.3). The profiles of the decreasing portions of the

ac fields (dots in Fig. 5.2 and Fig. 5.3) and the increasing portions agreed very well except when the amplitude of the ac field was too large. Some of the samples displayed a cycling effect and time dependent behavior at dc fields much lower than H_{c2}. These effects will be discussed in section 5.6.

Figure 5.1 The wave forms at different dc fields.

Sample #18 after the 3rd irradiation. The ac field amplitude is 6 Oe.

—— H_{dc}= 7.5 KOe (in the normal state).

--- H_{dc}= 2.69 KOe.

— — H_{dc}= 2.60 KOe.

—·— H_{dc}= 2.48 KOe.

The superconducting state wave forms are enlarged ten times.

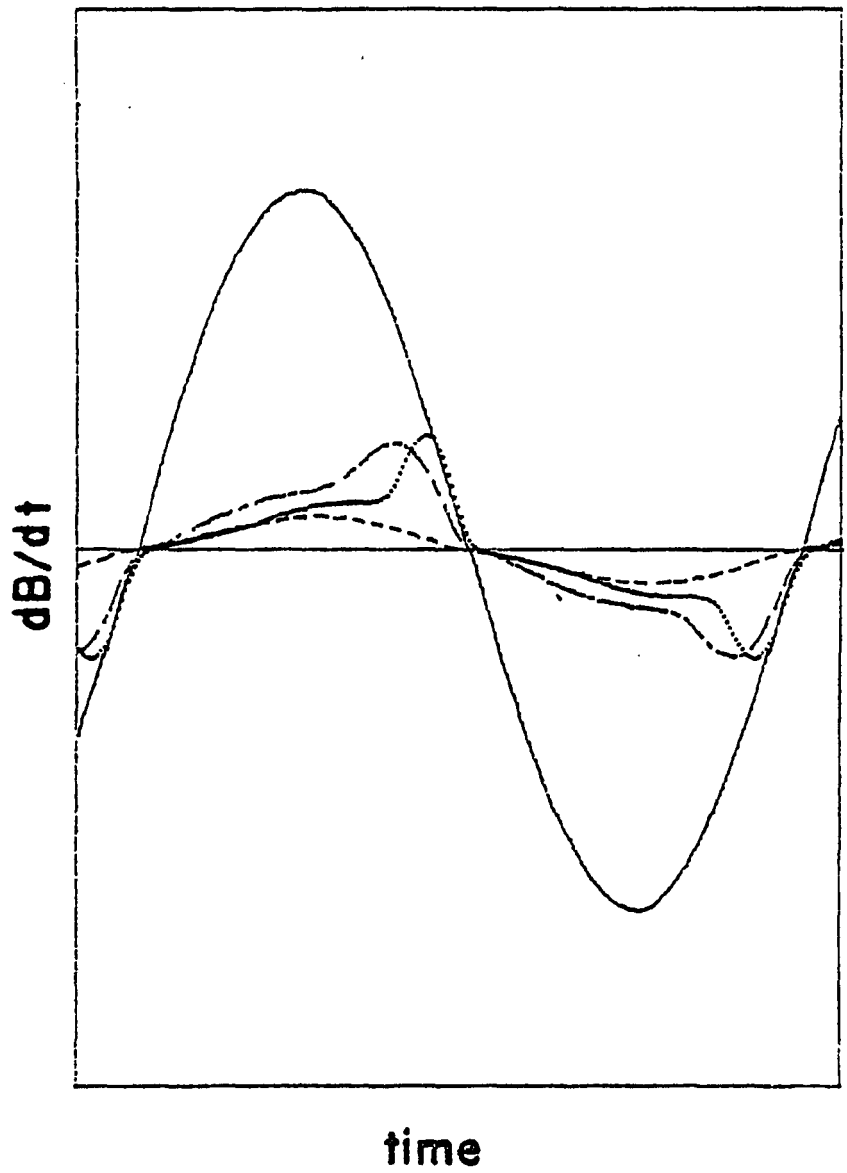
dB/dt
time

Figure 5.2 The field profiles at different dc fields. Sample #18 after the 3rd irradiation. The ac field amplitude is 6 Oe (wave forms of Fig. 5.1).

Δ H_{dc}= 2.69 KOe

X H_{dc}= 2.60 KOe

Z H_{dc}= 2.48 KOe

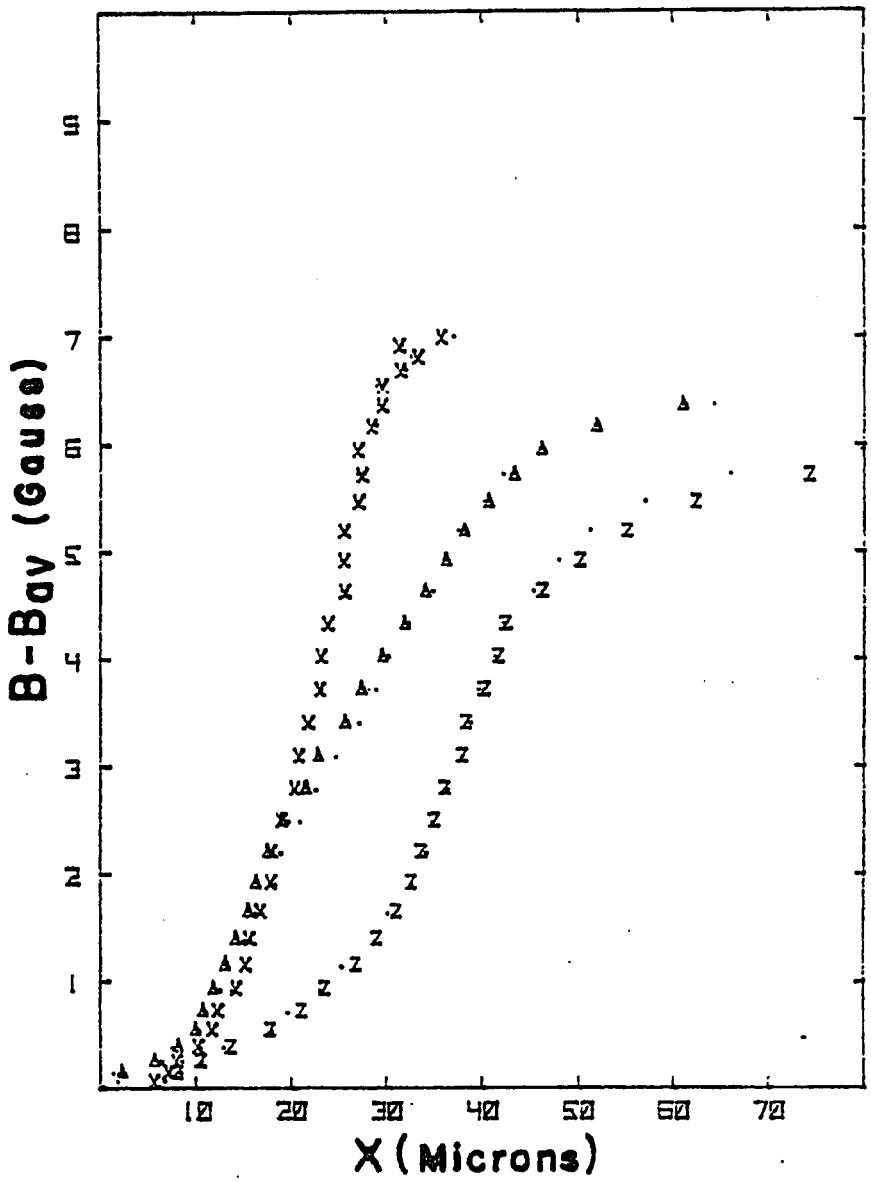
B-Bav (Gauss)
X (Microns)
1
2
3
4
5
6
7
8
9
10
20
30
40
50
60
70

Figure 5.3 Field profiles with different ac field amplitudes.

Sample #18 after 3rd irradiation at H_{dc} = 2.6 KOe.

X with 2.5 Oe ac field.

Δ with 6.0 Oe ac field.

Z with 10 Oe ac field.

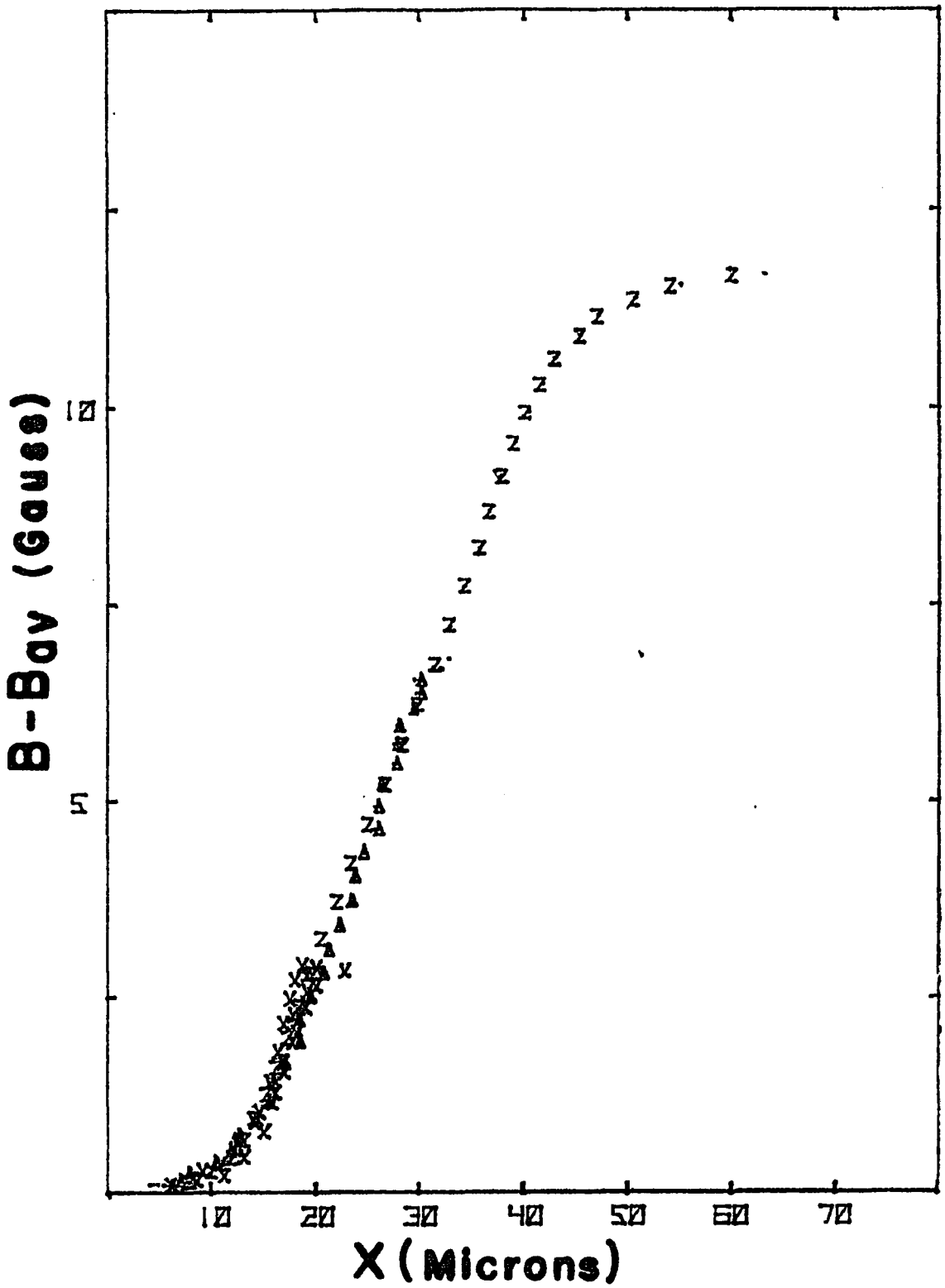
B-Bav (Gauss)
10
5
10
20
30
40
50
60
70
X (Microns)

5.3 Measurements of Total Pinned Magnetic Field and Volume Pinning Force.

Unfortunately, the phase shifts of the normal wave forms due to the normal skin effect and of the superconducting state wave forms due to the flux flow effect were not always easy to determine unambiguously. The slope of the field profile needed in the calculation of the volume pinning force depends not only on the above mentioned phase shift but also critically on the depth from the sample surface, and these effects made it rather difficult to determine accurately the volume pinning force as a function of depth. However, the total amount of magnetic field pinned by the surface pinning region, B_t, was found to be quite insensitive to the above factors. Therefore, we have chosen to use the total pinned magnetic field, B_t, when comparing the pinning behavior of different samples. The alignment of the samples during irradiation is such that the proton beam strikes normal to the sample surface. Small deviations in this alignment will cause deviations in the damage profile and would lead to large errors when comparing the volume pinning force measured at a particular depth in different samples.

The total pinned magnetic field, B_t, is related to the total integrated volume pinning force using Eq. 2.8.

$$B_t = \int_0^{x_{max}} \frac{dB}{dx} dx \simeq \frac{\mu_{eq}}{B_{av}} \int_0^{x_{max}} F_v \, dx \quad , \tag{5.1}$$

where we have assumed $B_t \ll B_{av} \equiv B_{eq}(H_{dc})$, and x_{max} is the maximum depth to which radiation damage, and hence, flux pinning occurs. For 3.2 Mev protons, $x_{max} \sim 50$ micron.

The results of the three successive irradiations of sample #18 and sample #16 are shown in figures 5.4 and 5.5. These two samples displayed sharp peaks close to H_{c2}. The integrated volume pinning force at fields above the peak seems to be little affected by the different proton fluence. However, B_t is observed to increase rapidly at lower dc fields as the fluence increases. Thus, increasing the irradiation is found to decrease the dc field where the peak occurs as well as reduce the sharpness of the peak. The graph of sample #22 is similar to that of sample #16 after the second irradiation but the other samples displayed much higher integrated pinning forces with no noticeable peak effect (Fig. 5.6).

The samples irradiated with 1.0 Mev protons did not show any conclusive trend except that samples #12 and #13 displayed very large pinning forces. In fact, an ac field of 200 Oe or higher could penetrate a measureable depth only when the dc field was just below H_{c2} and the increasing portions and the decreasing portions of the field profiles

were entirely different from each other. Hence, no quantitative information could be obtained from these samples (Fig. 5.7).

The volume pinning forces are calculated from the slopes of the field profiles with an uncertainty of up to 50 % or more in some cases. The samples irradiated with 1.0 Mev and some with 3.2 Mev showed a minor depth distribution but most irradiated with 3.2 Mev showed that the volume pinning force is a critical function of the depth. For those samples which showed a significant depth dependence, the volume pinning force was calulated at two different depths. The volume pinning force at the shallower depth was always smaller than the one at the deeper depth and had a sharp peak at a higher dc field (Fig. 5.8 and 5.9).

Figure 5.4 The total pinned magnetic field vs. the dc field (H_{c2}: 2.715 ± 0.005 KOe).

Sample #18 (proton energy: 3.2 Mev).

X total fluence 2.01×10^{16} p/cm^2 (after 1st irradiation).

Δ total fluence 4.20×10^{16} p/cm^2 (after 2nd irradiation).

□ total fluence 6.39×10^{16} p/cm^2 (after 3rd irradiation).

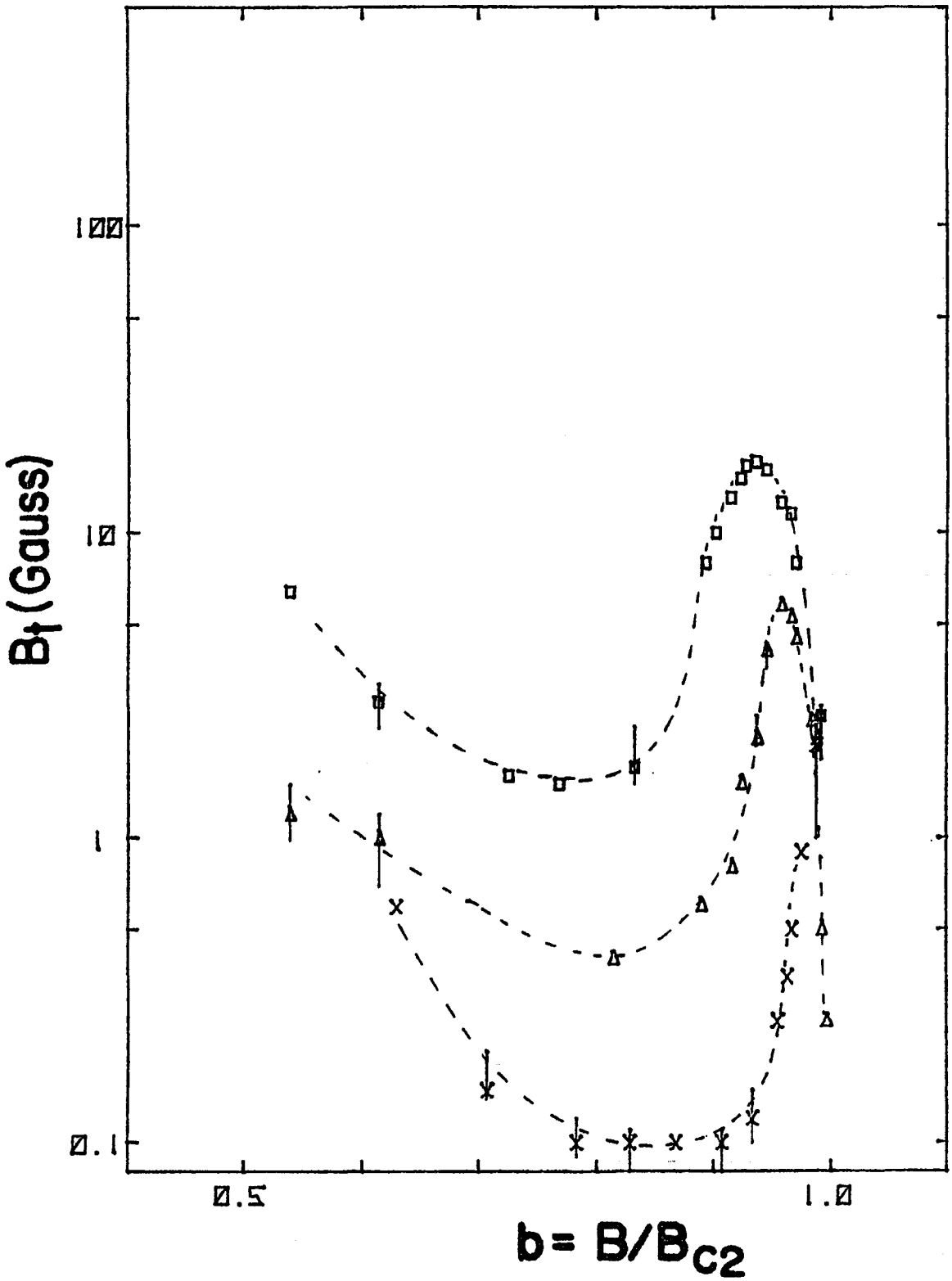
100
10
1
0.1
0.5
1.0
B_t (Gauss)
$b = B/B_{c2}$

Figure 5.5 The total pinned magnetic field vs. the dc field (H_{c2}: 2.715 ± 0.005 KOe).

Sample #16 (proton energy: 3.2 Mev).

× total fluence 4.07×10^{16} p/cm^2 (after 1st irradiation).

△ total fluence 6.30×10^{16} p/cm^2 (after 2nd irradiation).

□ total fluence 8.95×10^{16} p/cm^2 (after 3rd irradiation).

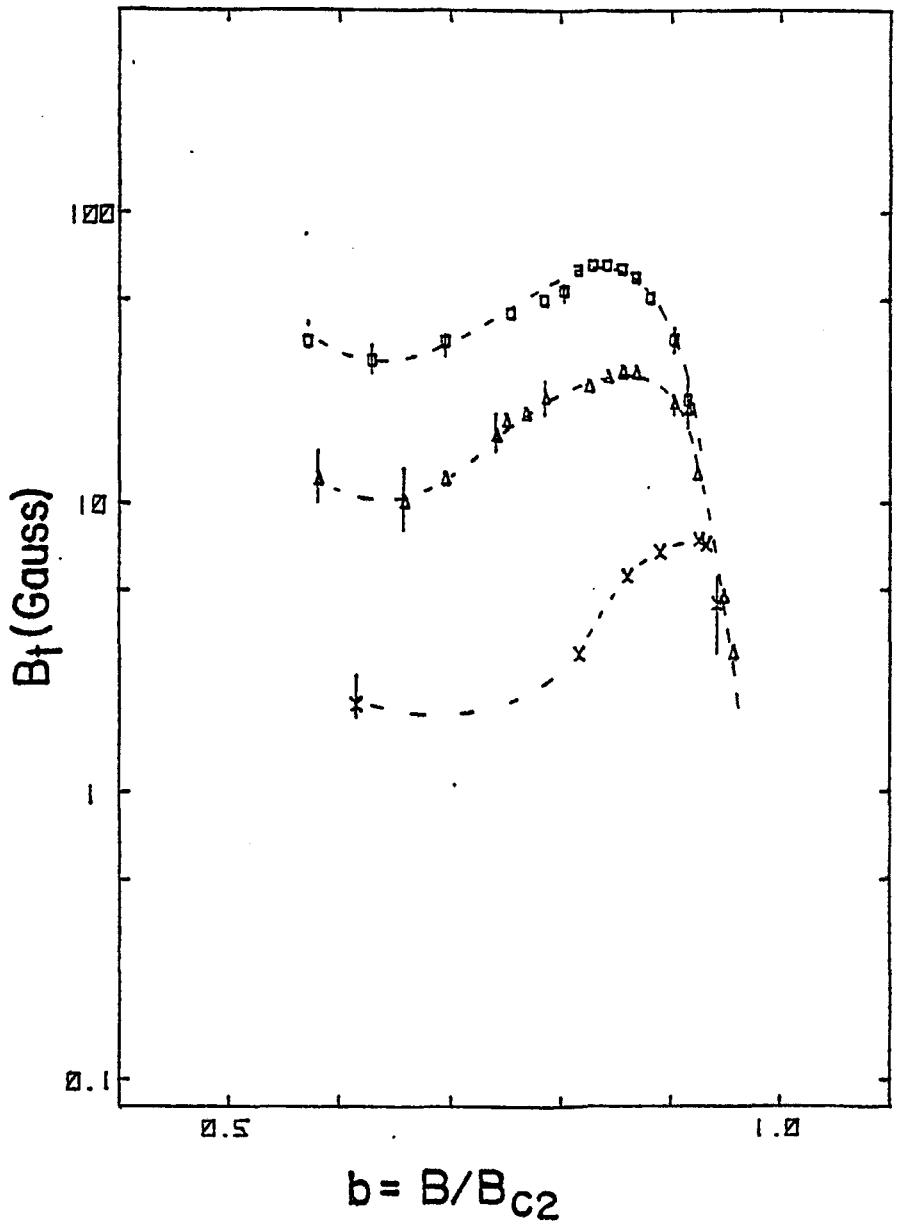
100
10
1
0.1
0.5
1.0
B_t (Gauss)
$b = B/B_{c2}$

Figure 5.6 The total pinned magnetic field vs. the dc field (H_{c2}: 2.715 ± 0.005 KOe).

▽ sample #17 (total fluence 4.53×10^{16} p/cm^2).

□ sample #20 (total fluence 8.92×10^{16} p/cm^2).

× sample #21 (total fluence 2.58×10^{16} p/cm^2).

△ sample #22 (total fluence 2.32×10^{16} p/cm^2).

Proton energy: 3.2 Mev.

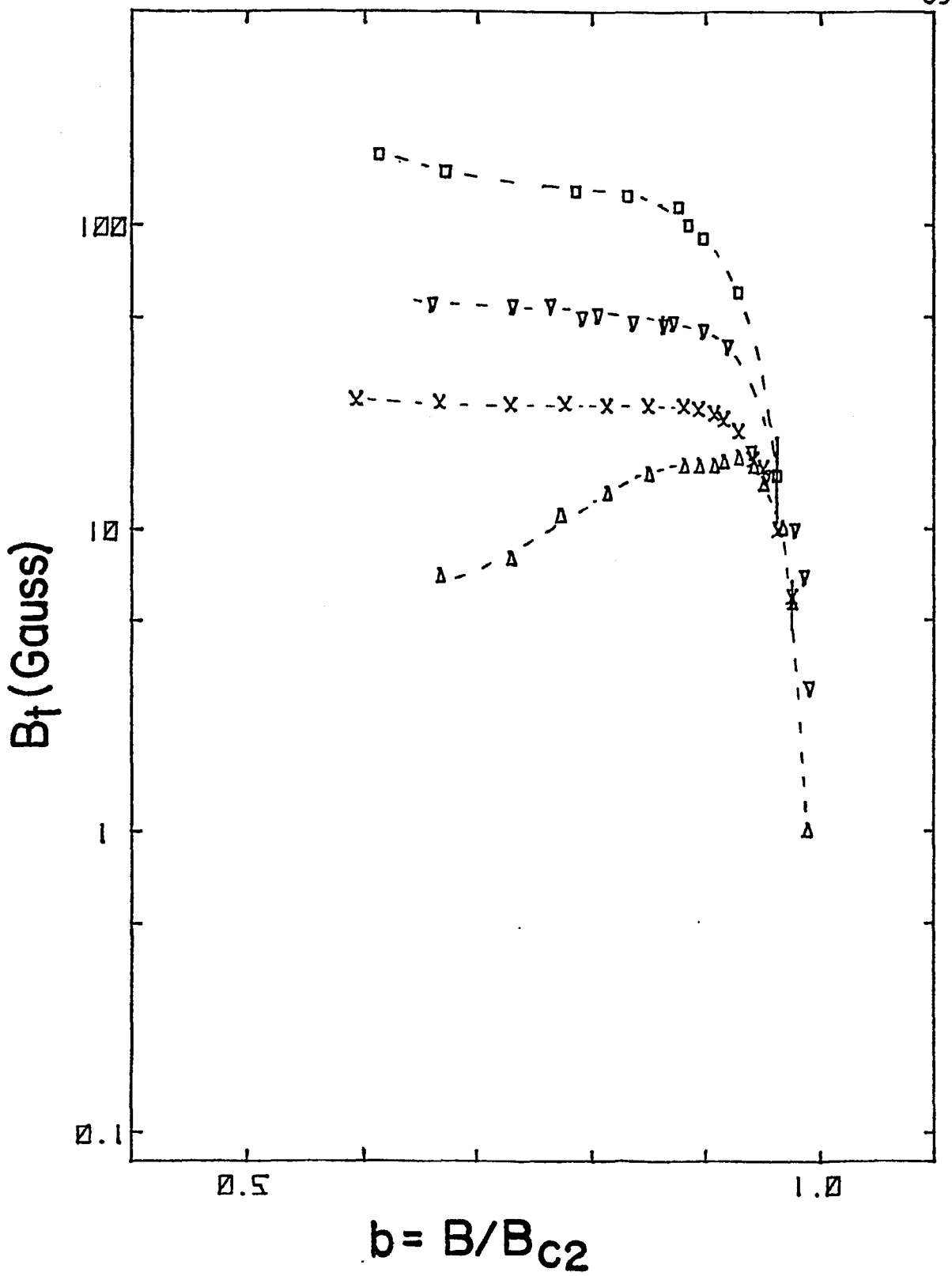
0.1
1
10
100
0.5
1.0
B_t (Gauss)
$b = B/B_{c2}$

Figure 5.7 The total pinned magnetic field vs. the dc field (H_{c2}: 2.715 ± 0.005 KOe).

× sample #23 (total fluence 2.06×10^{16} p/cm^2).

△ sample #26 (total fluence 2.11×10^{16} p/cm^2).

▽ sample #27 (total fluence 1.94×10^{16} p/cm^2).

□ sample #29 (total fluence 1.86×10^{16} p/cm^2).

Proton energy: 1.0 Mev.

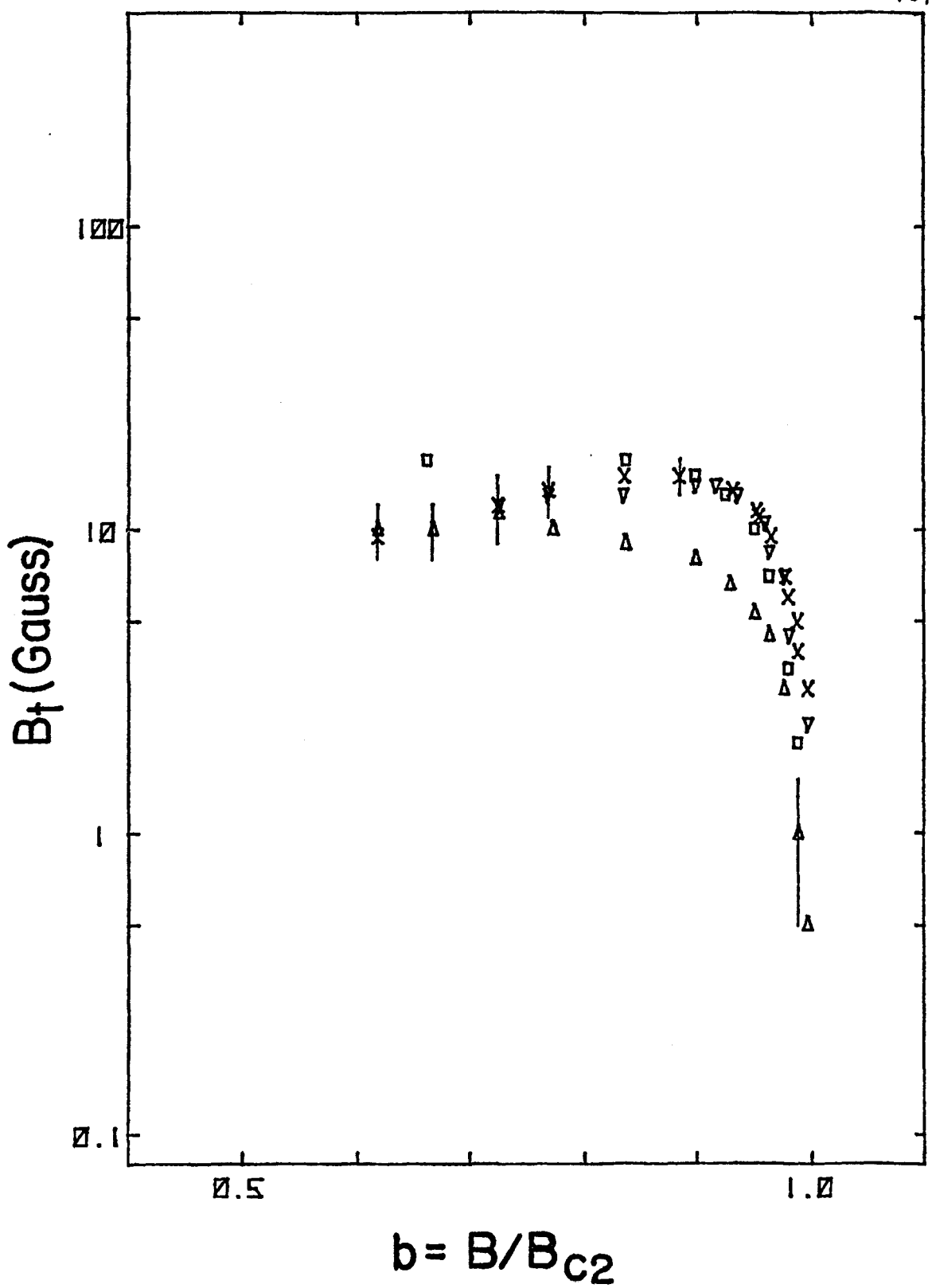
100
10
1
0.1
0.5
1.0
B_t (Gauss)
$b = B/B_{c2}$

Figure 5.8 The volume pinning force vs. the dc field.

sample #17

X at the depth of 15 ± 2.5 micron.

□ at the depth of 30 ± 5 micron.

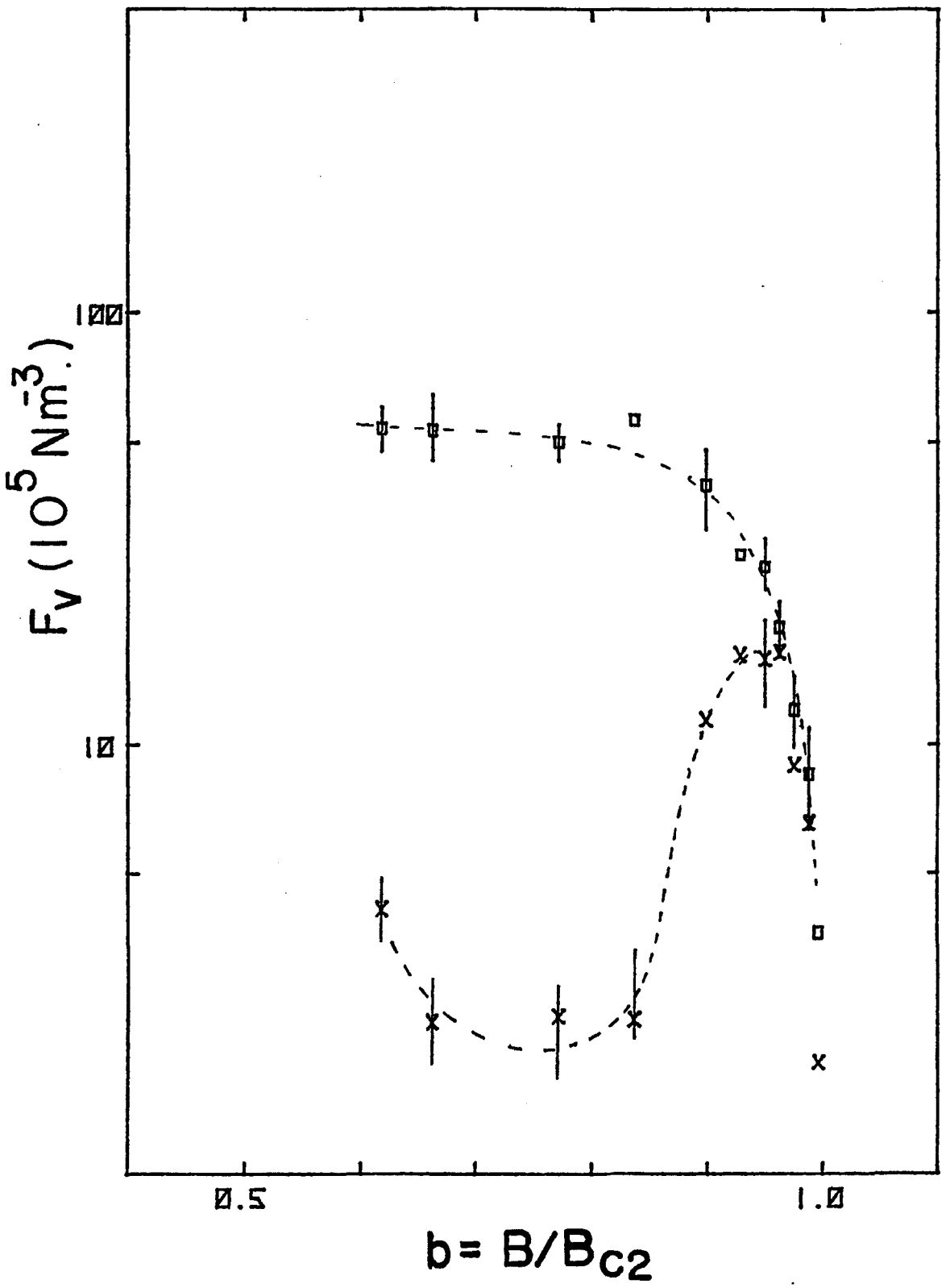
100
10
F_v (10^5 Nm^{-3}.)
0.5
1.0
b= B/B_{c2}

Figure 5.9 The volume pinning force vs. the dc field.

sample #22

X at the depth of 15 ± 2.5 micron.

□ at the depth of 30 ± 5 micron.

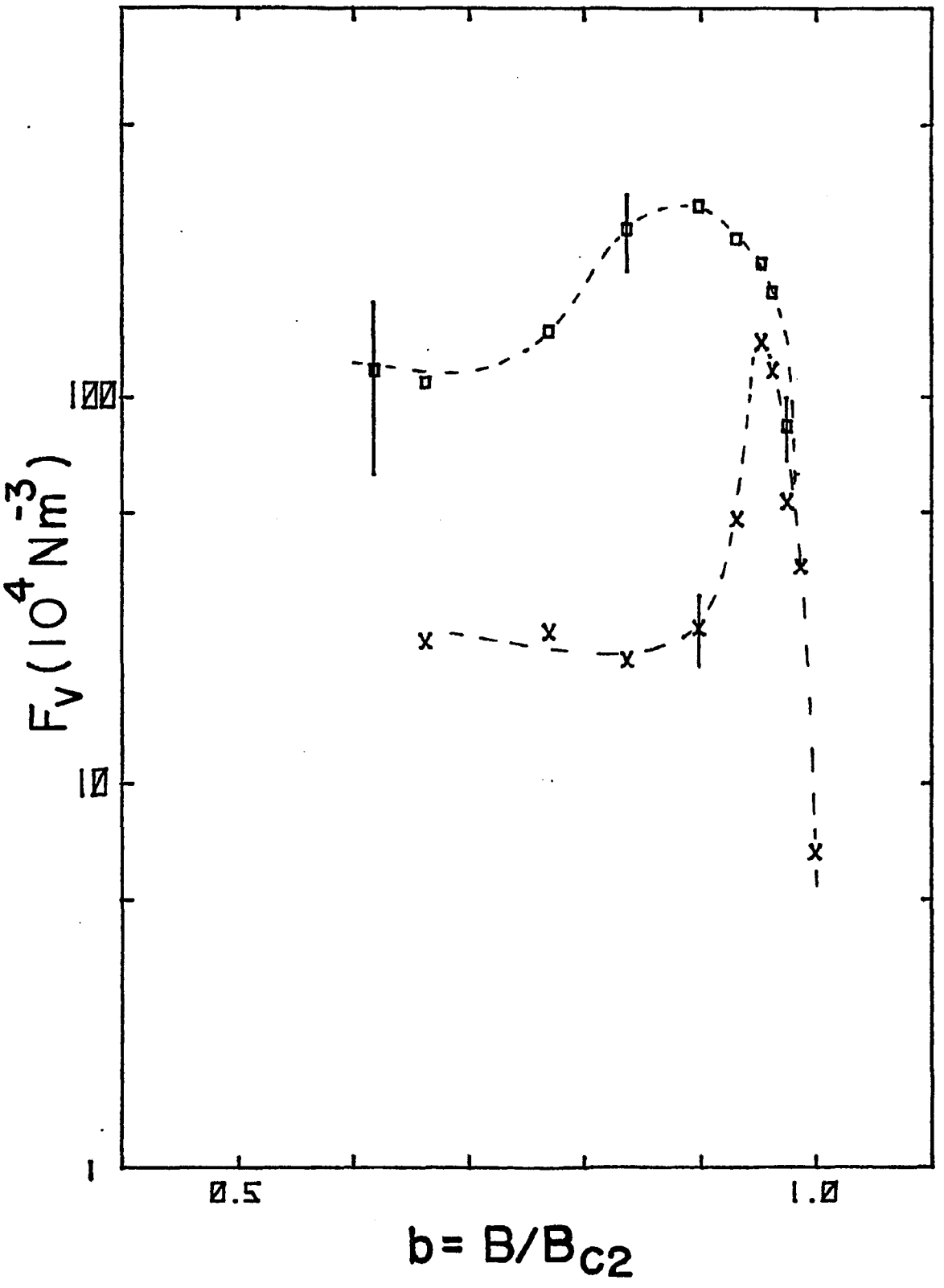
100
10
1
0.5
1.0
$F_v (10^4 Nm^{-3})$
$b = B/B_{c2}$

5.4 Proton Fluence Dependence of Total Pinned Magnetic Field.

An incident proton produces interstitial-vacancy pairs in the material, which, at room temperature, migrate to form interstitial type and vacancy type dislocation loops (Sec. 5.5). Presumally, the impurities in the material act as the nucleation cites for the dislocation loops and the density of the dislocation loops is not expected to change much as the fluence of protons increases. If the recombination of the interstitial-vacancy pairs is not extensive, the number of defects produced by the irradiation is roughly proportional to the proton fluence, Φ_p, and so is the total area of dislocation loops.

$$\Phi_p \propto \int_0^{x_{max}} \int_0^{D_{max}} \rho(x,D)\, D^2\, dD\, dx, \tag{5.2}$$

where x_{max} is the maximum penetration depth of the proton into samples and $\rho(x,D)$ is the density of the dislocation loops of diameter D at the depth x from the sample surface. Since the elementary pinning force f_p is proportional to the square of the dislocation loop diameter D (Kramer 1975), the fluence dependence of the total magnetic field pinned by all these dislocation loops, B_t, can be derived in cases of the

direct summation model and the FLL instability model under the assumption that the dislocation loops produced by the irradiation are the only pinning centers.

1) Direct summation model.

From Eq. 2.7 and Eq. 3.2,

$$\frac{dB}{dx} \propto \int_0^{D_{max}} \rho(x,D)\ f_p(D)\ dD$$

$$\propto \int_0^{D_{max}} \rho(x,D)\ D^2\ dD,$$

and

$$B_t = \int_0^{x_{max}} \frac{dB}{dx}\ dx \propto \Phi_p. \tag{5.3}$$

2) Quadratic summation model.

If the normalized size distribution of the dislocation loops to their average size s_{av} is independent from ϕ_p, then Eq. 5.2 becomes

$$\phi_p \propto s_{av} \int_0^{x_{max}} \int_0^{s'_{max}} \rho(x,s')\ s'\ ds'\ dx \propto s_{av} \tag{5.4}$$

where $s' = s/s_{av}$ and using Eq. 2.7 and Eq. 3.6,

$$\frac{dB}{dx} \propto \int_0^{s_{max}} \rho(x,s)\, s^2\, ds$$

$$\propto s_{av}^2 \int_0^{s'_{max}} \rho(x,s')\, s'^2\, ds' \propto s_{av}^2$$

and

$$B_t = \int_0^{x_{max}} \frac{dB}{dx}\, dx \propto \phi_p^2 \tag{5.5}$$

The actual graphs of the total pinned magnetic field, B_t, vs. the proton fluence ϕ_p at the different dc fields (Fig. 5.10 to Fig. 5.13) show the following results. The most significant data are those obtained from a given sample which was irradiated several times and measured after each irradiation. The dashed lines are drawn through these data in Fig. 5.10 to Fig. 5.13. For the dc field very close to H_{c2}, B_t was observed to be much less dependent on the proton fluence than at lower dc field. Also, when H_{dc} is near H_{c2}, the measured values of B_t were nearly the same for samples which experienced quite different total fluences. However, B_t was observed to depend more strongly on fluence as the dc field decreased below the peak. In some cases

$B_t \propto \Phi_p^n$ were $n \sim 3$ and in nearly all cases $n > 1$. We observed no evidence for a saturation effect for fluences up to 8×10^{16} protons/cm^2. We were unable to go to higher fluences since the small amplitude ac field approaximations essential for the measurement method is no longer valid at the larger amplitudes necessary to measure $B_t > 100$ Oe.

An explanation of the high fluence dependence at the low field could be the existence of some threshold. However, the threshold pinning force proposed by Labusch (1969) is much higher than the elementary pinning force of these dislocations (Anjaneyulu and Rollins 1979) and therefore totally inappropriate (Sec. 3.2). If there exists a lower threshold for some reason, it might explain this strong fluence dependence (Sec. 6.2).

Figure 5.10 Total pinned magnetic field vs. the proton fluence at 2.66 KOe dc field.

× sample #16

▽ sample #17

△ sample #18

□ sample #20

⊠ sample #21

✡ sample #22

Solid lines represent linear and quadratic slopes.

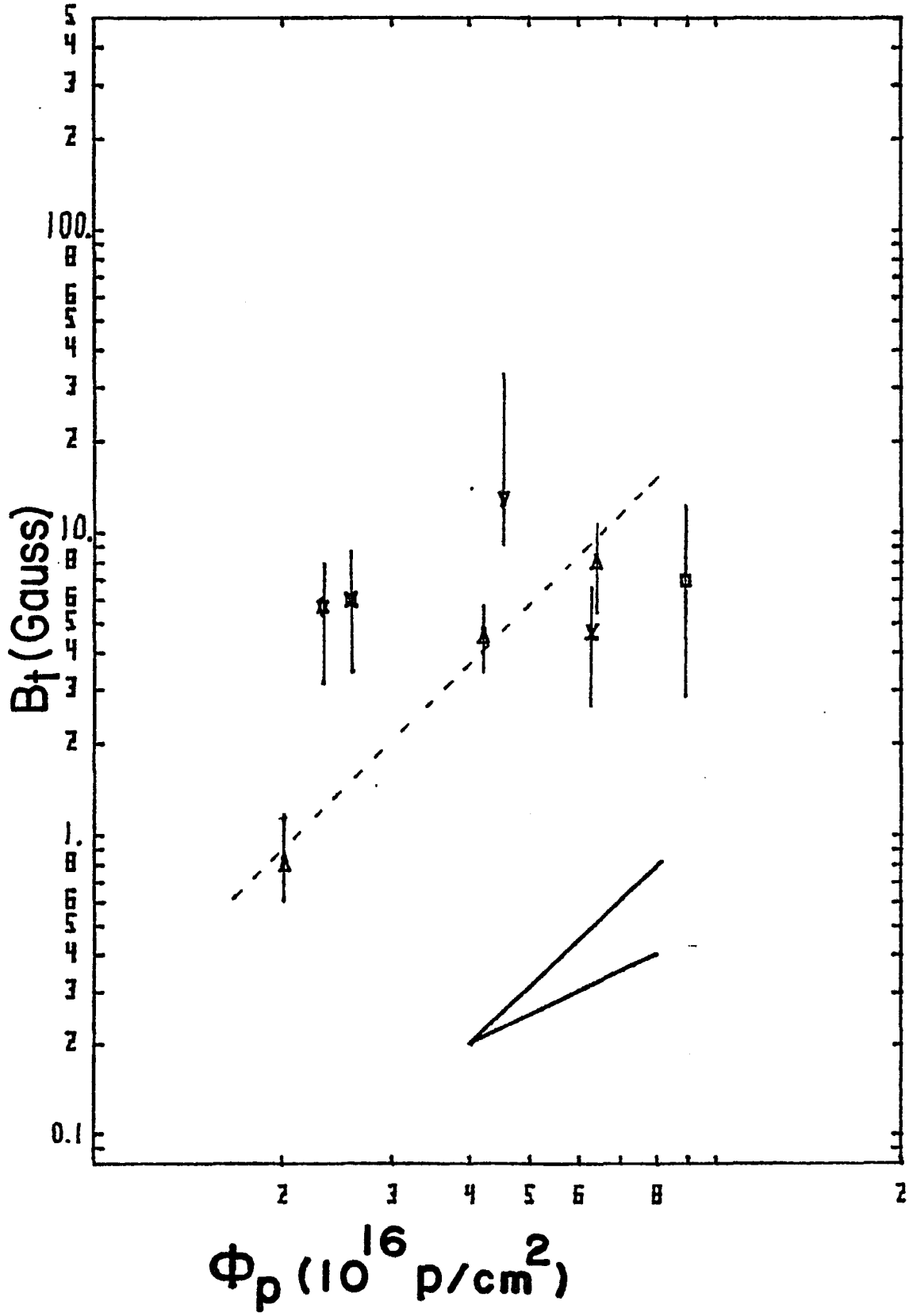
B_t (Gauss)
Φ_p (10^{16} p/cm^2)
100.
10.
1.
0.1

Figure 5.11 Total pinned magnetic field vs. the proton fluence at 2.60 KOe dc field.

× sample #16

▽ sample #17

△ sample #18

□ sample #20

⊠ sample #21

✡ sample #22

Solid lines represent linear and quadratic slopes.

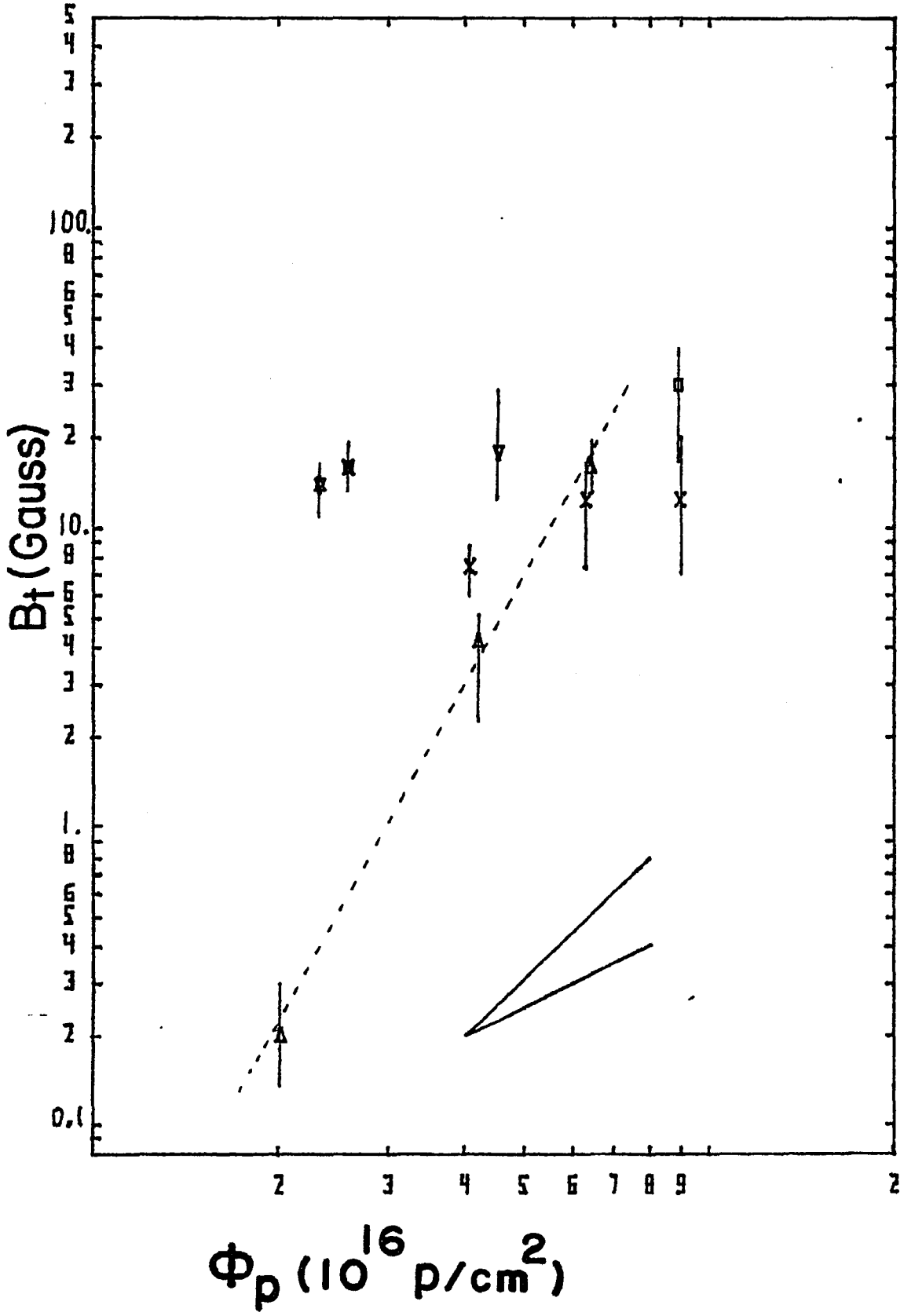
B_t (Gauss)
100.
10.
1.
0.1
2
3
4
5
6
7
8
9
Φ_p (10^{16} p/cm^2)

Figure 5.12 Total pinned magnetic field vs. the proton fluence at 2.48 KOe dc field.

X sample #16

▽ sample #17

△ sample #18

□ sample #20

⊠ sample #21

✡ sample #22

Solid lines represent linear and quadratic slopes.

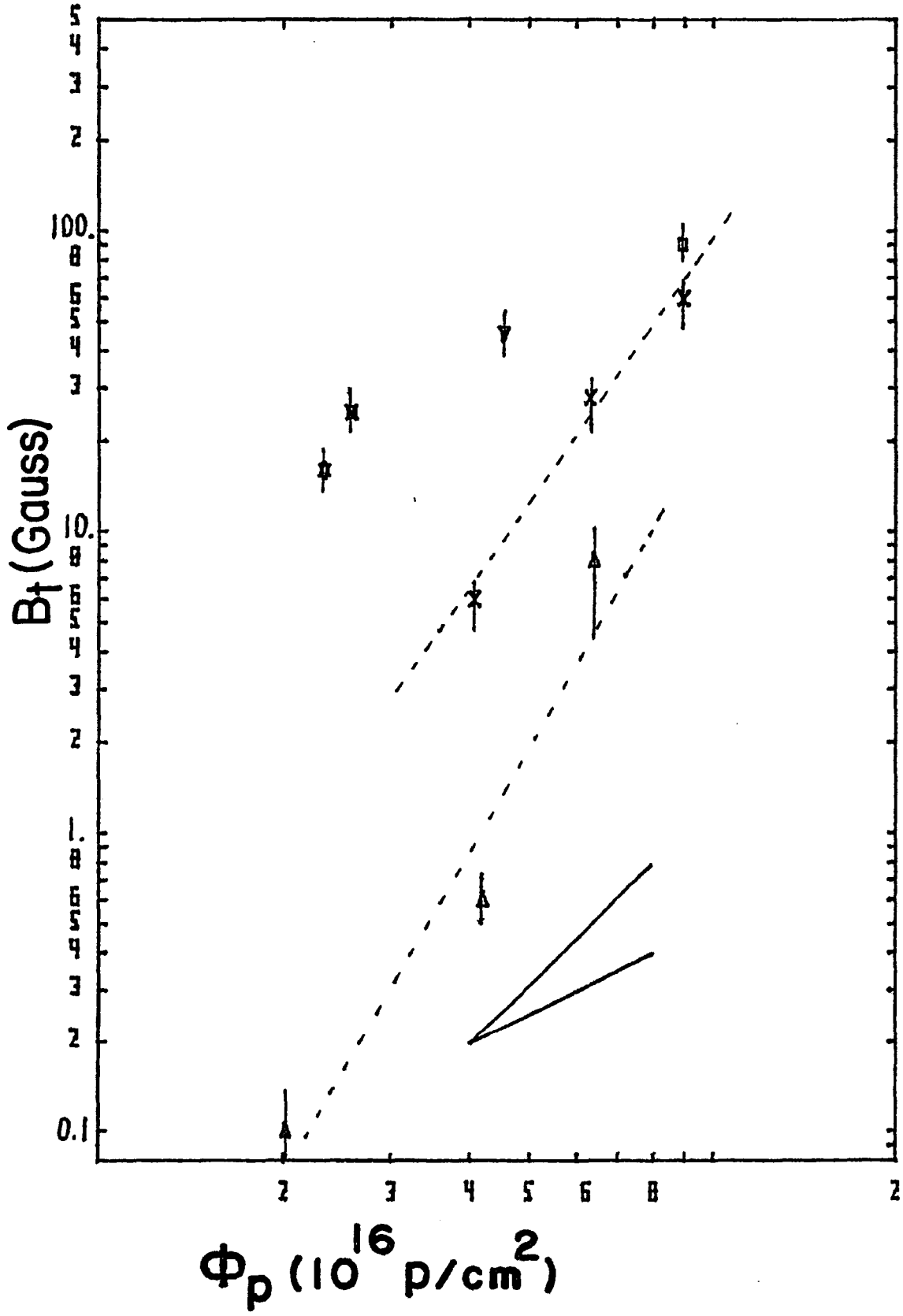
B_t (Gauss)
Φ_p (10^{16} p/cm^2)
100.
10.
1.
0.1

Figure 5.13 Total pinned magnetic field vs. the proton fluence at 2.30 KOe dc field.

× sample #16

▽ sample #17

△ sample #18

□ sample #20

⊠ sample #21

✡ sample #22

Solid lines represent linear and quadratic slopes.

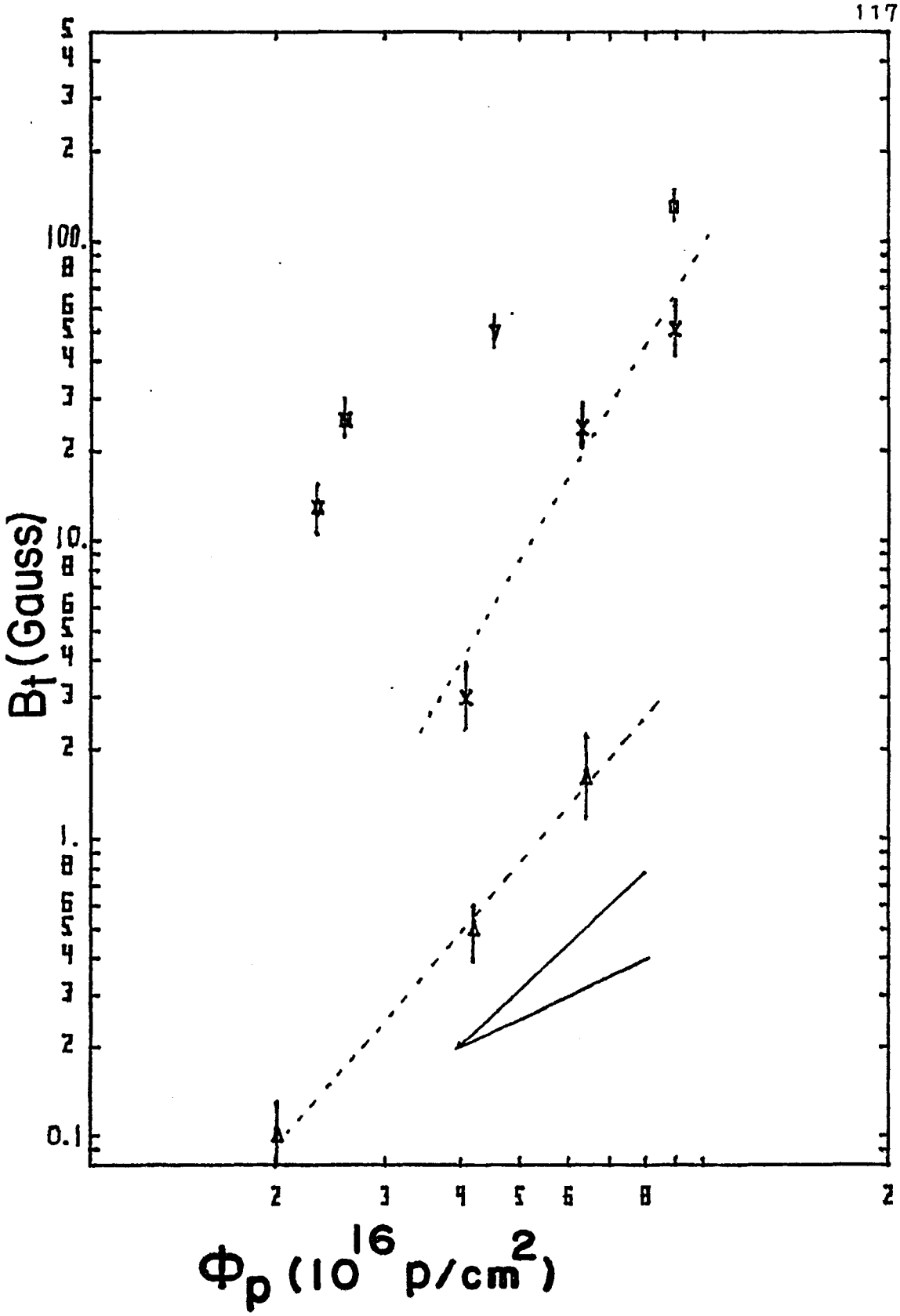
B_t (Gauss)
Φ_p (10^{16} p/cm^2)
100.
10.
1.
0.1

5.5 The Dependence of Total Pinned Magnetic Field on Subsequent Heat Treatment.

Sample #20 was annealed successively for approximately one hour each at temperatures of 135°C, 365°C, 415°C and 579°C. The results of B_t versus H_{dc} measured after each anneal is shown Fig. 5.14. The change in the pinning behavior by the annealing at 135°C was minimal but annealing at a temperature of 365° C and above produced markedly different volume pinning forces and their field dependence. The changes at dc fields close to H_{c2} were hardly noticeable while the volume pinning force was reduced drastically at dc fields much lower than H_{c2}. These results agree with the general assertion that samples with small volume pinning forces also exhibit a sharp peak effect (Sec. 5.3).

Chang and Chen (1977) reported the annealing behavior of dislocation loops in pure niobium (Fig. 5.21). They irradiated a thin sheet of moderately pure niobium (commercial grade 99.85%) with fast neutrons of fluence of 8×10^{17} per cm at a temperature of 80°C. Afterward, they annealed it successively at several different temperatures from 350°C to 1000°C for about one hour each in a vacuum of about 10^{-7} torr. The defects present were studied using transmission electron microscopy at each stage. They found two types of defects after irradiation. The defects found

were vacancy type dislocation loops of diameter around 45 Å and interstitial type dislocation loops of diameter from 160 Å to 600 Å. The large interstitial type loops consisted of several clusters which transformed into a single dislocation loop upon subsequent annealing. They also reported the interstitial type loops were found only in the interior of the grains while the vacancy type loops were distributed uniformly. According to the report, the principle change made by annealing at 350°C, was an approximately 45 % decrease in the density of the small vacancy type dislocation loops. In contrast, the annealing at 480°C and 550°C changed the overall dislocation density little but the size of the large loops decreased while the small loops increased in size which made the two kinds of dislocation loops indistinguishable.

The sharp decrease of the volume pinning force at low dc field by the annealings at 455°C and 579°C, compared with the report by Chang and Chen, seems to suggest that the large dislocation loops are responsible for the volume pinning force at the low field and the role of the small loops is not significant. However, at fields close to H_{c2}, almost all sizes of dislocation loops contribute to the volume pinning force. This suggests that there may be a pinning threshold which decreases faster than the elementary pinning force as the field approaches H_{c2} so that the elementary pinning forces of the small loops are above the

threshold at high magnetic field but fall below the threshold at low field.

Figure 5.14 Total pinned magnetic field vs. the dc field (sample #20).

× room temperature

⊠ one hour at 135 C

△ one more hour at 365 C

▽ one more hour at 415 C

□ one more hour at 579 C

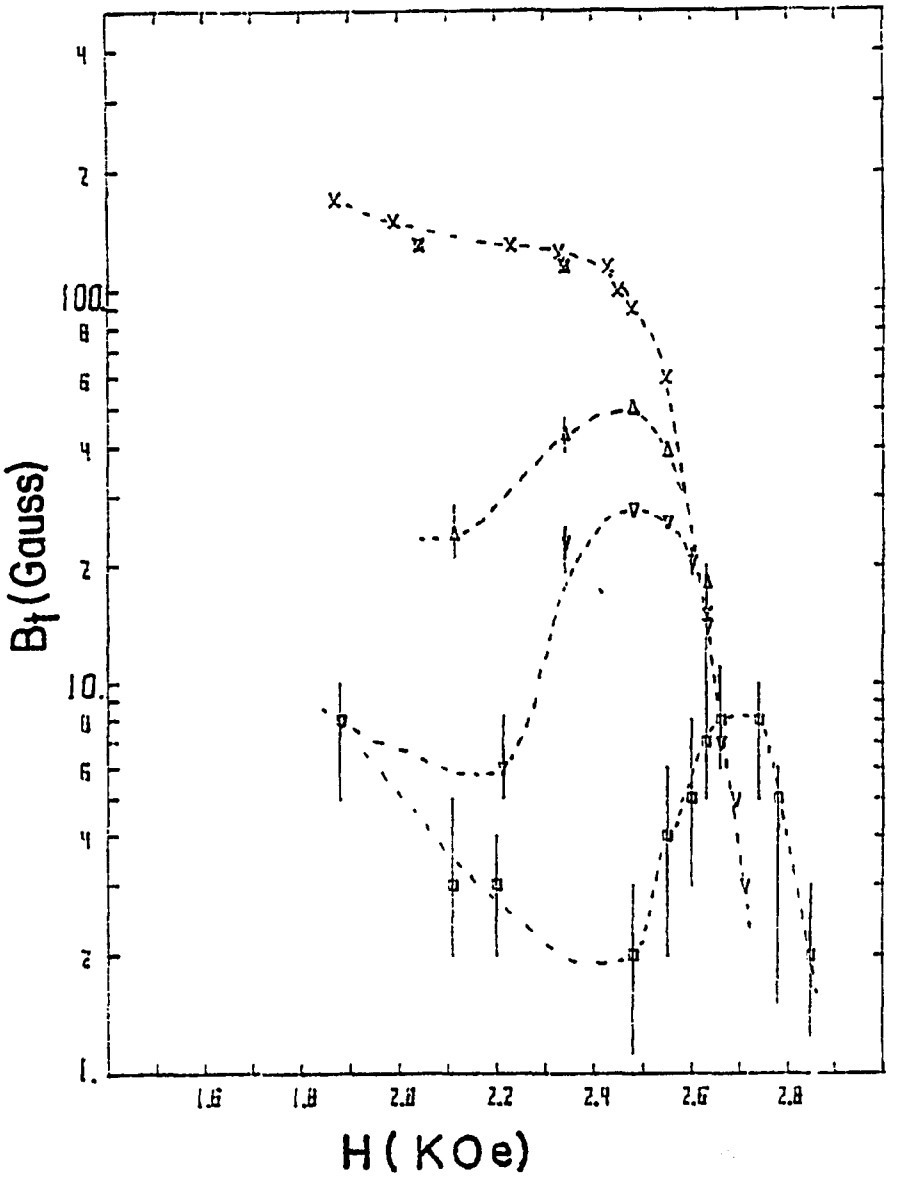
B_f (Gauss)
H (KOe)
4
2
100.
8
6
4
2
10.
8
6
4
2
1.
1.6
1.8
2.0
2.2
2.4
2.6
2.8

Figure 5.15 The size distribution of the defect cluster in pure Nb as a function of the annealing temperature (Chang and Chen 1977).

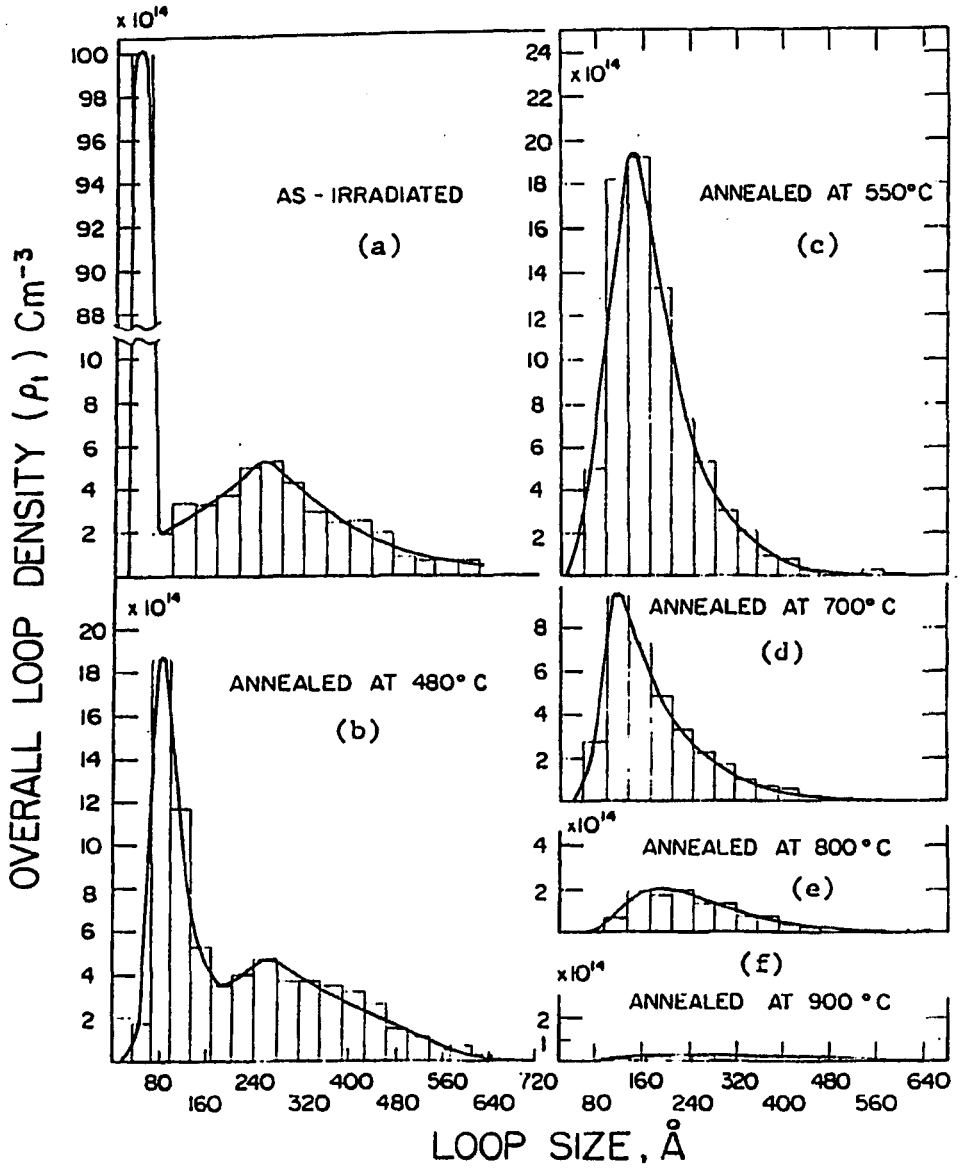
OVERALL LOOP DENSITY (ρ_1) Cm^{-3}
LOOP SIZE, Å
AS - IRRADIATED
(a)
ANNEALED AT 480° C
(b)
ANNEALED AT 550°C
(c)
ANNEALED AT 700° C
(d)
ANNEALED AT 800° C
(e)
(f)
ANNEALED AT 900 °C
x 10^14

5.6 Time Dependence of Total Pinned Magnetic Field and Cycling Effects.

Perhaps the most significant new finding in these experiments is the observation of a time dependent behavior of the volume pinning force at low magnetic fields. A small cycling effect and a slight decrease of the total pinned magnetic field, B_t, over a few minutes are observed at low dc fields in most of the samples but the size of the effect was usually less than 5 %. However, sample #16 after the 3rd irradiation showed much more evident time dependent and cycling effects. Immediately after the field was brought down to 1.88 KOe from above H_{c2}, a clear 30 % reduction in B_t during the first ten minutes was observed when a 40 Oe ac field was used (Fig. 5.16). This sample also displayed a large cycling effect (Fig. 5.16 and 5.17). However, when a 60 Oe ac field was used, the decrease of B_t with time and the cycling effects were less profound than those observed using a 40 Oe ac field (Fig. 5.17). Only small effects were observed when a 90 Oe ac field was used. Since it is unthinkable that the crystalline defects themselves changed their structure at liquid helium temperature, the dependence of the FLL structure on time and field history might be resposible for the time dependent and cycling effects (Kupfer and Gey 1977). There is a temptation to suspect that this decrease in the volume

pinning force with time is a universal phenomenon but that the time constants are too short or too long in most cases to be observed readily since it takes several minutes to complete one field profile measurement.

Figure 5.16 The time dependent behavior of the volume pinning force. The field profiles of sample #16 after the 3rd irradiation. H_{dc} = 1.88 KOe with a 40 Oe ac field.

Non-cycled state (the magnetic field was brought down from above H_{c2}).

⊠ 1 minute later.

▲ 10 minutes later.

⧗ 20 minutes later.

Cycled state (the magnetic field was brought up from below H_{c1}).

× 1 minute later.

△ 10 minutes later.

⧖ 20 minutes later.

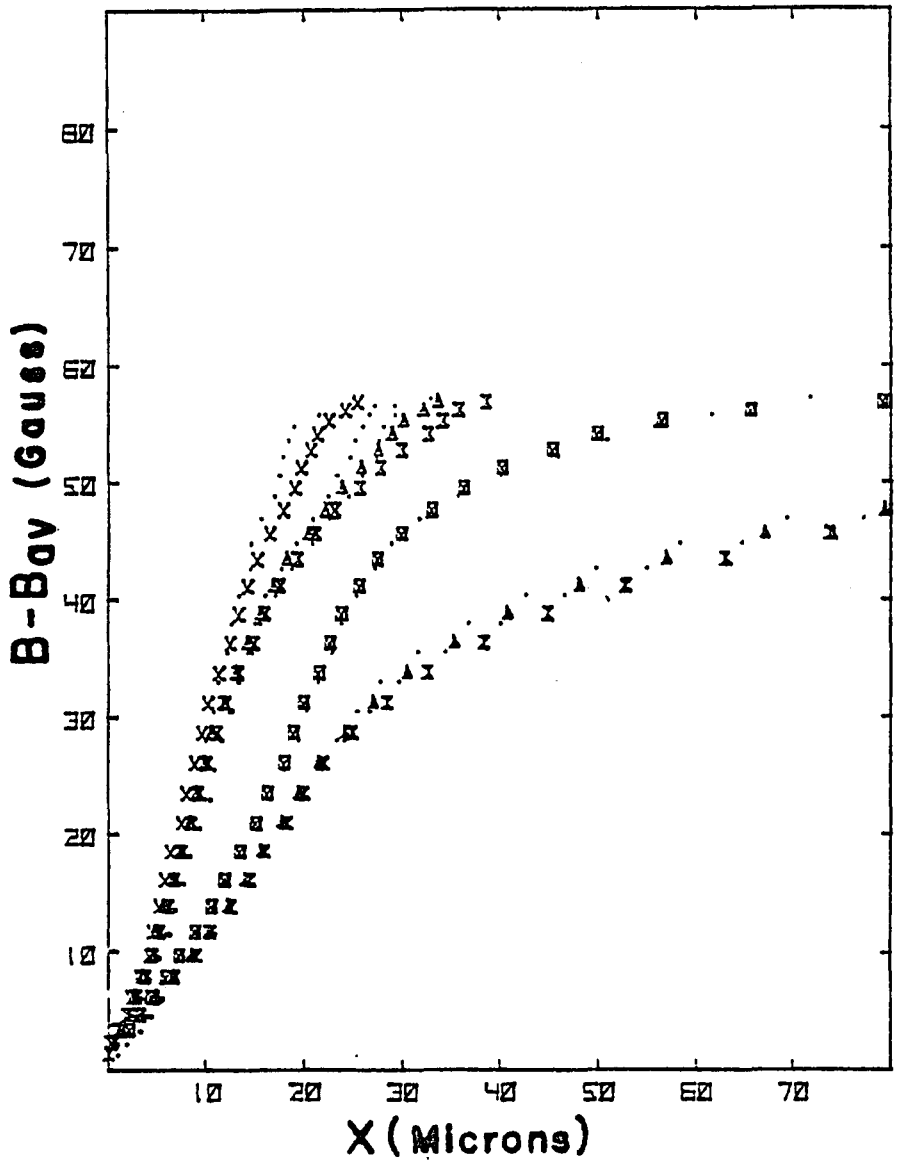
B-Bav (Gauss)
X (Microns)
10
20
30
40
50
60
70
80

Figure 5.17 The time dependent behavior of the volume pinning force. The field profiles of sample #16 after the 3rd irradiation. H_{dc} = 1.88 KOe with a 60 Oe ac field.

Non-cycled state.

⊠ 1 minute later.

▲ 10 minutes later.

Cycled state.

× 1 minute later.

△ 10 minutes later.

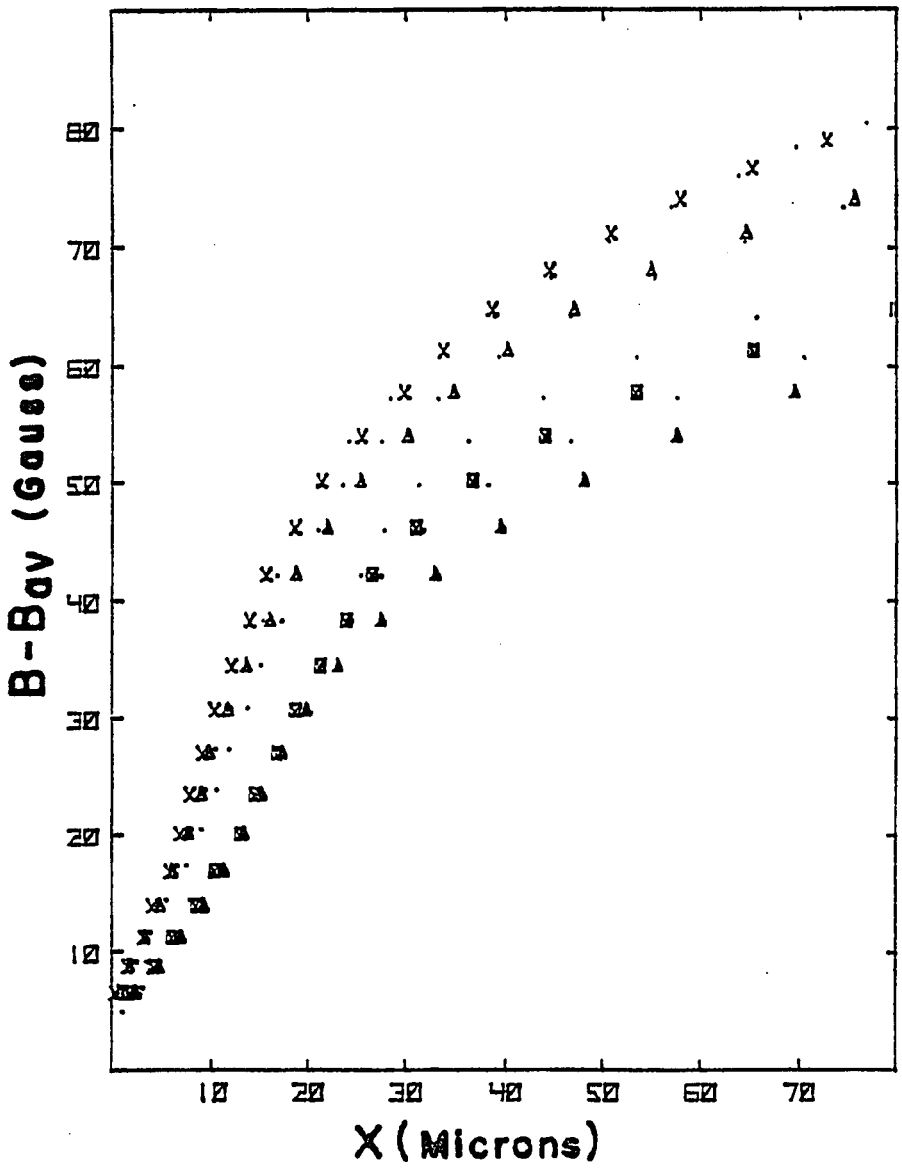
B-Bav (Gauss)
X (Microns)
10
20
30
40
50
60
70
80

5.7 Summary.

The following is a brief summary of the general experimental results which are not adequately explained by current theories.

1) A peak was observed in most samples in the volume pinning force near H_{c2}. When the overall pinning force is small, the peak is sharp and occurs at a field just below H_{c2}. As the overall pinning force increases, the peak moves to a lower field and its sharpness decreases.

2) The volume pinning force increases faster than quadratically with the proton fluence at fields below the peak but the increase is much slower at fields above the peak.

3) Some samples display the cycling effect and a time dependent effect in the volume pinning force. These effects depend sensitively on the nature of sample and also on the ac field amplitude.

Since it is highly unlikely that the increase of the proton fluence actually reduces the crystalline defect density, the progressive shift of the peak to the lower magnetic field as the proton fluece increases (item 1 above) can not be explained by the synchronization proposition (Sec. 3.3). If the increase of the elementary pinning force is responsible for this shift, the fact that the volume pinning force increases more at lower magnetic field

(item 2 above) might suggest the existence of a pinning threshold much smaller than the threshold of the FLL instability model. If such pinning threshold exists for some reason, the small pinning centers which can not contribute to the volume pinning force may grow larger and come into play as the proton fluence increases. However, this effect may not be observed at fields close to H_{c2} because all the pinning centers may already be above the threshold at low proton fluences.

It is very hard to imagine that the crystalline structure would change or depend on the history of the magnetic field at liquid helium temperature and we can safely assume that the structural change of the FLL causes the cycling effect and the time dependent bahavior of the volume pinning force. It seems to be quite possible that the FLL structure depends on the field history or has some time constant in its response to the external field (Chapter 6).

Finally, electron micrographs taken on similarly prepared proton irradiated Nb samples by Anjaneyulu (1977) (Anjaneyulu and Rollins 1979) show the density and size of the dislocation loops obtained. This allowed a comparison between measured and calculated values of the volume pinning force, F_V. Using the FLL instability model they found F_V calculated was about two to three orders of magnitude smaller than the measured value. Anjaneyulu (1977) also

found the dislocation loops (although rather large in size with average diameter of about 300 Å) have an elementary pinning force, f_p, which is about three orders of magnitude below the threshold predicted by the FLL instability model (Labusch 1969 and Kramer 1976). Thus, unless we neglect the threshold criterion, we would not expect to see any pinning at all in our samples.

Chapter VI

Flux Line Lattice Defect Instability Model

6.1 Introduction.

It is clear from the experimental evidence that flux pinning is observed when the elementray pinning force, f_p, is several orders of magnitude below the threshold predicted by the Labusch statistical summation model which we have referred to as the FLL instability model. The threshold appears in this model because it requires an instability in the deformation of the perfect FLL by a local pinning center. The existence of the instability is essential in the model in order that the stastical summation leads to a non-zero volume pinning force. This leads to the calculated threshold which is too large.

We suggest that what is needed is a different type of instability in the flux line lattice. Clearly the evidence suggests that the previously suggested instability in a perfect lattice is not the correct instability. What follows in this chapter is a proposed instability mechanism. The proposal is qualitative in nature but could lead to more quantitative calculations. Consideration of the particular mechanism suggested below for the instability may lead to further suggestions of other complex instabilities.

We propose that the instability which leads to a lower threshold pinning force depends on the motion of defects which are present in the FLL. The existence of such FLL defects (FLLD), especially FLL dislocation lines, has been well accepted for some time (see Chapter 2.3). We are led to suggest FLL defects are the key to the instability partly because of the experimental evidence that the volume pinning force depends on the structure of the FLL. For example, the cycling effect which we observed (Sec. 5.6) and has also been reported by others (Kupfer and Gey 1977), shows that the volume pinning force in certain situations depends on the magnetic field history of the sample. Also, Campbell and Evett (1972) observed large changes (factor of three) in the volume pinning force when edge dislocations were artificially induced in the FLL by small external coils which caused local field variations in the sample.

Several authors have concerned themselves with the effect which dislocations in the FLL will have on the volume pinning force. However, the unstable motion of FLL dislocations has not been suggested as a possible source of an instability in the FLL which may also lead to a low pinning threshold. Attention has been given to the possible effect of FLL dislocations on the elastic constants of the FLL (Kramer 1978). There have been several suggestions that FLL dislocations move easily through the FLL (Schmucker 1974 and Kramer 1978) and that the

interactions between pinning centers and FLL dislocation lines are strong (Kusayanagi and Yamafuji 1969, Schmucker 1974, Chang et. al. 1969, and Campbell and Evetts 1972).

In this chapter, we assumed that many of the suggestions of others about the motion and pinning of FLL defects (FLLD) are true. It is assumed that the FLLD movement through the FLL can be induced by pinning centers. A model is described in some detail which indicates that motion of the FLLD in the presence of pinning centers can give rise to a new type of instability in the FLL and hence, can give rise to a volume pinning force. The model is similar, in principle, to the FLL instability model but the nature of the instability of the new model is with respect to the position of the FLL defects and therefore, it will be referred to as the FLLD instability model. This model is combined with the statistical summation method to obtain a general relationship between the elementary pinning force and the volume pinning force.

6.2 FLLD Instability Model.

It is assumed that the elementary pinning force is below the threshold of the FLL instability model and hence, the statistical summation over all pinning centers would

lead to zero volume pinning force on a perfect FLL. However, a pinning center exerts a local force on the FLL causing a stress-strain field around the pinning center. If there is a FLLD not far from this pinning center, it will experience a force through the interaction of the FLL stress-strain field induced by the pinning center and the FLL stress-strain field of the FLLD. It is shown that if the interaction force between the pinning center and the FLLD is large enough to move the FLLD (a new, and much lower, threshold criterion), then there is an instability in the position of the FLLD related to the pinning center and also an instability in the positions of the flux lines around the FLLD.

6.2.1 Forces Acting on a FLLD.

The following four forces may act on a FLLD. All the position vectors are with respect to the ideal undistorted FLL.

a) A FLLD at r_l will experience a periodic force $F_l(r_l)=A\ H_l(r_l)$ as it moves through the FLL due to the periodic structure of the FLL. $H_l(r_l)$ is a periodic function varing between 1 and -1 and has the periodicity of the FLL and A is a constant which depends on the intrinsic

superconducting parameters and the type and the shape of the FLLD.

b) The pinning force of a point pinning center at r_2 can be expressed as $F=f_p H_2(r_2)$ if the FLL is otherwise undistorted, where f_p is the elementary pinning force and $H_2(r_2)$ is another lattice periodic function varing between 1 and -1. However, in the presence of a FLLD at r_1, the pinning force is $F=f_p H_2[r_2-u(r_2-r_1)]$ where $u(r_2-r_1)$ is the distortion of the FLL at r_2 due to the FLLD at r_1. The pinning center then induces a force $F_2=F\ G(r_2-r_1,F)$ on the FLLD due primarily to the interaction of the stress-strain fields of the FLLD and the FLL distorted by the pinning center. Generally we would expect $G(r_2-r_1, F)$ to be a weak function of F which reaches a maximum for small r_2-r_1 and approach zero as $r_2-r_1\to\infty$.

c) The FLLDs interact with each other.

d) Any general flux density gradient will produce a net force on the FLLD.

6.2.2 Origin of the Instability.

Let's consider a one dimensional case of a single pinning center at x_2 moving from negative infinity toward a FLLD. The forces (c) and (d) above do not exist in this

case and again all the positions are with respect to the ideal undistorted FLL.

The FLLD will take a position in the FLL such that the total force, F_t, on the FLLD is zero.

$$F_t = F_1 + F_2$$

$$= A\, H_1(x_1) + f_p H_2[x_2 - u(s)]\, G(s) = 0$$

or

$$H_1(x_1) = -[f_p G(s)/A]\; H_2[x_2 - u(s)] \tag{6.1}$$

where $s = x_1 - x_2$ and $G(s)$ is maximum when $s=0$ and goes to zero as $s \to \infty$. When f_p is equal to or smaller than $A/G(0)$, which will be called the critical pinning force f_c, Eq. 6.1 has at least one real root for x_1 in all periods of $H_1(x_1)$ or, in other words, the FLLD is stable regardless of the distance from the pinning center. The FLLD simply goes through an oscillatory motion as the pinning center produces a periodic force as it moves through the FLL. The whole process is reversible and there is no volume pinning force. However, if $f_p > f_c$, there exists a value s_0 where $f_p = A/G(s_0)$. Then Eq. 6.1 has no real root for x when $|s| < s_0$ and the pinning force $F = f_p H_2(x_2 - u)$ becomes larger than f_c (Fig. 6.1). If a FLLD is in this instability region, it will

jump irreversibly out of this region, thus, producing the instability which is essential for the volume pinning force. The critical pinning force, f_c, which is the minimum force necessary to move a FLLD, is much smaller than the force required to move the flux lines or the pinning threshold of the FLL instability model (Sec. 6.4).

The maximum force on the FLL to move the FLLD will occur when the pinning center just comes to within the distance s_0 of the FLLD. If the pinning force reaches its positive maximum at this point, the FLLD will be pushed away from the pinning center and stability will be restored immediately. However, when the pinning force reaches its negative maximum after the above process or when it first comes into the instability range (Fig. 6.2 a), the FLLD at x_{1a} will be pulled toward the pinning center at x_{2a} where $H_2[x_{2a}-u(x_{1a}-x_{2a})]=-1$ and $G(x_{1a}-x_{2a})=A/f_p$. The FLLD does not stop immediatly because G(s) increases as $s=x_1-x_2$ decreases while the pinning force F at its peak does not change rapidly, which makes $F_2= F\,G(s)$ even larger as the FLLD moves toward the pinning center (Fig. 6.3). However, the distortion u(s) becomes large as the distance s decreases and the pinning force F and, therefore, F_2 starts to decrease until the FLLD reaches x_{1b} where $f_pH_2[x_{2a}-u(x_{1b}-x_{2a})]=-A/G(x_{1b}-x_{2a})$ and stability is restored (Fig. 6.2 b). Meanwhile, the pinning center has not moved although the pinning force changed due to the movement of

the flux lines around it. The pinning center moves reversibly afterward until it reaches x_{2c} and the pinning force becomes large enough to move the FLLD again i.e. $f_p H_2[x_{2c}-u(x_{1b}-x_{2c})]=A/G(x_{1b}-x_{2c})$. In this stage, the pinning center pushes the FLLD away as it moves until the pinning force reaches its peak at x_{2d} where $H_2[x_{2d}-u(x_{1d}-x_{2d})]=1$. The process becomes reversible again afterward until the pinning force reaches its negative maximum which is the beginning of the next cycle. Therefore, the average pinning force over a cycle, F_{av}, is

$$F_{av} = \frac{1}{L}\int_a^e F\,dx_2$$

$$= \frac{1}{L}\left[\int_b^c F\,dx_2 + \int_c^d F\,dx_2 + \int_d^e F\,dx_2\right].$$

But

$$\int_b^c F\,dx_2 = \int_d^e F\,dx_2 = 0$$

because of the periodic nature of $F_2(x_2)$. Therefore,

$$F_{av} = \frac{1}{L}\int_c^d F\,dx_2$$

$$= \frac{1}{L}\int_c^d f_p H_2[x_2 - u(x_1 - x_2)]\, dx_2$$

$$= f_p\, C(f_p) \quad , \tag{6.2}$$

where

$$C(f_p) = \frac{1}{L}\int_c^d H_2\langle x_2 - u(x_1 - x_2)\rangle\, dx_2 \tag{6.3}$$

and L is the FLL constant.

The detailed behavior of $C(f_p)$ is complicated and obviously depends on the type of pinning center and the type of FLL defect. However, we can speculate about the general qualitative behavior of $C(f_p)$. When $f_p < f_c$, $C(f_p)$ and the volume pinning force are zero. As f_p increases above f_c, the instability range and, therefore, the FLLD movement and $C(f_p)$ increase rapidly. However, when $f_p >> f_c$, the further increase of f_p might increase the range of the FLLD movement but does not increase $C(f_p)$ much because the distortion in the FLL at the pinning center is small when the FLLD is far away. The limiting maximum in $C(f_p)$ for the one dimensional case of a single FLLD and a single pinning center with a sinusoidal force is

$$C(f_p) \simeq \frac{1}{\pi} \int_0^{\pi/2} \sin x \; dx = \frac{1}{\pi} . \tag{6.4}$$

The volume pinning force which is a sum of the average pinning forces should, therefore, depend linearly on f_p when $f_p \gg f_c$ and decrease rapidly to zero as f_p approaches f_c.

In the real case, the FLLD may move around the pinning center left behind rather than staying in the line of the pinning center movement, thus, reducing $C(f_p)$ considerably. However, unless the pinning center density is very low or the instability range is too small ($f_p = f_c$), there might always be at least one pinning center within the instability range from each FLLD. Furthermore, the movement of FLLD affects not only the pinning center which causes the movement but all the pinning centers under its influence. Therefore, even if the FLLD density is not high enough so that every pinning center corresponds to one FLLD, still most of the pinning centers could be under the influence of at least one FLLD and contribute to the volume pinning force.

Figure 6.1 The force on a FLLD.

(a) without the pinning center ($f_p = 0$).

(b) when $f_p < f_c$.

(c) when $f_p > f_c$.

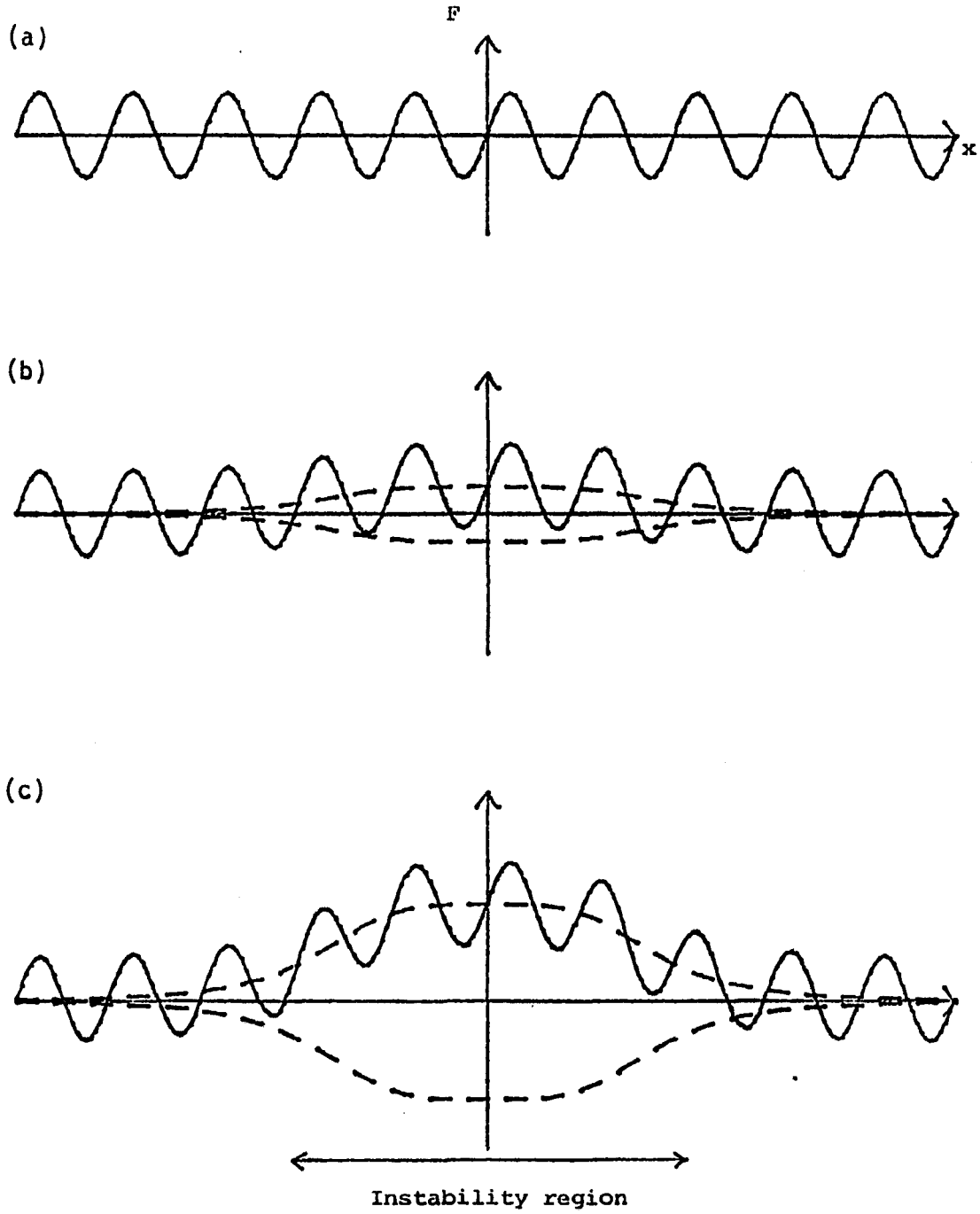
(a)
F
x
(b)
(c)
Instability region

Figure 6.2 The relation between a pinning force and a FLLD when $f_p > f_c$.

(a) The beginning of the instability (the pinning force is at its negative maximum).

(b) The end of the instability (the pinning force decreased but the pinning center did not move).

(c) The beginning of the next instability.

(d) The end of the instability (the pinning force is at its positive maximum).

(e) The beginning of another cycle.

(f) The pinning force during a complete cycle.

The FLLD moves (a) to (b) in one step but moves (c) to (d) gradually as the pinning force increases.

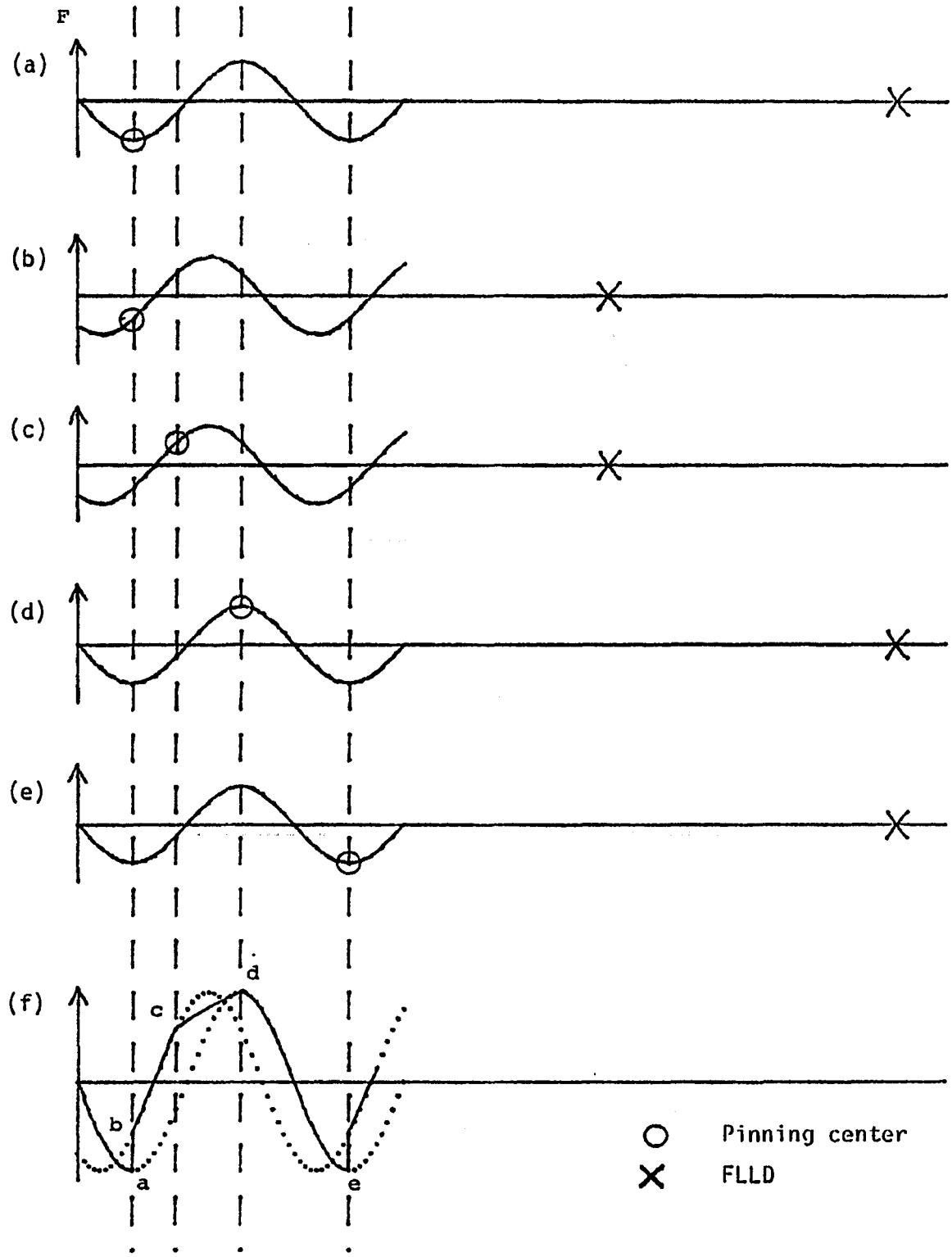
F
(a)
(b)
(c)
(d)
(e)
(f)
a
b
c
d
e
Pinning center
FLLD

Figure 6.3 The relation between the pinning force and the FLLD position during the step from (a) to (b) in Fig. 4.2.

(a) Pinning force vs. position of a pinning center.

- - - - - Perfect FLL.

——— FLL with FLL defect.

(b) Force on a FLLD vs. Position of the FLLD. A pinning center is at origin.

(1) The beginning of the instability.

(2) In the middle.

(3) The End of the instability.

a.

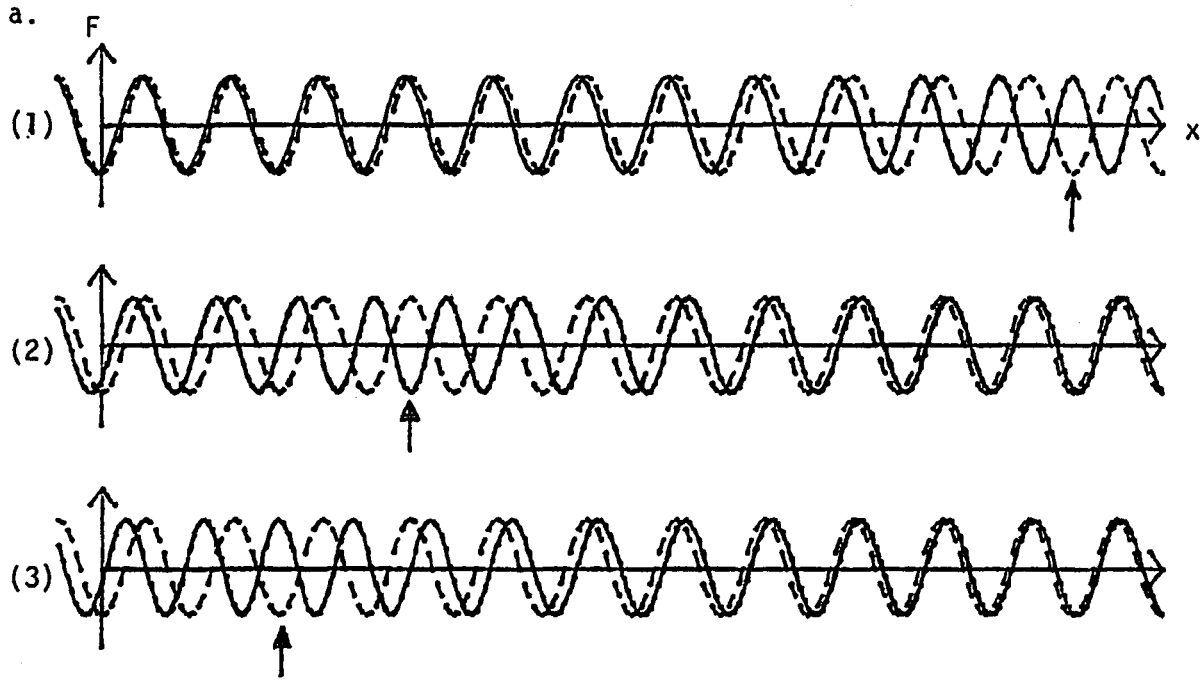

b.

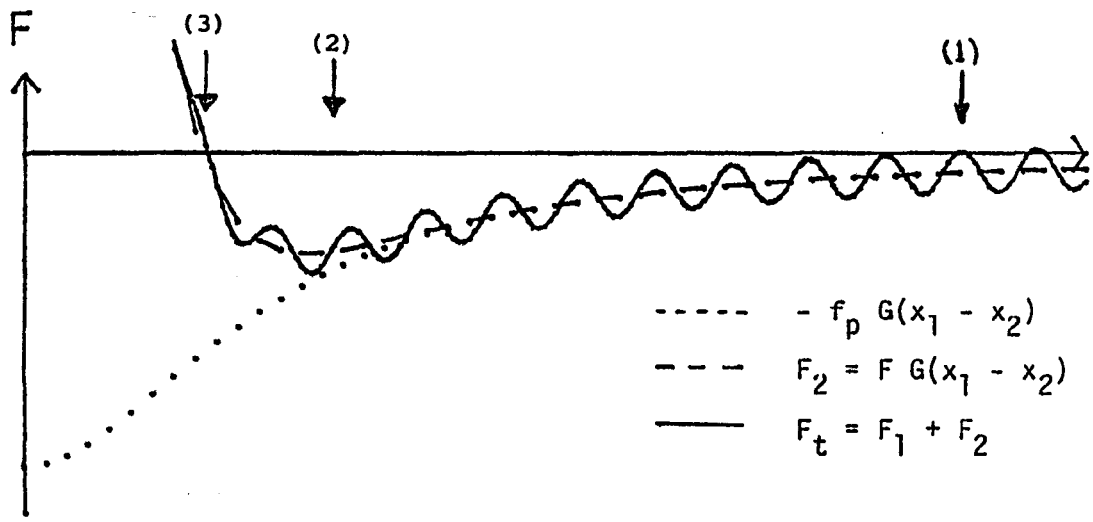

6.3 Origin of FLLD.

The flux line lattice is known to contain defects of various types. However, little is known about how these defects are created or how they affect the macroscopic superconducting properties of a material.

The flux line density gradient seems likely to be achieved by the introduction of edge dislocation lines rather than by a gradual density change. However, this can not be considered as a FLLD source which leads to the flux pinning since the volume pinning force is a prerequisite to the flux density gradient. The displacement of the flux lines, even by the largest pinning force available, is generally too small to produce the FLL defects except at fields very close to H_{c1} or H_{c2} and it is quite unlikely that a pinning center can be a source of the FLLD in general (Sec. 2.2). However, the displacements of the flux lines by a pinning force can be large at a field very close to H_{c1} or H_{c2}. The pinning center can be a source of the FLLD when the displacement of a flux line is equal to or larger than the FLL constant. Furthermore, since a sample must pass either H_{c1} or H_{c2} to reach the mixed state, if the FLLDs created when the field is close to H_{c1} or H_{c2} stay in the FLL, The FLL could have many defects without any source at that particular magnetic field. The FLL defects can also be produced as the flux lines enter through the sample

surface. When the magnetic field increases, the new flux lines penetrate into the sample through the surface. The flux lines may not enter uniformly due to irregularities in the sample surface or in the external magnetic field, thus, forming the FLL defects. Also the FLL defects may be formed during the FLL formation itself at H_{c2}.

A two dimensional vacancy or an interstitial can, roughly speaking, be considered as two edge dislocation lines face to face and the energy required to produce a pair of dislocation lines is smaller than the energy required to produce a vacancy-interstitial pair. A dislocation line also has a specific glide plane and it is possible for dislocation lines to be annihilated only when two identical dislocation lines of opposite sign are close together on the same glide plane. Compared to dislocation lines, vacancies or interstitials should be produced in small numbers and also they can be readily annihilated. Furthermore, when two edge dislocation lines are not on the same glide plane, they do not simply repel or attract but they have well defined equilibrium positions with respect to each other (Fig. 6.4). Therefore, the movements of the dislocation lines are quite restricted and even when the magnetic field moves into the range where the FLLD can not be produced, still a large portion of the dislocation lines should remain in the FLL. The FLL may look 'fluid-like' at a field where the FLL elastic constants are so small that the pinning

centers can easily move the flux lines and as the field increases beyond this region, vacancies and interstitials might recombine leaving the dislocation lines as the major FLLD.

Figure 6.4 The forces and the stable configurations between parallel edge dislocation lines (Kovacs and Zsoldos 1973).

(a) The force acting between two edge dislocation lines with perpendicular Burgers vectors.

(b) The force acting between two edge dislocation lines with parallel Burgers vectors.

(c) The stable configurations between two edge dislocation lines with perpendicular Burgers vectors.

(d) The stable configurations between two edge dislocation lines with parallel Burgers vectors.

The dislocation lines enclosed by triangles are considered as fixed. The arrows indicate the direction of the force on the dislocation which is free to move along its glide plane.

(a)

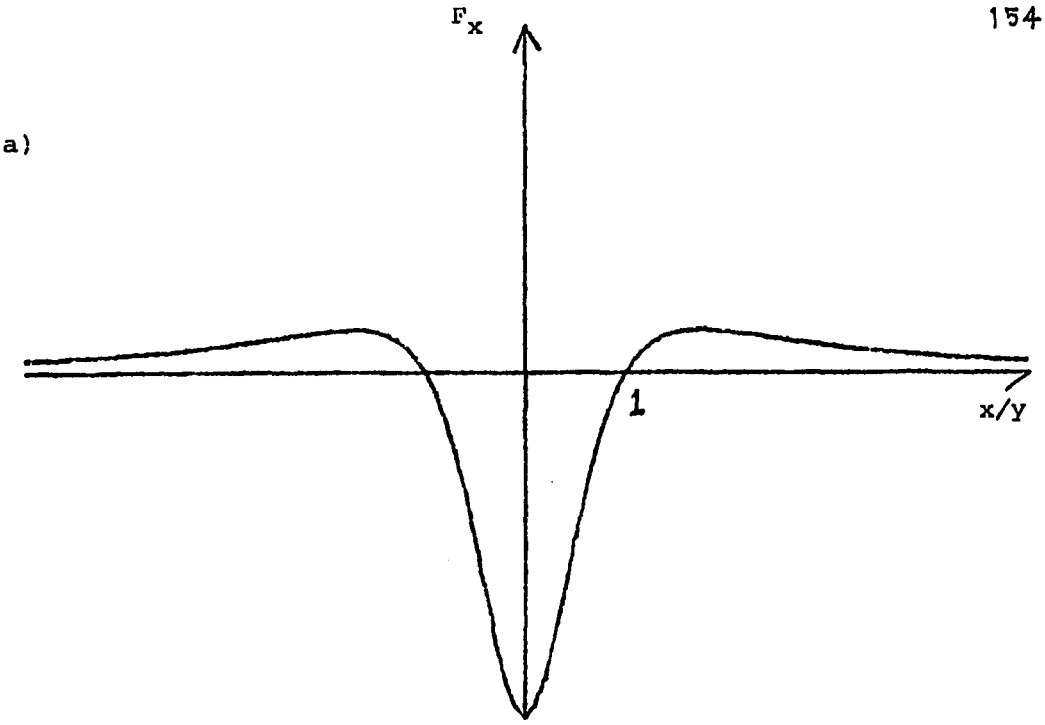

(b)

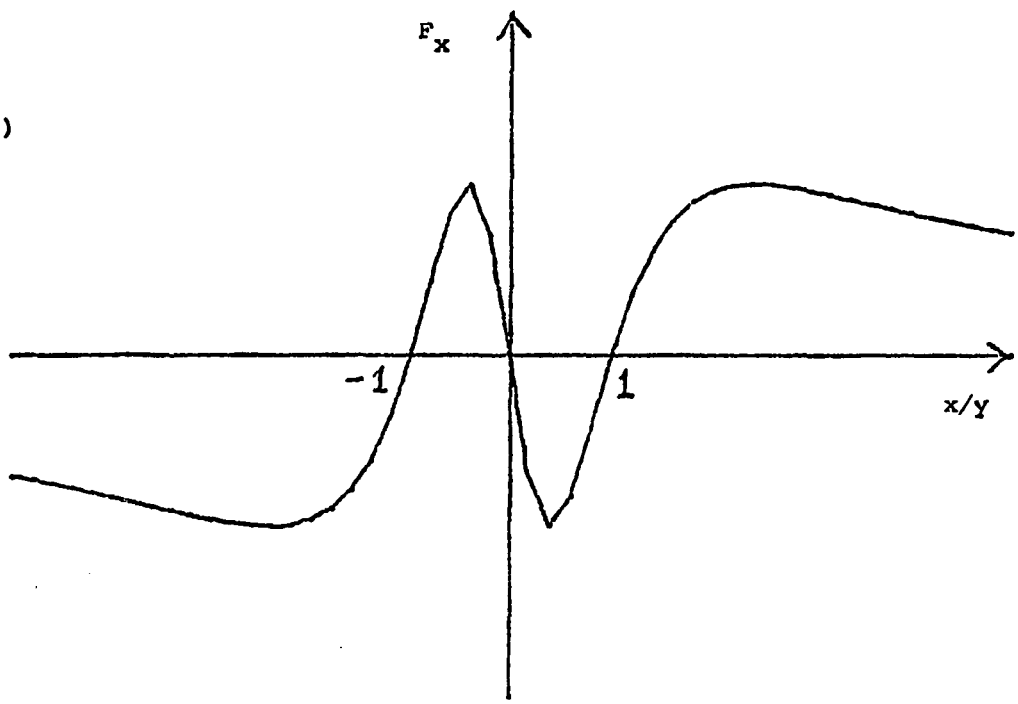

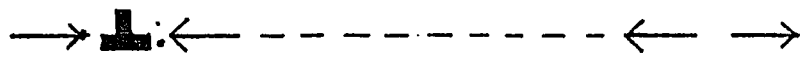

(c)

(d)

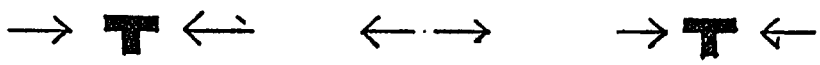

6.4 Critical Pinning Force.

Although the FLL is known to contain defects of various types, it may be sufficient to consider only FLL dislocation lines since defects of other types are low in density and their critical pinning forces should be larger than that of the edge dislocation lines. A calculation of the critical pinning force requires a complete understanding of the FLLD and its interaction with pinning centers. However, a general comparison with the pinning threshold of the FLL instability model can be made using the results of ordinary dislocation theory applied to crystalline lattice.

Peierl's model gives the stress s_{xy} at a distance x from an edge dislocation line as (Kovacs and Zsoldos 1973)

$$s_{xy} = \frac{b}{2\pi c} \sin\left(-2 \arctan \frac{2x}{s}\right) \tag{6.5}$$

where $s=c/(1-\nu)$, $\nu=\lambda/2(\lambda+\mu)$ and b is the Burgers vector which is the distance between the lattice points along the glide plane; c is the interlayer distance; λ is the bulk modulus and μ is the shear modulus. For two dimensional cases, λ and μ are c_{11} and c_{66} respectively (Sec. 2.2). The critical shear stress to move a dislocation line (Peierl's stress), s_c, is given by (Kovacs and Zsoldos 1973)

$$s_c = \frac{2}{1-\nu} e^{-2\pi c/b(1-\nu)} \tag{6.6}$$

In the case of the trianqular flux line lattice $(c/b=\sqrt{3}/2)$ and $\lambda >> \mu$, $\nu = 0.5$ and the critical shear stress is

$$s_c \simeq 4\mu \exp(-2\sqrt{3}\pi) \simeq 7.5 \times 10^{-5} \mu . \tag{6.7}$$

Kramer (1973) estimated the critical shear stress for the perfect flux line lattice to be about $\mu/6$. Thus, the stress needed to move a FLL edqe dislocation line is about three orders of maqnitude smaller than the stress needed to move the flux line itself. On the other hand, the interaction force between a FLL defect and a pinninq center seem to be similar to the interaction force between a flux line and a pinninq center. Kusayanaqi and Yamafuji (1969) estimated the interaction energy between a FLL edqe dislocation and a crystalline screw dislocation and obtained a value of same order as the sinqle flux line interaction with a crystalline screw dislocation. If other pinninq centers act similary, the critical pinning force might be about three orders of maqnitude smaller than the pinning threshold of the FLL instability model. In case of crystalline dislocation lines, this estimation of the critical stress generally qives a value which is one order of maqnitude larqer than the value obtained experimentally. If the FLL dislocations lines act

similarly, the magnitude of the critical force needed to move a FLL dislocation may be near four orders of magnitude less than the pinning threshold of the FLL instability model.

Figure 6.5 Illustrative diagram describing the peak effect. The scales are arbitrary.

(a) The elementary pinning force, f_p, and the critical pinning force, f_c.

(b) $C(f_p)$ goes to zero where $f_p = f_c$

(c) $F_v = f_p\, C(f_p)$ has a peak.

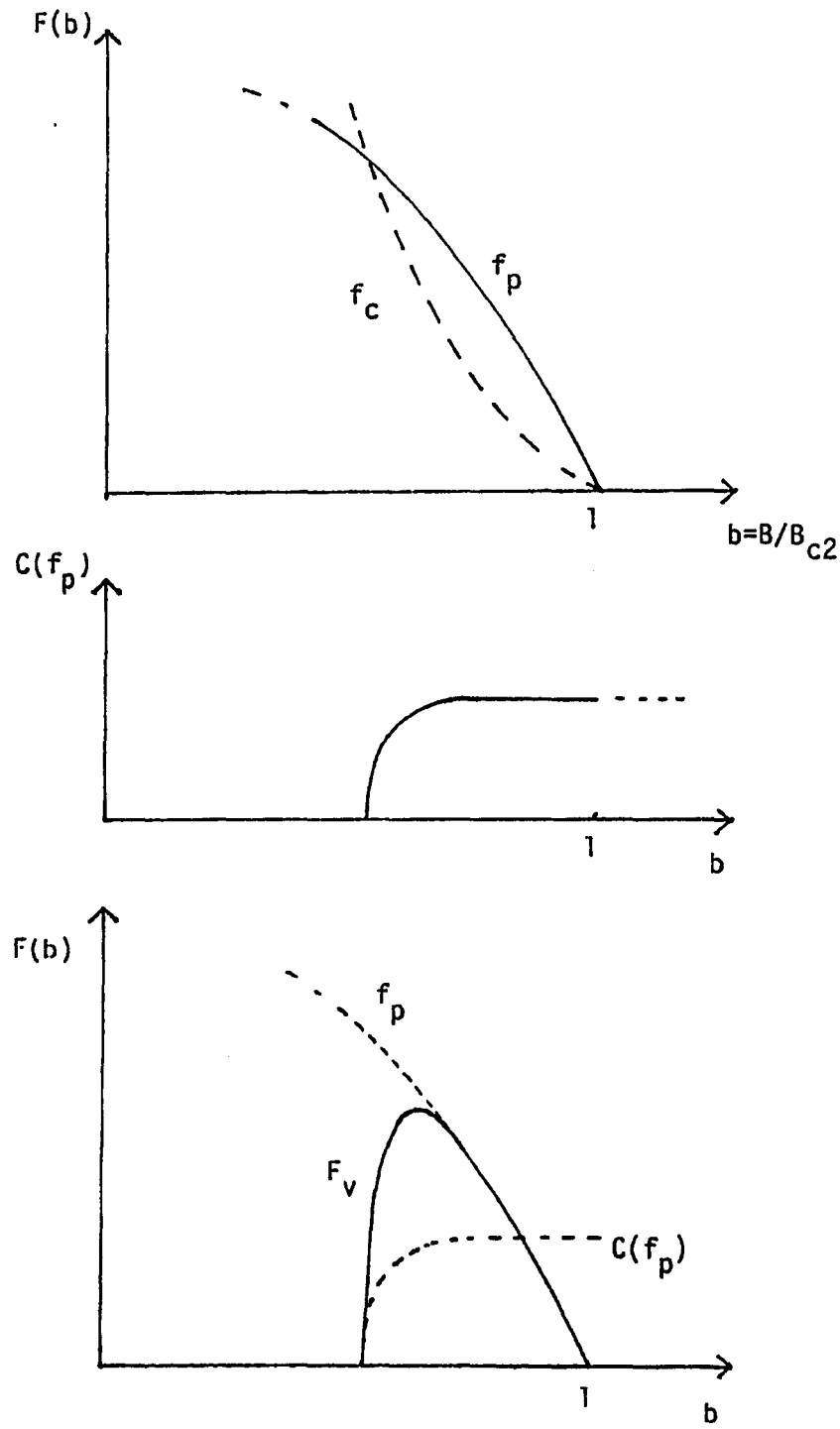
F(b)
f_p
f_c
1
$b=B/B_{c2}$
$C(f_p)$
1
b
F(b)
f_p
F_v
$C(f_p)$
1
b

6.5 Interpretations of Experimental Results.

To calculate the volume pinning force and its behavior, the types and the shapes of the FLLD and their densities should be determined first and this seems to be beyond immediate reach. However, much of the experimental phenomena previously unexplained can be explained at least qualitatively by the FLLD instability model. In this section, the experimental results are explained one by one in terms of the FLLD instability model.

6.5.1 Specific Pinning Force vs. Volume Pinning Force.

The specific pinning force Q (the volume pinning force per pinning center) or the average pinning force is several times smaller than the elementary pinning force, f_p, even if all the pinning centers are under the full influence of a FLLD all the time (Sec. 6.2). Q, in a real case, should be even smaller since the FLLD density may not be as high as that of the pinning centers. The experimental result (see Sec. 3.3 and Fig. 3.2) that Q is about one order of magnitude smaller than f_p agrees well with this model. Specially, the FLLD instability model predicts the dependence of Q on f_p is roughly linear when $f_p >> f_c$ but Q should

decrease to zero rapidly as f_p approaches f_c which is about four orders of magnitude smaller than the pinning threshold of the FLL instability model . This prediction agrees well with the experimental results summerized by Kramer in Fig. 3.2 as discussed in Sec. 3.3.

6.5.2 Proton Fluence Dependence of Volume Pinning Force and the Peak Effect.

The elementary pinning force increases rapidly as the magnetic field decreases from H_{c2} and so does the volume pinning force. As the field decreases further, the critical pinning force increases more rapidly than the elementary pinning force does (Schmucker and Brandt 1977) and where these two values become equal, the volume pinning force goes to zero rather abruptly, thus, producing the peak effect (Fig. 6.5). In reality, however, there is always a distribution in the size of the pinning centers and also in the direction of the glide planes of the FLL dislocation lines which make the transition less sharp. When the pinning centers are very small, as is the case in the samples with a small proton fluence, the peak occurs just below H_{c2} and the volume pinning force goes to zero or becomes very small below the peak producing very sharp peak effect. When the pinning

centers are large or the proton fluence increases, presumably the size distribution of the pinning centers also becomes broad making the peak less sharp and shifting it to a lower field. When most of the elementary pinning forces stay above the critical pinning force over the whole field range, as in the case of pinning by some voids and precipitates as discussed by Kramer (1978), the peak effect never occurs. Therfore, the proton fluence dependence of the volume pinning force is high at the low field since the pinning centers which are too small to contribute to the volume pinning force at the low proton fluence may grow large enough as the fluence increases. The dependence is much smaller at high fields since the smallest pinning centers may already contribute to the volume pinning force at the low fluence.

6.5.3 Cycling Effect and Time Dependence of Volume Pinning Force.

The density of the FLL dislocations could be quite different depending on whether they were formed with the FLL at H_{c2} and by the pinning centers as the field decreases or produced at the surface when the flux lines enter the sample as the field increases. Since $C(f_p)$ should depend on the average number of the FLLD per pinning center, this

difference in the FLLD density could be resposible for the cycling effect.

The FLL interstitial-vacancy pairs or even some FLL dislocation lines will recombine after they are produced. This reduction of the FLLD density might have caused the time dependence of the volume pinning force. Kupfer and Gey (1977) investigated the cycling effect of various samples and found only samples with pinning centers which displace the FLL by one hundredth to one tenth of the FLL constant also displayed cycling effects, while samples with larger pinning centers or smaller pinning centers did not display the cycling effect. When the elementary pinning force is large, the pinning centers may restrict the FLLD movement and the recombination might not be extensive. On the other hand, when the elementary pinning force is very small, the time constant is too small for this effect to be detected.

Chapter VII

SUMMARY

7.1 Experiment.

Dislocation loops were produced in pure defect-free niobium samples by room temperature irradiation with 3.2 Mev or 1.0 Mev protons and their magnetic flux pinning behavior at 4.2 degrees kelvin was examined. In spite of similar sample treatment, the volume pinning force and its magnetic field dependence were found to be quite different from sample to sample. Nevertheless, a low volume pinning force is accompanied by a sharp peak at a field close to H_{c2} while samples with a high volume pinning force display a weak peak at a lower field. Two samples were irradiated in three successive steps and their volume pinning forces increased sharply at low magnetic fields as the proton fluence increased. At fields close to H_{c2}, however, the increase in the volume pinning force was not as rapid nor was there such large differences between samples.

One of the samples showed a large cycling effect and a noticeable decrease in the volume pinning force over a 10 minute interval at an external field of 1.88 KOe or lower and when a 40 Oe ac field was used. These two effects decrease as the ac field amplitude increased. The volume

pinning force and the peak effect of this sample were intermediate in magnitude as compared with other samples.

7.2 FLLD Instability Model.

A new summation model of flux pinning based on the instability in the movement of the flux line lattice defects (FLLD) was developed. It is shown that when the elementary pinning force is larger than a critical pinning force, which is perhaps four orders of magnitude smaller than the threshold force of the FLL instability model, the pinning center can produce an instability in the movement of a flux line lattice (FLL) defect. This instability results in a net force when averaged over all possible positions of the pinning center and gives rise to a volume pinning force. This model is used to explain qualitatively most of the experimental results. Because of the uncertainties of the FLLD structure and their density, it is possible to discuss only general pinning behavior.

REFERENCES

Abrikosov, A.A. (1957) Zh. Eksperim. i Teor.fiz. 32, 1442

Adaktylos, I. and Weber, H.W. (1977) Philos. Mag. 35, 983

Agrawal, D.C., Kramer, E.J., and Loomis, B.A. (1974) Philos. Mag. 29, 559

Anjaneyulu, Y. and Rollins, R.W. (1979) J. Appl. Phys. 50, 1442

Anjaneyulu, y. (1977) Measurement of Magnetic Flux Pinning Near the Surface in Proton-Irradiated Thick Nb Samples., Ph.D. Thesis, Athens Ohio

Antesberger, G. and Ullmaier, H.A. (1974) Philos. Mag. 29, 1101

Bean, C.P. (1962) Phys. Rev. Letter 8, 250; (1964) Rev. Mod. Phys. 36, 31

Brandt, E.H. (1969) Phys. Stat. Sol. 36, 371; 36, 393; 36, K167

Brandt, E.H. (1976) Commu. Phys. 1, 57

Brandt, E.H. (1977) J. Low. Temp. Phys. 26, 709; 26, 753

Brandt, E.H. (1978) Philos. Mag. b 37, 293

Campbell, A.M., and Evetts, J.E. (1972) Adv. Phys. 21, 199

Campbell, A.M. (1969) J. Phys. c 2, 1492

Campbell, A.M. (1975) Philos. Mag. 31, 1191

Campbell, A.M. (1978) Philos. Mag. b 37, 149

Chang, C.C., McKinnon, J.B., and Rose-Innes, A.C. (1969) Phys. Stat. Sol. 36, 205

Chang, C.P., and Chen, C.W. (1977) Crystal lattice Defects 7, 91

DeSorbo, W. (1963) Phys. Rev. 132, 107

Dew-Hughes, D. (1974) Philos. Mag. 30, 293

Essmann, U., and Trauble, H. (1967) Phys. Letter A 26, 525

Essmann, U., and Trauble, H. (1969) Phys. Stat. Sol. 32, 337

Fearday, J.H. (1971) Magnetic Measurements of Strong-

Coupling $Pb_{1-2x}Bi_xTl_x$ and Pb-In Superconducting Alloys., Ph.D. Thsis, Ohio University, Athens, Ohio 45701

Fetter, A.L., Hohenberg, P.C., and Pincus, P. (1966) Phys. Rev. 147, 1

Fetter, A.L. and Hohenberg, P.C. (1967) Phys. Rev. 159, 2

Fietz, W.A., and Webb, W.W., (1969) Phys. Rev. 178, 657

Freyhart, H.C. (1971) Philos. Mag. 23, 345

Friedel, J., DeGennes, P.G., and Mtricon, J. (1963) Appl. Phys. Letter 2, 199

Good, J.A. and Kramer, E.J. (1970) Philos. Mag. 22, 329

Hill, D.C., Morrison, D.D., and Rose, R.H. (1969) J. Appl. Phys. 40, 5160

Kittel, (1971) Introduction to Solid State Physics., John Wieley & Son., New York

Koch, C.C., Freyhardt, H.C., and Scarborough, J.O. (1977) IEEE Trans. Mag. MAG-13, 828

Kramer, E.J. (1969) J. Appl. Phys. 41, 2

Kramer, E.J. (1973) J. Appl. Phys. 44, 1360

Kramer, E.J. (1975) J. Electron. Mater. 4, 839

Kramer, E.J. (1976) Philos. Mag. 33, 331

Kramer, E.J. (1978) J. Appl. Phys. 49, 742

Kramer, E.J. (1978) J. Nuclear Material 72, 5

Kroeger, D.H., Koch, C.C., and Charlesworth, J.P. (1975) J. Low Temp. Phys. 19, 493

Kuper, H., and Gey, W. (1977) Philos. Mag. 34, 859

Kusayanagi, E. and Yamafuji, K. (1969) Phys. Letter A 29, 529

Labusch, R. (1966) Phys. Letter 22, 9

Labusch, R. (1967) Phys. Stat. Sol. 19, 715

Labusch, R. (1969 a) Crystal Lattice Defects 1, 1

Labusch, R. (1969 b) Phys.Stat. Sol. 32, 439

Lauterwasser, E.D. and Kramer, E.J. (1975) Phys. Letter a 53, 410

Lowell, J. (1972) J. Phys. F 2, 547

Pande, C.S. (1976) Appl. Phys. Letter 28, 462

Parks, R.D. (1969) Superconductivity Vol. 1 and Vol. 2., Marcel Dekker, Inc., New York

Pippard, A.B. (1969) Philos. Mag. 19, 217

Rollins, R.W., Kupfer, H., and Gey, W. (1974) J. Appl. Phys. 45, 5392

Schmucker, R (1974) Inter. Discussion Meeting on Flux Pinning in Superconductors, At. andreasberg/Har3, Germany, Sept. 23-27

Schmucker, R., and Brandt, E.H. (1977) Phys. Stat. Sol. b 79, 479

Schneider, E. and Kronmuller, H. (1976) Phys. Stat. Sol. b 74, 261

Schneider, E. (1977) J. Low Temp. Phys. 29, 573

Tinkham, M. (1975) Introduction to Superconductivity., McGraw-Hill, Inc., New York

Trauble, H., and Essmann, U. (1968) J. Appl. Phys. 39, 4052

Ullmaier, H. (1975) Springer Tracts Mod. Phys. 76, 1

Yamafuji, K., and Irie, F. (1967) Phys. Letter A 25, 387

APPENDICES

Appendix A: Attempted Computer Calculation of the Critical Pinning Force.

The FLLD instability model is based on the movement of the FLL defects. Although it is generally believed that FLL defects move easily (Schmucker 1974, Kramer 1978), the exact value of the minimum force on a flux line required to move a nearby FLL defect (critical pinning force, see Section 6.4) is not clearly known.

An attempt was made to find critical pinning force to move a vacancy type FLL defect by constructing a simulated flux line lattice using an IBM 370 computer. The interaction force, F_{ij}, between two lattice points separated by a distance r_{ij} is given by (Tinkham 1975, see Sec. 2.1)

$$F_{ij} = \frac{\phi_0^2}{8\pi^2\lambda^3} K_1(r_{ij}/\lambda) \tag{A.1}$$

where ϕ_0 is the flux quantum, λ is the magnetic penetration depth and $K_1(r)$ is the first order Hankel function of imaginary argument. $K_1(r)$ decreases exponentially as $r \to \infty$ and varies as $1/r$ as $r \to 0$.

A two dimensional triangular lattice of size 17 x 17 with a fixed boundary was used. The lattice point at the center of the lattice was removed to create a vacancy and

all the lattice points except those on the boundary were relaxed until the net force on each lattice point was less than a preset value. The calculation included up to the third nearest neighbor contributions to the force on each lattice point. The result of this calculation gave an approximate structure for a vacancy type defect in the FLL.

Starting with this result, a lattice point next to the vacancy was moved toward the vacancy step by step and the force on this lattice point, f_D, was obtained at each step with all other lattice points relaxed. This result was compared with the force required to displace a lattice point in a perfect lattice, f_L. This calculation was repeated with lattice constants from $L=10\lambda$ to $L\sim 2\lambda$. The main result found was that f_D reached its peak when the displacement of the lattice point was about 15 % of the lattice constant, L, while f_L reached its maximum when the displacement was about 90 % of L. The ratio of the two peak values was one to two orders of magnitude.

In our calculation, the boundary was fixed and the restoring force on a lattice point did not only come from the shear distortion of the FLL but from the local compression of the lattice by the rigid walls. This gave a larger value of f_D than would be required in a real situation. It was evident that a large lattice size was necessary to obtain a realistic value.

However, we also found that our simulated lattice

became unstable as the lattice constant decreases below about 2.5λ. This led us to consider the stability of the flux line lattice (Appendix B).

The following difficulties made the above calculations not directly applicable to the real situation.

1) The boundary was fixed and this led to high values of f_D. This could be modified by another computer similation model but the more sericus problem listed below made such calculations difficult.

2) The 1/r dependence of the interaction force between flux lines when $r < \lambda$ requires a progressively large number of neighbors to be included in calculations of the force on lattice points as the lattice constant decreases. When the magnetic field approaches the upper critical magnetic field, B_{c2}, the lattice size and the computer time required to obtain a meaningful value would be forbiddingly high.

Appendix B: Condition Necessary for a Stable Two Dimensional Triangular Lattice.

It is well know that the triangular flux line lattice (FLL) has a lower free energy in most cases than the square FLL. However, very few authors comment about the stability of the lattice although several imply that it is stable over the full range in applied field from H_{c1} to H_{c2}. We investigated the stability of the FLL because our computer simulated lattice became unstable at high density. As outlined below we found the FLL is stable.

The interaction potential of an ordinary crystalline lattice has a minimum and there exists an equilibrium distance between two lattice points. However, the interaction potential between two lattice points of the flux line lattice is a monotonically decreasing function of the distance. The FLL is held together by the magnetic pressure of the applied field. We consider in this appendix a two dimensional lattice held together under pressure and the stability of such a lattice to a shear distortion which does not change the total area of the lattice. In this case the pdA work is zero and we only need to consider changes in the internal energy.

Let's consider a uniform infinitesimal distortion along the x-axis in a triangular lattice with an interaction

potential $U(r) = A\ r^n$. The distance from the lattice point at origin to the i-th lattice point is

$$r_i = [(X_i + u_{ix})^2 + Y_i^2]^{1/2}$$

$$= [(X_i + Y_i e_{xy})^2 + Y_i^2]^{1/2} \tag{B.1}$$

where u_{ix} is the displacement of the i-th lattice point ($u_{iy} = 0$). $e_{xy} = du_x/dy$ and X_i and Y_i are the x and y coordinates of the same lattice point in an undistorted lattice. The potential energy per lattice point after the distortion is

$$U_L = A \sum_i r_i^n \tag{B.2}$$

A stable lattice should satisfy the following conditions.

$$\left.\frac{dU}{de_{xy}}\right|_{e_{xy}=0} = 0 \tag{B.3}$$

$$\left.\frac{d^2U}{de_{xy}^2}\right|_{e_{xy}=0} > 0 \tag{B.4}$$

The condition (B.3) is satisfied by any symmetric lattice, however, the condition (B.4) is not always satisfied. For a

triangular lattice, there are always six equidistant lattice points 60 degrees apart from each other. If we consider these six as a group, the Eq. B.2 becomes

$$U_L = \sum_j U_j \tag{B.5}$$

where U_j represents the potential energy due to the interaction between the lattice at origin and the six lattice points belonging to the j-th group. d^2U_j/de^2_{xy} turns out to be

$$\frac{d^2U_j}{de^2_{xy}} \quad \frac{3}{4} A\ n(n+2) \quad R_j^n \tag{B.6}$$

where R_j is the distance of j-th lattice group from the origin. The above result does not depend on the lattice orientation. Therefore,

$$\frac{d^2U}{de^2_{xy}} = \frac{3}{4} A\ n(n+2) \sum_j R_j^n = K\ n(n+2) \tag{B.7}$$

where K is a constant. Therefore, a triangular lattice with a repulsive interaction will be stable only if n is less than -2.

The interaction energy between two flux lines (in the London limit, $\kappa \to \infty$) varies as $\log(1/r)$ at short distance (Appendix A). Therefore, when the lattice constant is small, the contribution of the nearest neighbors toward the stability of the FLL is negative. However, the contribution from the lattice points further away where the interaction energy varies as $\exp(-r)$ tends to make the lattice stable. It turns out that the contribution from the distant neighbors is always dominant and the lattice never becomes unstable or the shear modulus negative.